2011

Structure of mesovortices in Hurricane Ike (2008) derived from dual-Doppler analyses

Stephanie Ann Mullins

STRUCTURE OF MESOVORTICES IN HURRICANE IKE (2008) DERIVED FROM DUAL-DOPPLER ANALYSES

by

STEPHANIE ANN MULLINS

A THESIS

Submitted in partial fulfillment of the requirements
for the degree of Master of Science
in
The Department of Atmospheric Science
to
The School of Graduate Studies
of
The University of Alabama in Huntsville

HUNTSVILLE, ALABAMA

2011

In presenting this thesis in partial fulfillment of the requirements for a master's degree from The University of Alabama in Huntsville, I agree that the Library of this University shall make it freely available for inspection. I further agree that permission for extensive copying for scholarly purposes may be granted by my advisor or, in his/her absence, by the Chair of the Departments or the Dean of the School of Graduate Studies. It is also understood that due recognition shall be given to me and to The University of Alabama in Huntsville in any scholarly use which may be made of any material in this thesis.

Stephanie A. Mullins _____ 6/6/11 _____

(student signature) (date)

THESIS APPROVAL FORM

Submitted by Stephanie Mullins in partial fulfillment of the requirements for the degree of Master of Science in Atmospheric Science and accepted on behalf of the Faculty of the School of Graduate Studies by the dissertation committee.

We, the undersigned members of the Graduate Faculty of The University of Alabama in Huntsville, certify that we have advised and/or supervised the candidate on the work described in this thesis. We further certify that we have reviewed the thesis manuscript and approve it in partial fulfillment of the requirements for the degree of Master of Science in Atmospheric Science.

Kevin Knupp 6/6/11 Committee Chair
(Date)

Department Chair Sundar. A.C.

College Dean

Rhonda Kay Hardee 7/28/11 Graduate Dean

ABSTRACT
The School of Graduate Studies
The University of Alabama in Huntsville

Degree Master of Science College/Dept. Science/Atmospheric Science
Name of Candidate Stephanie Mullins
Title Structure of Mesovortices in Hurricane Ike (2008) Derived from Dual-Doppler Analyses

Past modeling work showed that vorticity mixing in the tropical cyclone (TC) inner core can lead to mesovortices (MVs) and impact storm intensity. Observations of MVs are necessary to improve understanding of these features and their role in TC dynamics, but few have been made. This study presents nearly 10 hr of observation of MVs in the inner eyewall of Hurricane Ike (2008) prior to and during landfall. Dual-Doppler derived vertical vorticity, divergence, perturbation pressure, horizontal and vertical wind fields are analyzed. Results indicate persistent arrangements in kinematic fields. Perturbation pressure retrievals suggest a local pressure minimum associated with the MVs. As the entities progress around the eye, the preferential updraft location transitions around the vorticity center. MV updraft magnitudes are within the top 5-10 % of TC vertical velocities. Characteristics shown for the MVs in Ike compare well with the limited body of previous MV observational work.

Abstract Approval: Committee Chair Kevin Knupp

Department Chair Jon S. Christopher

Graduate Dean Rhonda Kay Gaede

ACKNOWLEDGMENTS

First, I would like to thank my advisor, Dr. Kevin Knupp, for his guidance, patience, and support in completing this thesis. I am also grateful to Drs. Daniel Cecil, Walt Petersen, Timothy Coleman and Donald Perkey, for their willingness to serve on my committee, helpful feedback and assistance. I would like to acknowledge the Ike deployment crew (Kevin Knupp, Daniel Cecil, Dustin Phillips, Patrick Gatlin, Ken Leppert, and Cody Kirkpatrick) for their work in the field that made this study possible.

Additionally, I am indebted to many of my colleagues, including Patrick Gatlin, Chris and Elise Schultz, Todd Murphy, Danelle Botes, and Christina Crowe, for their help with learning some of the software and programming skills needed for this project. Most of all, I thank my family, friends, and previous mentors for their support and motivation to bring this thesis to fruition.

TABLE OF CONTENTS

Page

LIST OF FIGURES

LIST OF TABLES

CHAPTER 1

INTRODUCTION

Early observations of tropical cyclones (TCs) revealed the occurrence of coherent, mesoscale structures, including mesovortices (hereafter, MVs), embedded in the eyewall of the storm. Lewis and Hawkins (1982) described geometric eyewall shapes, which can form due to the presence of these features, from radar observations. More recent numerical modeling and observations have suggested formation avenues for these MVs.

A handful of specific intense hurricanes with MVs have been examined in detail. Marks and Houze (1984) were the first to use airborne Doppler radar data to construct the wind field in a TC. They found evidence for what may have been an MV embedded in the eyewall of Hurricane Debby (1982). Marks et al. (2008) presented analysis of a very small, intense MV encountered by a research aircraft in Hurricane Hugo (1989), the first documentation of in-situ observations of one of these features, and suggested the MV may have acted to intensify the hurricane via an eye/eyewall mixing process.

For about two days, while Hurricane Isabel (2003) was a Category 5 storm on the Saffir-Simpson hurricane scale (Saffir 1973, Simpson 1974), the inner core developed an impressive sequence of MVs that formed a "starfish" pattern closely resembling results of Kossin and Schubert's (2001, hereafter KS01) simple numerical model (Kossin and Schubert 2004). Examination by Montgomery et al. (2006) showed the features in

Isabel's low-level eye acted to transport high entropy air from the eye to the eyewall. Thus, they were vital to maintaining Isabel's high intensity, which was above previous theoretical limits proposed by Emanuel (Emanuel 1988, 1995, 1997).

Such a "turboboost" mechanism was theorized by Pershing and Montgomery (2003, hereafter PM03). Analysis of airborne Doppler radar and dropsonde data by Aberson et al. (2006) suggested that air within one of Isabel's MVs originated in the high-entropy eye and was being mixed into the eyewall. Such mixing allowed the storm to tap an additional heat source and increase local instability (Eastin et al. 2005b). Braun et al. (2006, hereafter B06) used a high-resolution, moist simulation of Hurricane Bonnie (1998) to show that MV features can interact with shear induced low level inflow, initiating updrafts and enhancing convection within the eyewall. Similar processes were suggested by simulations of Hurricane Erin (2001) by Braun and Wu (2007). Trajectory analysis for Bonnie by Cram et al. (2007) showed the transport of positively buoyant, low level eye air into the eyewall, thus supporting the PM03 mechanism. These impacts on storm intensity, a notoriously difficult parameter to forecast, warrant detailed observations of TC MVs, and Hurricane Ike (2008) provides a new case for study.

Ike began as a Cape Verde storm and reached peak intensity (125 kts, or Category 4) over the Atlantic. It impacted the Turks and Caicos Islands before making landfall in the Bahamas and Cuba. Weakened after its interaction with Cuba, Ike entered the Gulf of Mexico on 9 September with winds of only 70 kts (Category 1). Over the next couple of days, an eyewall replacement cycle took place. On 12 September, in the hours before landfall, the eastern edge of the eyewall began to spiral inwards, similar to the progression of the eyewall of rapidly intensifying Hurricane Guillermo (1997)

discussed by Sitkowski and Barnes (2009). Ike developed a much smaller eye and intensified to a strong Category 2 storm with winds of 95 kts (see Berg 2009 and Brown et al. 2010 for a complete synopsis of Ike).

In the hours just prior to and during its landfall along the southern Texas coast at 07 UTC on 13 September 2008, Ike exhibited a progression of eyewall shapes and MVs. The evolution of the inner core at this time was observed by both KHGX, the National Weather Service's (NWS) Houston/Galveston Weather Surveillance Radar-1988 Doppler (WSR-88D), and the University of Alabama in Huntsville's Mobile Alabama X-Band dual-polarization (MAX) radars. MAX was located at the Anahuac Airport in Anahuac, TX, about 53 km to the northeast of KHGX (Figure 1.1), a set up that allowed for true dual-Doppler analysis.

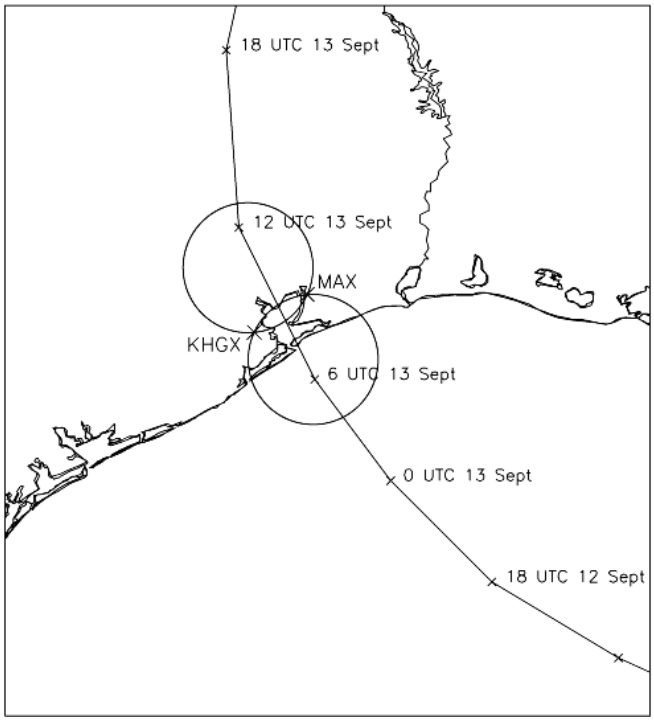

Figure 1.1: Map of KHGX and MAX locations in SE TX, including the track of Ike and outline of the dual-Doppler lobes.

The purpose of this work is to document the structure of Ike's eyewall MVs from the perspective of ground-based dual-Doppler radar analysis. Chapter 2 provides a background on past observational studies and modeling work on MVs. Chapter 3 describes the data and methodology employed in this study. For perspective, an overview of the evolution of the eyewall is given in Chapter 4. Results are discussed in the next chapter. A summary, error recap, and look at ongoing and future work are given in Chapter 6.

CHAPTER 2

BACKGROUND

Numerical modeling over the past decade has advanced understanding of the processes that govern the TC inner core and can lead to MV formation and vorticity mixing episodes. Keen observational studies have verified that similar features and episodes are not uncommon in the real world. Hurricane Ike (2008) was one recent landfalling system that displayed these features.

2.1 Polygonal eyewalls and mesovortices

Idealized, high-resolution barotropic simulations like Schubert et al. (1999, hereafter S99) and following works have shown that the breakdown of the eyewall into MVs and their subsequent mergers can have a profound impact on the intensity of the storm, and compliment theoretical work by PM03 suggesting a mechanism by which a TC can achieve an intensity beyond previously predicted limits (Emanuel 1988, 1995, 1997). Observations show a transition in TC kinematics and thermodynamics similar to model predictions for the mixing process (Reasor et al. 2000, Kossin and Eastin 2001, hereafter KE01), and in-depth studies on various storms (Jorgensen 1984, Marks and Houze 1984, Willoughby and Black 1996, Kossin and Schubert 2004, Montgomery et al. 2006, Aberson et al. 2006, Braun et al. 2006, Braun and Wu 2007, Cram et al. 2007,

Marks et al. 2008, Reasor et al. 2009) provide some validation to the modeling and theoretical concepts of the formation and impacts of MV features.

Early observations of shapes in hurricane eyewalls (e.g., Lewis and Hawkins 1982) are perhaps the first documentation of MVs in the TC inner core. In time it became clear these structures were more than just occasional curiosities. Jorgensen (1984) documented convective scale entities in the eyewall of Hurricane Allen (1980) that may have been MVs. The features in Allen consisted of localized peaks in reflectivity and vertical motion values of 7-9 m s^{-1} at heights of 0.5 - 6.1 km. Also, changes in equivalent potential temperature (θ_e) suggested mixing between the eye and eyewall and resemble profiles later determined by KE01 to be indicative of such a mixing process. With early airborne Doppler radar data, Marks and Houze (1984) provide details of a probable MV in the eyewall of Hurricane Debby (1982). Their analysis shows a cyclonic circulation embedded in the mean flow, collocated with a reflectivity appendage, vorticity maximum, and convergence/divergence couplet. The feature extended through the 1-5 km layer, and was persistent enough to be resolved in the coarse time resolution of the analysis (> 0.5 h).

Hurricane Andrew (1992) provided a unique case of MVs during its notorious landfall in south Florida. Willoughby and Black (1996) explain that, with a fast forward speed of 8.5 m s^{-1}, Andrew developed a series of MVs during the interaction of the N eyewall with the increased surface frictional convergence at the coastline. Newly forced updrafts increased the large background vorticity in the eyewall by stretching. Seven features were seen, each adjacent to enhanced areas of reflectivity, with lifetimes

on the order of about 10 min. Similar to later model results (KS01), one MV in Andrew contained a surface pressure 9 hPa below the value at the center of the eye.

The eyewall of intense or intensifying TCs can be simplified and viewed as an annulus of large vorticity. Convergence and moist convection here build up vorticity, creating a profile across the storm of two peaks (near the RMW) with lower values on either side. This configuration is barotropically unstable, and eventually the eyewall can break down to reach a more stable structure. One of the first and most comprehensive looks at this process was given in S99.

Using a high-resolution idealized barotropic nondivergent and unforced model, S99 simulated the progression of an initial annular ring of high potential vorticity (PV). Moist processes were neglected to keep the model simple and investigate the dynamics of these features without such complications. Along the inside of the initial annulus vorticity increases with radius while along the outside it decreases with radius. According to PV (Rossby) wave theory, one vortex Rossby wave (VRW) will propagate counter-clockwise relative to the primary flow along the inner gradient, and another will propagate clockwise relative to the flow along the outer, negative gradient. As the instability of the initial annulus increased, the vortex would break down. This breakdown began when the counter propagating VRWs became phase locked (i.e., they reached the same angular velocity, relative to Earth) and began amplifying each other. As the vortex is agitated, it can roll up into multiple MVs. In S99's simulation, the resulting MVs form a polygonal shaped eyewall and undergo multiple mergers so that after about 35 h the simulated vortex achieves a monopole, with a lower value of maximum vorticity located

in the center. The resulting vortex exhibited higher winds, a lower central pressure, and a significantly more stable vorticity profile.

With a similar model and numerical integration, KS01 performed nine experiments with annuli of varied initial vorticity, maximum winds, and radius of maximum winds (RMW). In all experiments, the initial vortex had its vorticity maximum located near the RMW and rolled up into multiple MVs. They formed on the inside edge of the ring, within the RMW, and each exhibited a local pressure perturbation. The structures moved about the simulated eye/eyewall region and often merged. Monopoles tended to result from annuli that were broader in size but smaller in total radius, while thin annuli (with larger total radii) produced a persistent set pattern, or "vortex crystal," with the MVs located just downwind of kinks in the flow (vertices of a polygonal eyewall). Generally, for a set annular width, the larger the ring was the more MVs it would break down into (because the ring is most unstable to a higher wavenumber or mode). KS01's numerical experiments showed that after a vorticity mixing episode, the storm vortex ends in either a monopole or crystal configuration with lower central pressure, decreased but broader maximum wind profiles, and lower magnitude but more stable vorticity profile, suggesting that MVs can act as transporters from an initial annulus to a final monopole without diluting the vorticity essentially trapped inside.

Aircraft Doppler and flight-level data support these simulated profile changes in transitioning storms. Reasor et al. (2000) looked at the evolution of Hurricane Olivia's (1994) structure by decomposing the airborne dual-Doppler derived wind field into symmetric and low wavenumber components. Over the time the seven flight legs in the

study were completed, Olivia weakened a bit and its RMW increased slightly. Horizontal vorticity maps created from the wind field decomposition showed a dominant wavenumber 2 asymmetry in the low level (≤ 3 km) vorticity averaged over all legs. The vorticity profile over the first leg suggested the storm contained a ring of elevated vorticity that was most unstable to wavenumber 2 perturbations. By the last legs, the profile had broadened, the vorticity maximum decreased, and the highest values shifted inward (i.e., it became more stable). To test the possibility that the dominant wavenumber 2 feature formed as a result of vortex breakdown as theorized by S99, Reasor et al. (2000) initiated a model similar to that in S99 with a vortex akin to what was observed during the first flight leg. This simulated Olivia vortex also exhibited a dominate wavenumber 2 vorticity asymmetry. The progression of the simulated vortex suggested the observed changes in the low level vorticity profile were consistent with the predicted breakdown due to barotropic instability according to the theoretical model of S99, and consistent with changes later shown by KS01.

More support for the breakdown hypothesis of S99 and results of KS01 is presented by KE01. With flight-level data from 44 TCs they present two characteristic regimes in kinematic and thermodynamic fields. Regime 1 tends to occur in intensifying TCs, while storms that have weakened past their peak intensity tend to demonstrate regime 2. Observed transition times varied, but in at least one case the progression occurred in less than an hour. Regime 1 has angular velocity and vorticity maximized within the eyewall and suppressed inside the eye, while in regime 2 the angular velocity and vorticity are essentially monotonic, with the maximum values in the center of the eye. Tangential winds in regime 2 are markedly decreased in the eyewall from regime 1

and increased in the eye (consistent with changes in the angular momentum profile). An example to the two regimes is provided in Figure 2.1 (Figure 7 from KE01). Thermodynamically, regime 1 consists of a very warm, dry eye and peaks in θ_e in the eyewall; regime 2 profiles have higher dewpoints in the eye and monotonic θ_e configurations (with the maximum at the center).

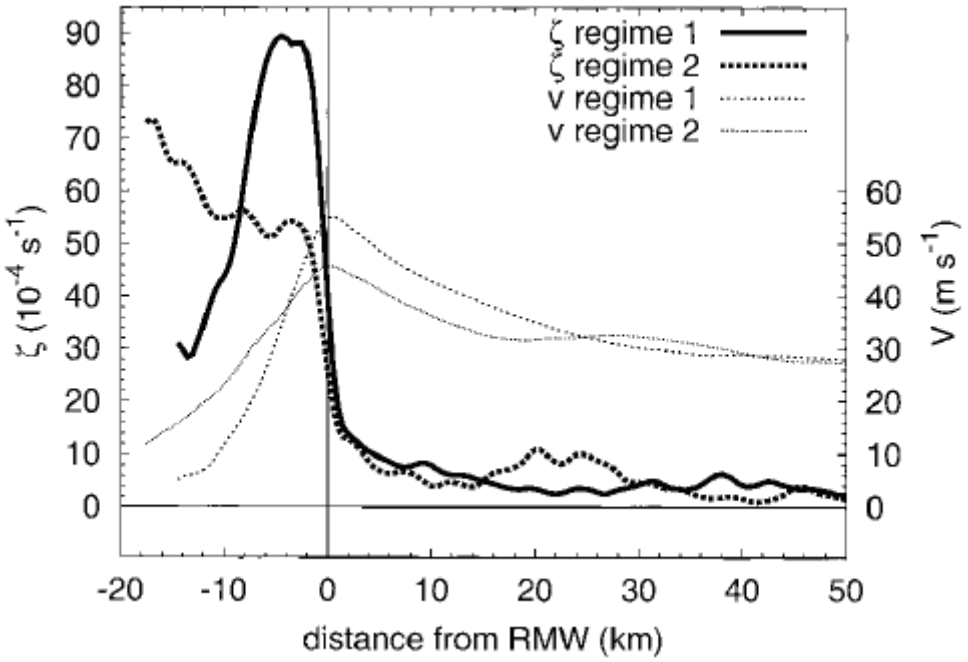

Figure 2.1: Example of regimes 1 and 2 as described by KE01. Averaged profiles of vorticity (ζ) and tangential winds (v) at 850 hPa in Hurricane Diana (1984). The regime 1 curve is the average of profiles from 22 flight legs over 11 UTC 11 September 1984 to 00 UTC 12 September, and the regime 2 curve is the average of profiles from 18 flight legs over 00 - 12 UTC 12 September (Figure 7 from KE01).

KE01 explain the transition from regime 1 to regime 2 in a purely horizontal sense, neglecting the changes in the height of the inversion level in the eye described by Willoughby (1998), using the idealized model of S99 initialized with a vortex representative of regime 1. Vorticity profiles of the initial and final simulated vortex express all of the kinematic qualities of regimes 1 and 2, respectively. Passive tracers originating at varying radii were used as an approximation for θ_e in the simulation.

Tracers that began in the eye tended to be mixed into the eyewall region, those that began in the eyewall region were mixed throughout the inner core, and only very few that began outside the eyewall were mixed into the eye. Qualitatively, this agrees with a decrease in eyewall θ_e at the eyewall, as seen in the transition from regime 1 to regime 2. It is quite remarkable that the simple 2D model of horizontal mixing presented by S99 can explain the observed regime changes documented by KE01.

Again employing the model of S99, Kossin et al. (2002) plant passive tracers in the eyewall of an initially unstable vortex. The progression of the tracers in the simulation closely resembles the shapes and swirling cloud patterns seen in high-altitude photoreconnaissance of the eye and eyewall of various intense TCs from as early as the 1950s. Montgomery et al. (2002) use fluid in a tank apparatus to physically simulate these patterns. They find that the peak tangential flow, which could be as great as 50% stronger than that of the main vortex, occurs within the MVs, and that the arrangement of the features was similar to that seen in KS01. While these similarities were striking, the best comparison was yet to come. Observations of Hurricane Isabel (2003) in the context of KS01's simulations and other theoretical work on intensity change provided a very exciting case.

Kossin and Schubert (2004) noted that while maintaining its highest intensity, Isabel showed nearly exact replications of the MV patterns shown in one of the KS01 experiments, as can be seen in Figures 2.2 and 2.3 (Figure 9 from KS01 and Figure 1 from Kossin and Schubert 2004). For two days, satellite images of Isabel revealed a stunning display in the eye and eyewall. In the morning on 12 September 2003, the eye displayed a starfish pattern, comprised of six MVs, five roughly evenly spaced around the

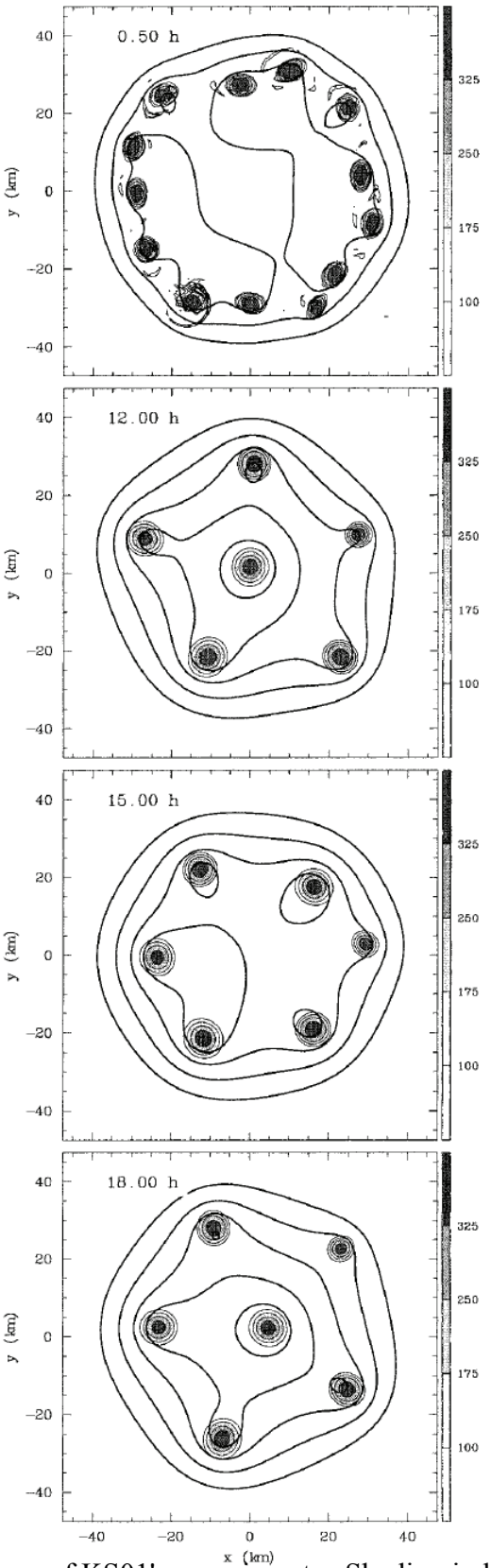

Figure 2.2: Results of one of KS01's experiments. Shading indicates vorticity (x 10^{-4} s^{-1}) and the contours show streamfunction. Time into the simulation is shown in the top left of each panel (Figure 9 from KS01).

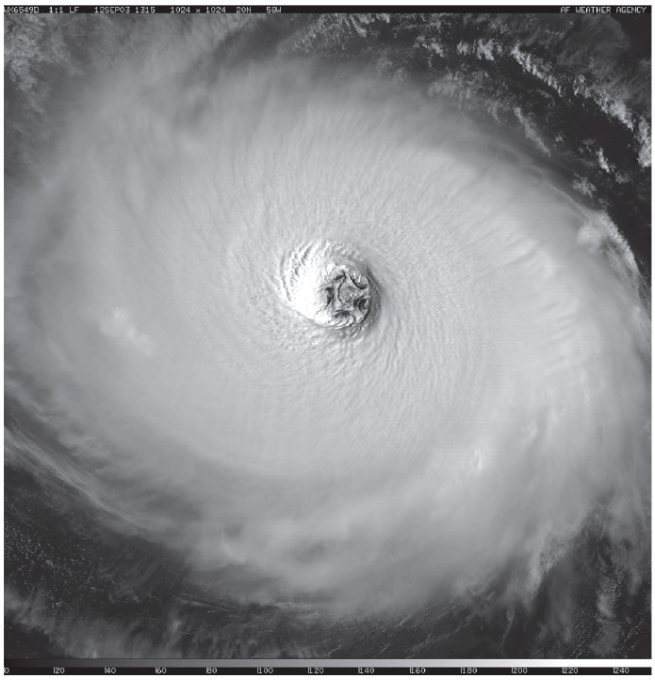

Figure 2.3: Image from the Defense Meteorological Satellite Program of Hurricane Isabel near 13 UTC 12 September 2003 (Figure 1 from Kossin and Schubert 2004).

inside edge of the eyewall and the last in the middle of the eye. The next day, super-rapid-scan-operations (SRSO) images from GOES-12 show that Isabel then had eight MVs that then merged and formed a square shaped eyewall in under 4 h. These amazing displays occurred almost exactly as in KS01's simulations, with some timing discrepancies, and suggest that the MVs may have acted to maintain Isabel's incredible intensity.

PM03 detail the case of "superintensity," which they define as a TC exceeding the maximum intensity predicted by theory furnished by Emanuel (1988, 1995, 1997) and based on a few simple parameters: sea surface temperature, outflow temperature, surface relative humidity, ambient surface pressure, Coriolis parameter, and storm size. According to this paradigm, the singular heat source driving the storm comes via a wind-induced heat exchange with the warm sea beneath the eyewall. With high spatial

and temporal resolution simulations, PM03 show that ingestion of high-entropy air from the eye into the eyewall provides an additional heat source beyond that of the warm sea. This extra energy acts as a "turboboost" to the simpler Carnot cycle used in previous maximum intensity theory. PM03 point to the high-resolution simulation of 1991 Hurricane Bob by Braun (2002) that shows that the MV features in the storm were associated with large θ_e anomalies and produced > 60% of the upward mass flux of the eyewall. Also recalling that Willoughby's (1998) observations show the low level eye can possess higher entropy and higher θ_e air than the eyewall, PM03 conclude the superintensity predicted by their model is possible in nature, and unlike previous theory, the maximum intensity of a TC is dependent on far more than the few parameters mentioned above.

As in KS01, after Isabel, PM03's results were more robust. Montgomery et al.'s (2006) look at Isabel provides evidence for the turboboost mechanism. With flight-level and GPS dropsonde data collected at or near the time of peak intensity from multiple research and reconnaissance aircraft, the authors present the first observational study to test the theory of PM03. Thermodynamic analysis shows low level air that spent some time in the eye could gain 14 K θ_e, and when this air was mixed into the eyewall it could provide extra energy to the storm, resulting in higher tangential winds. In fact, using Emanuel's earlier theory, the authors show the predicted maximum intensity for Isabel at the time of observation to be about 57 m s^{-1}, while the observed mean tangential winds were 76 m s^{-1}, a difference of nearly 35%.

Extending on Montgomery et al.'s (2006) assessment, Aberson et al. (2006) closely examine the structure of a very small MV that produced a 107 m s^{-1} horizontal

gust at 1.4 km above sea level. The sonde that took this measurement was released along the inner edge of the eyewall at about 2 km, became suspended in an updraft of >20 m s^{-1}, and encountered strong rotation: airborne dual-Doppler derived vorticity for the feature is 15 x 10^{-3} s^{-1}. The entity, < 4 km across, was evident as a distinct small, filamentary appendage in the reflectivity field. While values of θ_e in the eye were shown to be about 20 K higher than the eyewall, the MV's θ_e was nearly 5 K higher than that in the eyewall, suggesting mixing of the high entropy air of the eye into the lower entropy air of the eyewall. Bell and Montgomery (2008) extend this by showing that Isabel's eye established a surplus of high entropy via latent heat fluxes, and that the storm had an unstable, dual-peaked vorticity profile. As shown by S99 and KS01, the storm was apt to produce MVs, and consistent with PM03, the mixing that ensued provided extra energy for the heat engine. Bell and Montgomery (2008) conclude that the augmentation to the inner core by MVs was key to Isabel maintaining its category 5 intensity, and exceeding previous theoretical limits, while crossing over relatively cooler waters (in wake of Hurricane Fabian).

Evidence for how the mixing process displayed in Isabel may have been sustained can be seen in the results of B06's high-resolution simulation of Hurricane Bonnie (1998). With the fifth generation Pennsylvania State University - National Center for Atmospheric Research Mesoscale Model (PSU-NCAR MM5), Bonnie was studied to see how the environmental shear impacted the vertical motions in the eyewall. Updrafts were shown to be related to the progression of MVs around the eyewall. As MVs act as an impediment to inflowing air, convergence occurs radially outward from the entities as they encounter the low level flow associated with the shear and leads to updrafts.

Updrafts were shown to form as the MV enters the upshear side of the storm and intensify as the attendant MV moves cyclonically about the eye. Strongest in the downtilt region, the updrafts begin to weaken as they rotate to the downtilt-left side of the storm. While the updrafts may dissipate, the MVs persist on the opposite side, and can generate new (or intensify existing) updrafts upon the next pass on the downtilt-right side of the storm. A diagram of B06's conceptual model is shown in Figure 2.4 (their Figure 18); note that updrafts preferentially occur on the radial outward side of the MV. Convergence affiliated with the updrafts can increase the local vorticity, and the vorticity of the MV can be enhanced by stretching due to the increased upward motion. This acts to increase or sustain the annulus of high potential vorticity, which can in turn lead to production of new MVs via the breakdown process described by S99. While Isabel experienced less shear than Bonnie when its MVs were observed, the interactions shown by B06 may have been partially responsible for the longevity of the features.

Using the same model, Cram et al. (2007) present a trajectory analysis for Bonnie that further reinforces the PM03 mechanism. Paths shown for parcels seeded in the low level eye can progress outward to the eyewall, and rise in updrafts there. Values of θ_e are above 370 K for the parcels that enter the eyewall, and this decreases by 5 K as the air ascends in the updraft, but after reaching about 2 km, the value is roughly steady with height to about 10 km, suggesting the warmth from the low level eye is maintained against the relatively cooler (lower θ_e) eyewall air. The pattern of the trajectories' ascent was consistent with the updrafts that developed in the B06 simulation, preferring the downshear left side. The decrease in θ_e as parcels begin to rise should be matched by an increase in the θ_e of the surrounding air to satisfy conservation, so the eyewall is supplied

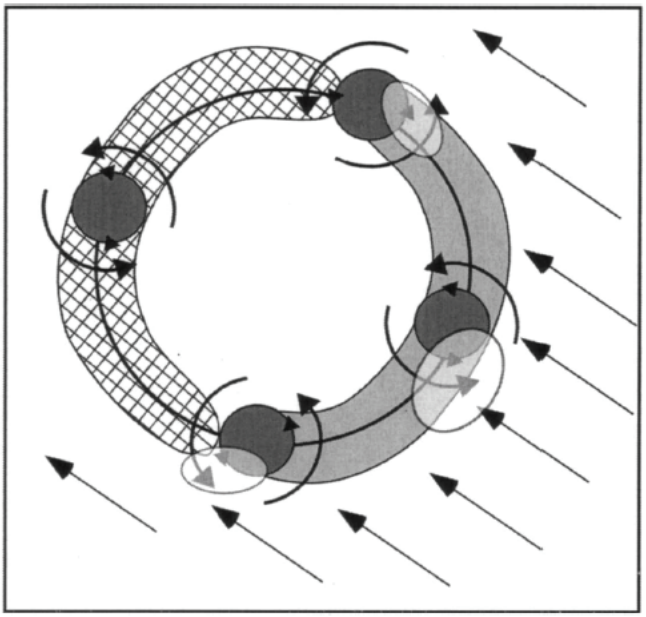

Figure 2.4: B06's diagram depicting updraft generation via interaction of mesovortices with shear-induced low-level inflow. Large shaded and hatched half circles show favored areas for upward and downward motion due to shear, respectively. Flow from the environmental shear is shown with straight arrows. Mesovortices are shown as the dark circles, and their local cyclonic flow with the accompanying curved arrows. Semi-transparent ovals highlight regions of low-level convergence and favored updraft generation (Figure 18 from B06).

with extra energy. Calculated maximum intensity estimates (based on earlier Emanuel theory) are performed and compared to the tangential winds produced in the simulated Bonnie to show that the modeled storm fits PM03's definition of superintensity. This along with the documented eye/eyewall mixing suggests that the turboboost mechanism occurred in Bonnie.

More than a decade before Isabel, a harrowing research aircraft mission encountered an MV in Hurricane Hugo (1989) while the storm had maximum winds of about 70 m s^{-1}. The interaction led to an engine failure on the aircraft and the radar systems were shut down, but data collection did not cease. Marks et al. 2008 analyzed these first ever in-situ observations of an MV in light of the dynamical hypotheses given

in works published after Hugo (S99, KS01, PM03). Flight-level data showed Hugo's horizontal winds at the RMW were about 70 m s^{-1} at the time of the mission, and satellite data suggested the storm was in a rapid deepening phase. Like the feature detailed by Aberson et al. (2006), the Hugo MV was very small (about 1 km radius) and located on the inside edge of the eyewall, within the RMW. A vorticity maximum of 1.25 x 10^{-1} s^{-1} (more than seven times that of the main vortex) was located at the center of the feature. There was a distinct pressure perturbation of 12 hPa associated with the MV, redolent of KS01's experiments, and in approximate cyclostrophic balance. Flight track values of θ_e in the eyewall peaked at the MV (> 370 K), hinting at the low level eye as a source region as shown by PM03.

While Hurricane Guillermo (1997) rapidly intensified in a an environment of increasing deep layer shear, transient convective features akin to MVs formed in and propagated cyclonically around the eyewall. Studies by Reasor et al. (2009) and Sitkowski and Barnes (2009) inspect airborne Doppler radar and GPS dropsonde data during this time. In the former, the evolution of the vorticity profile is similar to the regime 1 and regime 2 classifications defined by KE01, but in the Guillermo case regime 2 is seen as the storm is still intensifying. This suggests that the storm underwent a vorticity mixing episode while intensifying. Also in the time of most pronounced intensification, transient convective features formed in the downshear side of the storm, where upward motion then dominated, as in B06 and Braun and Wu (2007). Sitkowski and Barnes' (2009) work recounts the inward progressive spiral of a portion of the eyewall, eventually impinging so far into the eye that it forms an eyewall about 10 km smaller in diameter than the storm had previously. This inward progression could be

complete in as little as 10 min, took place multiple times, and is speculated to have been initiated by mixing similar to S99 and KS01. Analysis of the sondes' data shows warming along the inner edge of the eyewall over about 24 h as the storm strengthened, fairly coincident to the region of transient convective features discussed by Reasor et al. (2009). Momentum and entropy advection inward in the low levels from the environment is described as having little impact on the rapid intensification of Guillermo. Sitkowski and Barnes conclude that the strengthening was governed most by processes in the inner core and eyewall.

Both positive and negative effects on TC intensity have been shown to coincide with the occurrence of MVs: in the unforced simulations of S99 and KS01, the maximum tangential winds of the primary vortex decreased after a mixing episode, but the work of PM03, Braun et al. (2006), and Braun and Wu (2007) showed that interactions between the eye and eyewall via MVs led to significant intensification. Rozoff et al. (2009) discuss this "dual nature" of vorticity mixing. With a forced 2D barotropic model, diabatic and frictional effects are continuously applied (in contrast to the unforced simulations of S99) to a number of initial vortices to test the evolution of rings of various sizes (similar to the experiments in KS01). Results support many of the conclusions of works mentioned above: radially thinner rings of higher vorticity were the most likely to breakdown, inward mixing of vorticity via MVs acted as a break on intensification or even weakened the system, and the profile of vorticity across the vortex suggests mixing as in KE01. Because of the forcing employed in the model, generated vorticity replenishes the initial annulus around the mixed vorticity core (monopole that formed after the first mixing episode). As this is still an unstable configuration, mixing episodes

can continue as the ring of higher vorticity is continuously rebuilt, and once "sufficiently many" mixing episodes have occurred, the forced vortex reaches a more barotropically stable state (Rozoff et al. 2009).

Hendricks et al. (2009) revisited modeling the evolution of high vorticity annuli. With a nonlinear version of S99's nondivergent barotropic model 170 simulations were run. The initial annuli comprise a two-dimensional parameter space, defined by thickness and hollowness: the former defined as the ratio of the inner to outer radius of the ring and the latter as the ratio of initial value of the vorticity in the eye to the inner core. Results with the nonlinear model suggest that the linear model (S99) predicts the most unstable wavenumber of the breakdown process well, with the exception of wavenumbers 1 and 2 (not possible in S99 due to assumptions inherent in the model) that were manifested as a wobble in the eye (trochoidal oscillation in the track of a moving storm) and elliptical eyewall shape, respectively. By far, the most of the unstable rings tended to evolve into monopoles, with thin, hollow rings reaching this end state faster than thicker, more filled rings. Results also showed that some rings developed MVs that either persist indefinitely or linger for > 15 h before merging to a monopole ("slow monopoles"). In all the simulations, both the minimum central pressure and maximum tangential velocity decreased after a mixing episode, most substantially for vortices that formed a monopole after 48 h. This is similar to previous results (S99, KS01), and highlights that simple pressure-wind relations may not be valid during vorticity mixing events. While Hendricks et al.'s (2009) results show these events decrease winds, those authors contend the continuous vorticity generation that occurs in real storms promotes consecutive

mixing events and decreases in central pressure (as in Rozoff et al. 2009), and thus the mixing of vorticity can compliment, but not solely explain, TC intensification.

Dynamic explanations and modeling of MVs require improvements, but provide a good basis for attaining a better understanding of how such entities impact changes in TC intensity and inner core structure. As diabatic generation of potential vorticity increases the barotropic instability of the eyewall, the eyewall can break down into these small vortex features. The MVs are able to preserve the vorticity in their cores as they rearrange themselves and merge, often resulting in a lowering of the TC's core minimum pressure in cases where a monopole is ultimately formed. Other instances of MVs result in ornate patterns in the eyewall of the storm, as in Isabel. We must also consider the increased threat MVs may pose to populations. Willoughby and Black (1996) explain how MVs in Andrew locally increased the already devastating consequences of the storm. Impacts on TC intensity change and destructive potential at landfall warrant further detailed observational analysis of these entities.

2.2 Hurricane Ike

As this work is concerned with MVs that formed in Hurricane Ike (2008) near the time of landfall, a brief history of the storm, based on Berg (2009) and Brown et al.'s (2010) more complete assessments, is given here.

The system that became Ike started as an African easterly wave that moved off the continent on 28 August 2008. Convection increased and a surface low pressure developed near the axis, eventually organizing enough to be dubbed a tropical depression about 1250 km west of the Cape Verde Islands at 06 UTC on 1 September. The fledgling system was named Tropical Storm Ike 6 h later. Ike continued on across the Atlantic

south of a strong subtropical high, developed an eye and was upgraded to Hurricane status by 18 UTC 3 September. A deep trough to the NW weakened this ridge so that Ike's motion turned to the WNW. During this time, Ike underwent an intensification episode that strengthened the storm by 70 kts (~36 m s^{-1}) in only 24 h, from 55 kts at 06 UTC 3 September to 125 kts at 06 UTC 4 September. This category 4 strength was to be the maximum intensity Ike would achieve.

After attaining its peak intensity, Ike was influenced by a high over the western Atlantic, which increased the northerly shear atop the storm. Not surprisingly, this resulted in a more asymmetric cloud pattern and slight weakening. Ike was then steered primarily by the building high in the western Atlantic that eventually turned the storm to the WSW by 00 UTC on 6 September. Another bout of shear, from the NW, briefly weakened Ike again, but it regained Category 4 strength by 18 UTC on 6 September, just prior to skirting the Turks and Caicos Islands. It weakened to about 110 kts (Category 3) ahead of landfall in the SE Bahamas near 13 UTC on 7 September. This land interaction weakened the storm, but again it regained Category 4 strength before nearing Cuba, where the center came ashore about 02 UTC on 8 September with winds of about 115 kts.

After being modified by Cuba, Ike emerged over the Caribbean Sea with maximum sustained winds of about 75 kts around 15 UTC on 8 September. The storm moved along the southern Cuban coast, and made a second landfall on the island at about 14 UTC on 9 September. Ike finally entered the Gulf of Mexico near 21 UTC that day. Time over and near Cuba weakened the inner core, and Ike's wind field was larger upon moving into the Gulf. A small eyewall remained after the storm left the island, and this was enveloped by rainbands, essentially forming a secondary eyewall, as Ike moved on

NW and strengthened slightly. By 18 UTC on 10 September the winds were up to 85 kts, and hurricane and tropical storm force wind radii were 100 nmi (185 km) and 240 nmi (440 km), respectively. On 10 September, the subtropical ridge turned Ike towards the WNW, and the eyewall replacement cycle was completed by 18 UTC 11 September when the inner eyewall (that had emerged from Cuba) was gone and the banding that formed around it dominated.

At this point, Ike had a large wind field and little convection within its inner core, making rapid intensification unlikely. On 12 September, along the western edge of the ridge, Ike experienced about 15 kts (5-8 m s^{-1}) of northerly shear and progressed NW, moving towards the TX coast. This can be seen in the satellite deep layer shear composites (200-850 mb layer) shown in Figure 2.5 (UW-M, CIMSS). These moderate shear values persisted up through the storm's landfall (Beven 2008). In the hours prior to landfall, a smaller eye (40 n mi diameter) formed and winds increased to 95 kt. Formation of the smaller eye occurred as part of the NE eyewall progressed inward and joined with the inner edge of itself (see Section 4.1), similar to one of the inward spiraling episode of the eyewall of Guillermo detailed by Sitkowski and Barnes (2009) during that storm's rapid intensification. Figure 2.6 shows that Ike's intensity remained at about 85 kts until nearly half the eye had crossed the coastline, then rapidly weakened after landfall. The hurricane accelerated from about 00 UTC on 13 September as it approached SE TX, and continued to increase as Ike moved inland. From ground-based radars (Figure 1.1), the newly smaller eyewall was observed to exhibit polygonal shapes and MVs. Analysis of these features is the focus of this work. Ike turned again to the NNW and made its first US landfall near 07 UTC on 13 September, along the northern

a) 18 UTC
12 September

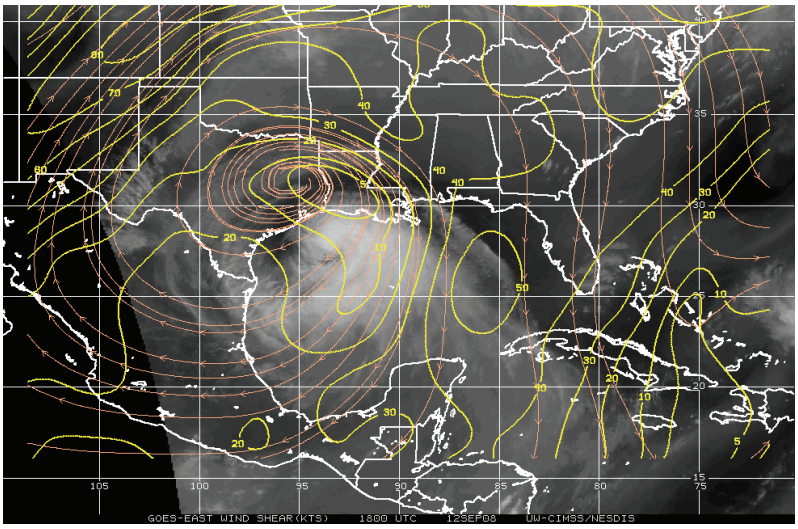

b) 00 UTC
13 September

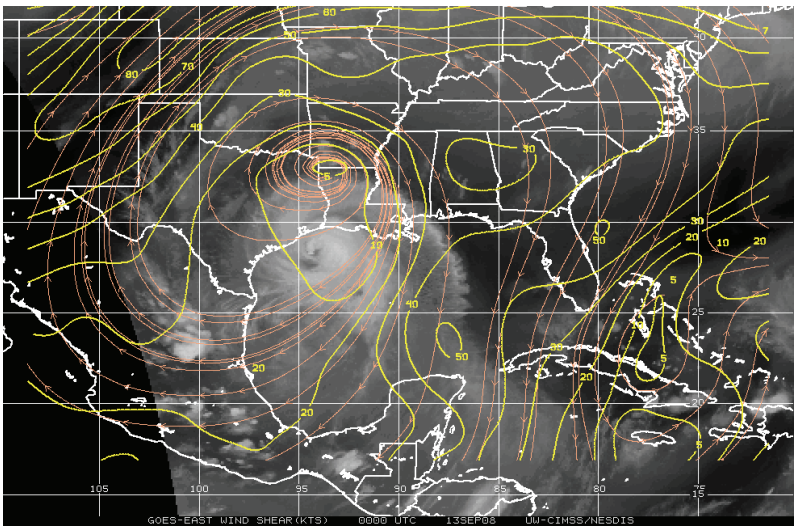

c) 06 UTC
13 September

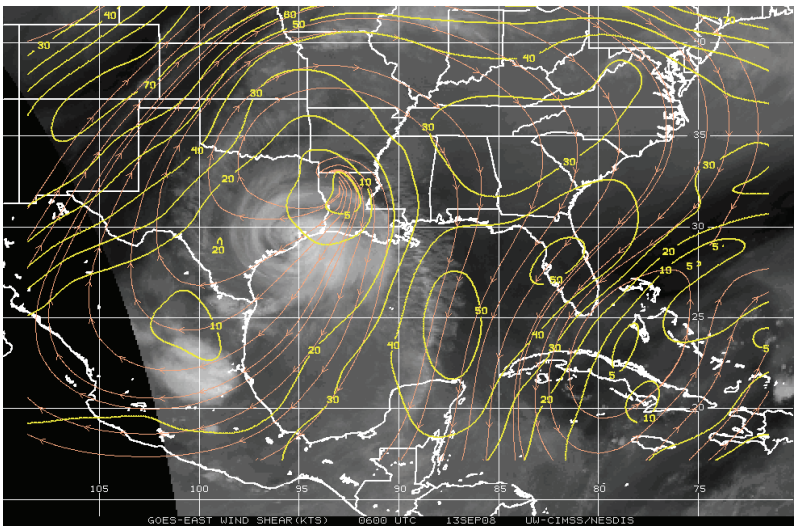

Figure 2.5: Satellite-derived deep layer (200-850 mb) shear at (a) 18 UTC on 12 September, (b) 00 UTC on 13 September, and (c) 06 UTC on 13 September. Prior to and during landfall, the inner core of Ike experienced 10-15 kts of N to NE shear.

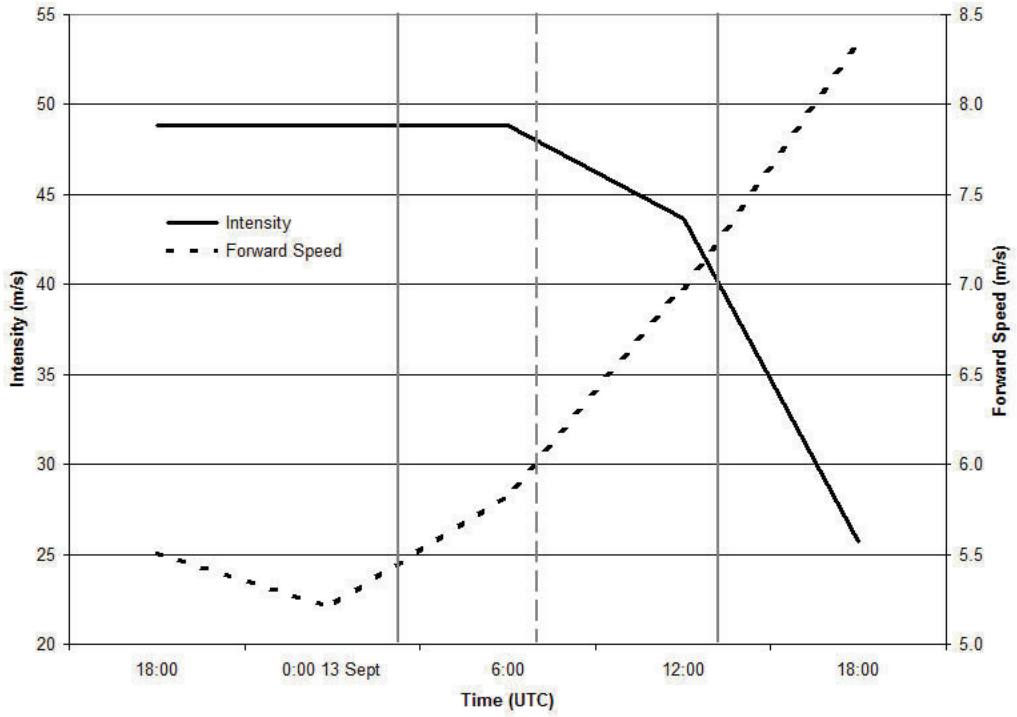

Figure 2.6: Best Track intensity (m s^{-1}, left ordinate) and interpolated forward speed of Ike (m s^{-1}, right ordinate). Solid gray vertical lines indicate the time interval when the eyewall was in the dual-Doppler lobes, and the dashed gray vertical line denotes landfall.

edge of Galveston Island, TX. Ike's center passed north over Galveston Bay, then on into part of east TX, where it was downgraded to a tropical storm. Remnants of the system became extratropical on 14 September and continued to the NE. What had been Ike caused hurricane force wind gusts in part of the Ohio River Valley later that day. The weakening low progressed into Canada and was absorbed by another system on 15 September.

CHAPTER 3

DATA AND METHODOLOGY

Data collected from both KHGX and MAX are used in this study. Raw reflectivity and velocity data are edited and used for dual-Doppler analysis. Pressure perturbations are retrieved from the derived wind field. Various plots of the results are created with IDL. Section 3.2 outlines the analysis procedures and includes discussion of sources of error within the methodology.

3.1 KHGX and MAX radars

The KHGX radar operated multiple volume coverage patterns (VCPs) during Ike's progression through its domain. At this time, KHGX had been upgraded to super-resolution data collection. Reflectivity (hereafter Z) data in elevation scans $\leq 1.5°$ have 250 m gate spacing along the radar beam, while the Z in scans above 1.5° have 1 km gate spacing. Radial velocity (v_r) and spectrum width data at all elevation angles have 250 m gate spacing. KHGX is an S-band radar with a wavelength of 10.7 cm, and the beamwidth is 0.95 degrees. In this study, the Level II format of WSR-88D data is used.

From about 1500 UTC on 12 September, when outer portions of the storm were clearly in range, to 2145 UTC on 12 September, when the inner core of the hurricane had progressed within the radar's view, KHGX employed VCP 211, which scans at elevation

angles 0.5, 1.5, 2.4, 3.4, 4.3, 5.3, 6.2, 7.5, 8.7, 10.0, 12.0, 14.0, 16.7, and 19.5° in about 5 min. After 2145 UTC, this pattern changes to VCP 121, scanning at 0.5, 1.5, 2.4, 3.4, 4.3, 6.0, 9.9, 14.6, and 19.5° in under 6 min. Once the center of Ike moved within about 100 km of KHGX, the VCP changes again to 212. VCP 212 scans at 0.5, 0.9, 1.3, 1.8, 2.4, 3.1, 4.0, 5.1, 6.4, 8.0, 10.0, 12.5, 15.6, and 19.5° in under 5 min. KHGX remained in VCP 212 until Ike was far inland over NE TX.

All of the aforementioned VCPs are part of the NWS' range folding mitigation group of scanning strategies, allowing for longer ranges at the lowest elevation angles (NOAA, 2009). These VCPs all use a split cut technique that allows for alterations to the pulse repetition frequency (PRF) during the scan, resulting in multiple Nyquist velocities for a single volume scan according to $V_{max} = \pm (PRF\ \lambda) / 4$, where λ is the wavelength of the radar (Rinehart 2004). These range from 28.1 m s^{-1} to 35.5 m s^{-1}.

MAX, located about 53 km to the NE of KHGX (Figure 1.1), collected Z, v_r , and spectrum width along with dual-polarimetric parameters differential reflectivity (Z_{dr}), differential phase (Φ_{dp}), specific differential phase (K_{dp}), and correlation coefficient (ρ_{hv}). MAX operates with a PRF of 1200 Hz and 3.2 cm wavelength, corresponding to a Nyquist velocity of 9.5 m s^{-1}. Gate spacing along the beam is 125 m, and the maximum range is about 125 km. A wedge of 40° is blocked at low levels (elevations < 10°) to accommodate the cab of the radar truck. During Ike, this area is between azimuths 330-10°, thus it is important to note that the E portions of the indicated NW dual-Doppler lobe are not resolvable in the dual-Doppler analyses.

Scanning strategy for the MAX consisted of volume scans (here termed MAX1, MAX2, and MAX3) and RHIs. MAX1 scans at elevation angles 0.5, 0.8, 1.0, 1.5, 2.0,

and 2.5°, MAX2 scans at 0.8, 1.5, 2.5, 4.5, 6.5, 8.5, 10.5, 12.5, 14.5, 16.5, 18.5, 20.5, 22.5, 24.5, 26.5, 28.5, and 30.5°, and MAX3 scans at 0.8, 1.5, 2.0, 2.5, 3.5, 4.5, 5.5, 6.5, 8.0, 9.5, 11.0, 13.0, 15.0, 17.0, 19.0, and 21.0°. From about 00 UTC on 13 September, when Ike's inner core is just entering MAX's range, to about 0400 UTC alternating volume scans of MAX1 and MAX2 were performed. After this, MAX changed to alternating MAX1 and MAX3 and remained in this sequence until the center of Ike was far inland over NE TX. Only volumes that scan with MAX2 or MAX3 were used in the dual-Doppler processing as these samples achieve greater spatial coverage. RHI scans were also periodically done between volumes at varying azimuths as Ike progressed through the MAX domain.

Observations of MVs from both airborne and ground-based radars have been documented over at least the last two decades. However, to the author's knowledge this work is the first to examine these features with dual-Doppler processing from ground-based radars. As a next step, dual-polarization data collected by the MAX will be analyzed in future work. As of yet, this dataset is truly unique.

Initial data from both radars were converted to universal format (UF) then to DORADE (DOppler RAdar Data Exchange format, Lee et al. 1994) format sweepfiles for use in NCAR's SoloII software. For the KHGX data this involved splitting the fields into separate files (Z in one and v_r and spectrum width in another) because of the differences in radial spacing. Raw data were manually edited in SoloII, primarily to remove aliasing in the v_r fields. Editing of the MAX Doppler velocities was quite tedious! After editing, the data were gridded using REORDER (an NCAR software package, Oye et al. 1995) to a common Cartesian grid 160 km x 160 km x 10 km with

horizontal spacing of 1 km, vertical spacing of 0.5 km, and origin at the midpoint of the baseline between the two radars. This is done with a radius of influence of 1.0 km in all directions. Gridded data are then used in NCAR's CEDRIC (Custom Editing and Display of Reduced Information in Cartesian space, Mohr et al. 1986) software for dual-Doppler processing and retrieval of the pressure perturbation field; output is to netCDF format (Rew and Davis 1990). Filtering, smoothing, and initial computations are done in CEDRIC, and output netCDF files are read into IDL for post processing and plotting. Further details on the methodology are provided in the following sections.

3.2 Dual-Doppler and pressure perturbation retrieval techniques

Procedures for synthesizing radial winds from multiple Doppler (airborne and ground-based) radars have been developed by Armijo (1969), Miller and Strauch (1974), Ray et al. (1978), Ray et al. (1980), Testud and Chong (1983), Chong et al. (1983), Chong and Testud (1983), Mueller and Hildebrand (1985) and others. For this study, the synthesis of radial winds is done in CEDRIC with the methods described in Mohr et al. (1986), similar to the process developed in the aforementioned papers. Horizontal wind components (u, v) are obtained from the synthesis. Vertical velocities (w) are calculated as follows: First, the mass continuity equation is integrated vertically with an upper boundary condition of w=0 at the top of the domain, as expressed in O'Brien (1970). Downward integration is employed rather than upward to mitigate concerns arising from the fact that the radar sampling does not extend down well into the boundary layer. Next, bulk estimates of the particles' terminal velocity (v_t) are subtracted from the resulting W, giving the value of w (i.e., $w = W - v_t$). These fallspeed estimates are based on the maximum Z value for a given grid box; because of attenuation in the MAX data,

generally the KHGX Z is used. Finally, values of horizontal divergence and vorticity are calculated from the resultant zonal (u) and meridional (v) wind components.

There are multiple factors to note in terms of error contribution in the methodology thus far. The dual-Doppler retrieval method assumes the scanned volumes are in steady-state, so that observations made by the two radars are taken as simultaneous measurements of the same flow field. Changes within radar volumes do, however, occur over the time that it takes for each scan to be completed (about 5 min). Pairs of scans from KHGX and MAX used in the analyses were not exactly matched, but were generally completed within 2-3 min of each other (Table 3.1). Other errors can arise based on the location of the examined feature relative to the radars, beam location inaccuracies, the underdetermined nature of synthesizing two (as opposed to three or more) Doppler velocity fields, and vertical velocity errors compounded over the integration process.

Doviak et al. (1976) showed that best estimates of horizontal wind magnitude occur when the true wind direction bisects the angle of the two radar beams, but the most accurate horizontal wind direction is obtained when this direction is perpendicular to the bisector. The direction of the horizontal wind result is best at stronger true wind magnitudes. Systematic and random errors also complicate matters. Doviak et al. also showed that the presence of non-uniform Z within a sample, use of an incorrect relationship for Z and particle fallspeed, and inaccuracies in beam position (as system error) can contribute to errors of at least 1-2 m s^{-1}. Random errors in measured Doppler velocities can be of the same order and originate from turbulence in the sample volume (large spectrum width) and beam position inaccuracies (arising from violations to the

standard refraction model, Doviak and Zrnic 1993, Rinehart 2004). The characteristic TC environment is incredibly moist and usually contains a temperature inversion in the eye (Willoughby 1998). It is then highly likely that radar beam propagation did not fit the standard refractive model.

Doviak et al. also explained that vertical velocity estimates tend to be much worse than horizontal components, with nearly twice the variance of the horizontal estimates and standard deviations on the order of a few m s^{-1}. While the choice of an appropriate Z-fallspeed is important, their work demonstrated variances of the vertical wind estimate tend to be "significantly smaller" than that in the fallspeed estimate due to drop size distribution variability. All of the issues for the vertical wind retrieval are compounded with the integration of the mass continuity equation. Errors accumulate throughout the integration, and further uncertainty arises from the imposed boundary conditions. This specific problem was explored by Matejka and Bartels (1998), who showed downward integration to be much more stable than upward schemes, due mainly to the density profile. When the initial implementation begins at the minimum density, accumulated errors are less than if it is first applied from the bottom (largest density) and sent upwards. Inaccurate boundary conditions (i.e., violations of the assumed vertical motion value above or below the domain) also contribute to erroneous final w estimates. The present study employs downward integration, especially since sampling of the hurricane boundary layer was rarely accomplished by the dual-Doppler analyses in Ike.

In the process of evaluating the effects of advection and convective storm evolution, Clark et al. (1980) showed that for dual-Doppler networks "horrendous" errors were possible in all of the Cartesian wind components due primarily to the

underdetermined nature of the radial velocity synthesis. In their study, errors related to the time evolution and advection of the storm (analyzed with the assumption of zero terminal fallspeed) were insignificant compared to the primary underdetermined problem. While their error values are extreme (about 20 m s^{-1} and 100 m s^{-1} for the worst horizontal and vertical retrievals, respectively), their paper demonstrates the limitation of a two radar system and the severity of the underdetermined problem relative to inaccurate advection and evolution assumptions.

Initially, the analysis was performed for the 160 km x 160 km x 10 km grid mentioned above using a uniform advection equal to Ike's forward speed as interpolated from the HURDAT Best Track Record kept by the National Hurricane Center (NHC). Storm center position information in the Best Track database is provided to the nearest tenth degree (latitude and longitude) at 6 h intervals. Due to this relatively coarse resolution, the exact motion of the storm center may not be properly accounted for, but to at least a first order the forward speed estimates are reasonable. A second, smaller domain was then placed over the feature of interest (e.g., Figure 5.1a). Generally, the smaller domain was 30 km x 30 km x 10 km, with the same spacing as for the larger grid. Some features require a larger second domain; the dimensions of the smaller domain used for each analysis are noted in Table 3.1. Horizontal winds derived in the first analysis were averaged over the entire second domain. This value was then used as the uniform advection for a new synthesis in CEDRIC over the smaller domain. Other than the advection and domain dimensions used, the analysis process was the same for the large and small domains. Horizontal divergence, vorticity, and radial and tangential wind components were computed from the final synthesized wind field.

It should be noted that the use of an average motion over the smaller domain can lead to errors in the analysis. TCs do not have uniform wind distributions with height (Wang and Wu 2004). Here the average is used to facilitate an estimate of the highly variable advection in the region of the MVs. This produces a first-order result in the wind field, and future work will involve using an advection scheme that allows for horizontal and vertical variations (e.g., Shapiro et al. 2010a,b). More importantly, however, the analysis procedure assumed that the center of the hurricane's circulation and its surface location obtained from the Best Track are the same at all heights. Vertical stacking of a TC center with height is rarely observed, especially when there is any type of environmental shear on the vortex (Frank and Ritchie 1999). The assumption of a consistent TC center with height may produce further errors in the large and small domain runs.

Once the derived 3D wind field is obtained, it is possible to perform a mathematical retrieval to obtain an estimate of the pressure perturbation field. The method used here is based on Gal-Chen's (1978) work, which has been used in numerous other studies, including Hane et al. (1981), Roux et al. (1984), Roux (1985), and more recently Murphy and Knupp (2009). Starting with the anelastic form of the continuity equation

$$\nabla \rho_{0a} U = 0 \quad , \tag{3.1}$$

where ρ_{0a} is the hydrostatic adiabatic density (exponential function of height), ∇ is the standard del operator, and U is the full 3D wind (made up of u, v, and w components), and the anelastic form of the horizontal momentum equations

$$\frac{\partial}{\partial t}\rho_{0a}u + \frac{\partial}{\partial x}\rho_{0a}uv = -\frac{\partial p'}{\partial x} + f_x + fr_x$$
$$\frac{\partial}{\partial t}\rho_{0a}v + \frac{\partial}{\partial y}\rho_{0a}uv = -\frac{\partial p'}{\partial y} + f_y + fr_y \quad , \tag{3.2}$$

where ρ_{0a} is as before, u and v are the zonal and meridional wind components, p' is the deviation of the pressure from its basic state value, f_x and f_y are the zonal and meridional components of the Coriolis force, and fr_x and fr_y are zonal and meridional frictional terms that include turbulent stresses, and solving for the pressure term leads to the following expression of the horizontal perturbation pressure field:

$$\frac{\partial p'}{\partial x} = F \equiv \frac{Du}{Dx} + f_x + fr_x$$
$$\frac{\partial p'}{\partial y} = G \equiv \frac{Dv}{Dy} + f_y + fr_y \quad , \tag{3.3}$$

where p', u, v, f_x, f_y, fr_x, and fr_y are as before, and Du/Dx and Dv/Dy are the total derivatives of the zonal and meridional wind components. This will have a solution if and only if

$$\frac{\partial F}{\partial y} = \frac{\partial G}{\partial x} \quad . \tag{3.4}$$

In light of physical considerations (i.e., that friction and derivative terms cannot be exactly determined), this is solvable only in a least-squares sense. Doing so gives the Poisson PDE

$$\frac{\partial^2 p'}{\partial x^2} + \frac{\partial^2 p'}{\partial y^2} = \frac{\partial F}{\partial x} + \frac{\partial G}{\partial y} \quad , \tag{3.5}$$

which is subject to Neumann boundary conditions. A local steady state assumption is made to allow time derivative terms in the total derivatives to go to zero, and friction is considered negligible. The values of F and G are then calculated from the results of the

wind derivation and the Coriolis parameter (3.3). With F and G known, (3.5) is solved, allowing for an estimation of the horizontal pressure perturbation field.

Because the perturbations are derived from the computed wind fields, all of the errors discussed above affect their accuracy too. The pressure perturbation method itself assumes time derivate terms are trivial and ignores frictional effects to allow for a solution, but only a least-squares solution is possible. Technically, this does not provide an exact solution, and derived pressure gradients may not balance with the horizontal momentum equation. However, the method is instructive in assessing the pressure perturbation field as errors from these assumptions should be quite small in light of those possible in the derived (especially vertical) wind fields.

In total, 166 dual-Doppler analyses were performed on 16 features that propagated through the dual-Doppler lobes. For each, the pair of radar volumes investigated, size of the smaller domain, and which lobe the entity was located in are included in Table 3.1.

Table 3.1: Catalog of features analyzed in the dual-Doppler lobes. Values listed for vertical vorticity are that associated with the mesovortex at 1.5 km. When two values are given the number in parenthesis tells which MV each value is associated with. Values listed for the maximum vertical and horizontal velocities are that over the entire analysis domain at 1.5 km. [Note: * indicates the value occurs at the edge of the domain or along the baseline; " denotes the maximum vorticity value in the domain but is not associated with feature; ^ feature 13 does not contain a center separate from 10, nor does 11 from 07.]

Feature	KHGX time	MAX time	Analysis Time	Small domain size (km)	Lobe	Vorticity [x 10^{-3} s^{-1}]	Up [m/s]	Down [m/s]	Horizontal [m/s]
01	022917	022735	0228	30 x 30	SE	2.9	8.9*	11.5*	53.4
02	024614	024849	0247	30 x 30	SE	3.3	6.7*	13.2	47.2
	025140	024849	0250	30 x 30	SE	4.0	7.8*	7.7*	38.5
	025725	025614	0256	30 x 30	SE	4.2	4.4*	9.5	40.9
	030250	030556	0304	30 x 30	SE	3.3	14.8*	4.4	42.7
	043456	043224	0433	30 x 30	SE	6.2	11.2	29.8	56.4
	043941	044111	0440	30 x 30	SE	6.9	11.2	25.0	57.8
	044855	044957	0449	30 x 30	SE	7.6	12.7	13.9	55.8
	045809	045859	0458	30 x 30	SE	8.5	6.4	6.6	52.9
	050723	050738	0507	30 x 30	SE	3.7	6.6	8.3*	46.4
	051652	051625	0516	30 x 30	SE	4.1	14.1	5.8	39.9
	052606	052534	0525	30 x 30	SE	4.0	21.7*	7.7*	44.7
	062202	062049	0621	30 x 30	SE	4.2	5.3*	6.8	50.3
	062631	062945	0628	30 x 30	SE	5.1	5.5*	8.7	61.4
	063115	062945	0630	30 x 30	SE	5.5	6.1	7.9	55.5
	064030	064100	0641	30 x 30	SE	3.8	4.4*	6.2*	58.5
	065000	064957	0650	30 x 30	SE	4.4	2.7	6.2*	59.4
03	030250	030556	0304	30 x 30	SE	5.0	4.7	15.1*	49.1
	031419	031501	0315	30 x 30	SE	3.4	7.2*	5.6*	53.9
	032529	032644	0326	30 x 30	SE	4.7	12.1	10.6*	40.9
	050723	050738	0507	30 x 30	SE	5.7	17.8	20.8	62.3
	051652	051625	0516	30 x 30	SE	6.7	19.2	19.8	58.7
	052606	052534	0525	30 x 30	SE	8.2	7.7*	9.1	55.8

Table 3.1 continued

	084706	084809	0848	35 x 35	NW	5.0	4.6	4.3	53.0
	053520	053434	0535	30 x 30	SE	6.2	7.6*	7.5*	54.9
	055404	055408	0554	30 x 30	SE	5.6	9.4*	13.0*	43.5
	065429	065358	0654	30 x 30	SE	3.9	9.8*	5.1*	48.2
	070456	070316	0704	35 x 35	SE	5.2	5.0	6.0	52.4
	071411	071238	0713	30 x 30	SE	6.8	5.0	6.9	52.6
	072326	072200	0722	30 x 30	SE	6.8	3.1*	4.7	54.0
	072811	072854	0728	30 x 30	SE	5.4	6.8*	4.7	64.5
	074639	074740	0747	30 x 30	NW	6.0	11.0*	8.3*	50.8
	075554	075441	0755	40 x 40	NW	5.6	7.8*	5.8*	55.3
	080039	080148	0801	40 x 40	NW	5.6	6.6*	2.5	53.6
	080954	080830	0809	30 x 30	NW	6.5*	14.6	10.3	66.0
04	031419	031501	0315	30 x 30	SE	4.8*	7.6*	12.3*	71.7*
	032529	032644	0326	30 x 30	SE	4.7*	8.5*	9.5*	51.8*
	033640	033553	0336	30 x 30	SE	3.9*	6.7*	9.1*	41.7*
05	033640	033553	0336	30 x 30	SE	7.5*	6.9*	8.9*	49.2
	034807	034508	0348	30 x 30	SE	4.0	3.6	6.7*	43.4
	035351	035420	0354	30 x 30	SE	4.8	4.9	9.8*	49.7
	035934	040151	0400	30 x 30	SE	5.2	6.3	10.3	38.8
	055404	055408	0554	30 x 30	SE	4.1	7.1	10.1	57.8
	055833	060049	0559	30 x 30	SE	4.0	4.0	7.6	58.1
	060318	060049	0601	30 x 30	SE	4.2	6.0	4.9	58.5
	061247	061156	0612	30 x 30	SE	4.6	10.0	9.1	57.6
	071411	071238	0713	30 x 30	SE	7.5	10.6	9.2	48.1
	072326	072200	0722	30 x 30	SE	5.4	6.4	8.1	48.1
	072811	072854	0728	30 x 30	SE	6.6	5.8	6.8	55.6
	073725	073817	0738	30 x 30	SE	5.7	4.9	7.8	52.3
	074639	074740	0747	30 x 30	SE	5.3	3.4	4.0	54.4
	075554	075441	0755	30 x 30	SE	5.3	7.2*	4.8*	64.6*
	080954	080830	0809	30 x 30	NW	9.6*	8.0*	17.0*	89.4*
	081908	081952	0819	30 x 30	NW	5.3	4.4	3.1	50.3
	082839	082915	0829	30 x 30	NW	5.5	4.2	3.7*	51.7
	083752	083852	0838	30 x 30	NW	5.3	4.2	3.3*	51.7

Table 3.1 continued

	065429	065358	0654	30 x 30	SE	3.7	3.0	7.0	55.6
	090121	085936	0900	30 x 30	NW	5.8	21.7*	5.2	66.2*
06	035934	040151	0400	30 x 30	SE	4.8	11.1	20.1*	55.9
	041627	041453	0415	30 x 30	SE	3.2	8.5	7.0	42.7
	042541	042338	0424	30 x 30	SE	4.3	11.4*	12.8*	38.2
07	041627	041453	0415	30 x 30	SE	4.6	23.7*	19.0*	57.2
	042541	042338	0424	30 x 30	SE	5.0	10.8	17.0	55.8
	043456	043224	0433	30 x 30	SE	7.5	8.2*	7.0*	46.4
	043941	044111	0440	30 x 30	SE	4.3	15.2*	6.1	44.7
	055833	060049	0559	30 x 30	SE	3.2*	7.0	7.8	63.2*
	060318	060049	0601	40 x 40	SE	3.0	5.1	7.4*	57.6
	061247	061156	0612	40 x 40	SE	3.5	3.9	5.5	60.5
	062202	062049	0621	40 x 40	SE	4.1	12.3*	6.1*	66.9
	062631	062945	0628	40 x 40	SE	3.6	4.2*	4.2*	52.0
	072811	072854	0728	30 x 30	SE	5.6	7.4	4.9*	60.2
	073725	073817	0738	30 x 30	SE	5.2	8.3*	7.1	56.0
	074639	074740	0747	40 x 40	SE	5.0	7.9	5.0	52.1
	075554	075441	0755	40 x 40	SE	3.9	5.9	4.5*	46.7
	080039	080148	0801	40 x 40	SE	4.4	5.0	6.0*	55.2
	080954	080830	0809	40 x 40	SE	3.9	2.8	3.1	47.9
	081908	081952	0819	30 x 30	SE	4.0	6.0*	6.1*	53.3*
	084706	084809	0848	30 x 30	NW	4.5	4.2	3.5*	50.6
	090121	085936	0900	30 x 30	NW	3.2 (07), 5.0 (14)	4.1	6.1*	59.8
	091035	091048	0910	40 x 40	NW	3.1 (07), 6.0 (14)	5.3	7.1*	55.3
08	043456	043224	0433	30 x 30	SE	4.9	11.5*	10.6	56.3
	043941	044111	0440	30 x 30	SE	3.7	9.2*	9.8*	52.9
09	045809	045859	0458	30 x 30	SE	5.6	12.6	16.0	58.5
	050723	050738	0507	30 x 30	SE	6.2	12.1	15.5	56.9
	051652	051625	0516	35 x 35	SE	5.3	11.5	7.2	54.1
	052606	052534	0525	35 x 35	SE	5.8	7.1*	4.6*	50.6
	053520	053434	0535	35 x 35	SE	5.1	17.6*	8.1	43.9*
	063115	062945	0630	30 x 30	SE	8.0	5.6	9.0*	57.9*
	064030	064100	0641	30 x 30	SE	4.5	9.4	7.6*	54.0

Table 3.1 continued

	071411	071238	0713	30 x 30	SE	3.8	13.4*	4.7*	82.5*
	065914	070316	0702	30 x 30	SE	3.6	6.3	5.6	61.7
	070456	070316	0704	30 x 30	SE	3.5	5.0*	3.4	60.8
	072811	072854	0728	40 x 40	NW	5.2	8.2*	8.8*	52.8
	073725	073817	0738	30 x 30	NW	5.4	20.5*	9.8*	57.1
	080039	080148	0801	30 x 30	SE	6.3	5.9*	8.7*	61.7*
	080954	080830	0809	30 x 30	SE	4.3	9.4*	4.5	48.9
	081908	081952	0819	30 x 30	SE	4.9	6.0	3.7*	48.7
	082839	082915	0829	30 x 30	SE	4.4	4.4	6.6*	47.4
	083752	083852	0838	30 x 30	SE	4.7	3.5*	5.4*	49.7
	084706	084809	0848	30 x 30	SE	4.1	7.6*	3.5*	52.6
	091035	091048	0910	30 x 30	NW	3.8*	4.0*	10.0*	61.2*
	092434	092221	0923	30 x 30	NW	5.9	4.8*	5.3*	58.6
	093346	093330	0933	40 x 40	NW	5.1	5.2	8.5*	58.9
10	052606	052534	0525	30 x 30	SE	5.4*	26.9*	30.9*	60.5*
	053520	053434	0535	30 x 30	SE	5.9	14.6*	28.2*	60.5*
	055404	055408	0554	30 x 30	SE	8.6	5.9*	8.2*	54.8
	055833	060049	0559	30 x 30	SE	6.5	6.4	6.8	52.1
	060318	060049	0601	30 x 30	SE	7.6	5.4*	4.9*	51.4
	061247	061156	0612	30 x 30	SE	6.5*	16.0*	6.2*	51.5*
	065914	070316	0702	30 x 30	SE	8.7*	9.2*	6.9*	78.2*
	070456	070316	0704	30 x 30	SE	6.0	5.2	5.3	49.9
	071411	071238	0713	30 x 30	SE	6.7	5.0*	5.7*	50.7
	072326	072200	0722	30 x 30	SE	5.9	4.7*	4.6	54.3
	072811	072854	0728	30 x 30	SE	5.4	5.7	3.1*	54.4
	073725	073817	0738	30 x 30	SE	3.9*	7.7*	4.5	82.6*
	080954	080830	0809	40 x 40	NW	5.8 (10), 6.2 (03)	8.0	4.4	62.6
	081908	081952	0819	40 x 40	NW	5.2 (10), 6.2 (03)	11.8*	5.6	57.7
11	061247	061156	0612	30 x 30	SE	3.3	4.3	7.9*	61.2
	062202	062049	0621	30 x 30	SE	4.1	4.5	10.4*	59.5
	062631	062945	0628	30 x 30	SE	3.6	5.2	5.5*	63.5
	063115	062945	0630	30 x 30	SE	3.2	8.0*	3.7	65.4
12	070456	070316	0704	30 x 30	SE	6.5*	3.7*	3.7	52.6

Table 3.1 continued

	113038	113251	1131	30 x 30	NW	5.5”	5.0	6.8	37.6
	072326	073817	0738	30 x 30	NW	4.3*	4.4*	6.2*	49.6*
	074639	074740	0747	30 x 30	NW	5.6*	15.6*	10.6*	50.8
	083752	083852	0838	30 x 30	SE	3.5	5.5	3.9	43.2
	084706	084809	0848	30 x 30	SE	3.6	6.2	3.1	42.8
	090121	085936	0900	30 x 30	SE	2.4	4.4*	2.5	47.0
	092434	092221	0923	30 x 30	NW	4.3*	3.1*	3.1*	55.9*
	093346	093330	0933	30 x 30	NW	4.7	7.0*	5.2*	55.1
	094802	094912	0949	30 x 30	NW	3.8	6.1*	4.1	54.4
	100201	100051	1001	30 x 30	NW	5.3(12), 6.3 (09)	5.4*	8.4*	51.4
	101115	101236	1012	30 x 30	NW	4.2	5.6	9.6*	40.5
	102512	102443	1025	30 x 30	NW	3.9	5.4	9.9*	38.8
13	080954	080830	0809	30 x 30	NW	5.4 (10)^	4.8	4.5	54.3
	081908	081952	0819	30 x 30	NW	3.3 (10)^	4.2*	8.7*	52.1
	082839	082915	0829	30 x 30	NW	5.0 (10)^	4.5*	8.7*	50.6
14	083752	083852	0838	30 x 30	NW	4.0*	2.9	11.0*	63.9*
	084706	084809	0848	30 x 30	NW	4.6	3.5	2.0	49.7
	090121	085936	0900	30 x 30	NW	5.1	4.3	2.9*	57.6
	091035	091048	0910	30 x 30	NW	6.0	5.8	5.8*	52.9
	092434	092221	0923	30 x 30	NW	5.1	8.6	4.0*	57.0
	093346	093330	0933	30 x 30	NW	4.1	9.0*	6.1*	49.4
	094802	094912	0949	30 x 30	NW	3.7	7.4*	3.8	39.7
15	090121	085936	0900	30 x 30	SE	2.8*	7.1*	1.3*	34.0*
	091035	091048	0910	30 x 30	SE	5.1	5.9*	3.5*	46.3
	094802	094912	0949	30 x 30	NW	3.6	5.6	2.5*	50.1
	100201	100051	1001	30 x 30	NW	4.5	4.9*	2.9*	51.6
	101115	101236	1012	30 x 30	NW	4.4	5.3*	3.5*	44.7
	102512	102443	1025	30 x 30	NW	4.3	5.2	4.2	48.1
	103911	103949	1039	30 x 30	NW	5.8	4.9*	5.9*	50.8
	105312	105151	1052	35 x 35	NW	4.9	5.8*	4.7	45.4
	110225	110335	1103	35 x 35	NW	4.0	7.8	4.0	41.6
	111155	111315	1112	35 x 35	NW	3.6	7.8	5.9	39.1
	112109	112326	1122	30 x 30	NW	3.6”	6.2*	7.5	39.8*

Table 3.1 continued

	114421	114245	1143	30 x 30	NW	2.7”	6.6*	7.4*	38.3
	115352	115309	1153	30 x 30	NW	3.0”	3.2*	7.1*	40.7
	120308	120133	1202	30 x 30	NW	3.1”	6.2*	6.7*	43.7
	121222	121446	1213	30 x 30	NW	7.4*”	7.7*	5.6*	41.5
16	090121	085936	0900	30 x 30	SE	5.4	11.4	6.2*	39.7
	091035	091048	0910	30 x 30	SE	4.9	21.3*	3.7	42.4
	092434	092221	0923	30 x 30	SE	3.6*	11.4	2.6*	61.2*
	102512	102443	1025	30 x 30	NW	4.1	10.2*	5.1	38.3*
	103911	103949	1039	30 x 30	NW	4.0	10.3*	6.2*	35.0*
	105312	105151	1052	30 x 30	NW	4.9	8.8*	12.0	37.0
	110225	110335	1103	30 x 30	NW	4.0*	6.6*	8.0*	33.6
	111155	111315	1112	30 x 30	NW	3.4”	4.6*	6.7	22.0*

CHAPTER 4

EYEWALL EVOLUTION

To provide context for the work presented in this study, a synopsis of the evolution of Ike's eyewall just before and during landfall is given here. This description is based on visual changes in the Z field and is not intended to serve as an in-depth analysis. It is included merely for contextual purpose. Following chapters discuss results for the MVs that formed along the inside edge of the eyewall within the dual-Doppler domain (Table 3.1).

As noted previously, KHGX operated VCPs designed to mitigate range folding in the lowest elevation scans. This provided a range out to nearly 450 km during Ike's progression, thus KHGX was the first of the two radars to observe the eyewall. Before it entered the dual-Doppler lobes, the eyewall spiraled in on itself multiple times, similar to the episodes in Guillermo reported by Sitkowski and Barnes (2009). From about 0130 UTC on 12 September, however, the eyewall remained closed. As Ike approached and crossed the coast, the eyewall maintained a multiple MV regime. Many of the entities persisted for multiple revolutions about the eye, and production and maintenance of the MVs did not cease after the storm made landfall.

4.1 Within range of KHGX (2000 UTC 12 September - 0230 UTC 13 September)

The entire eye and eyewall entered the KHGX domain by 2000 UTC 12 September (see Figure 4.1a), and the ~100 km diameter eye region was generally echo free. The distinct eyewall had an open section at the northeast edge. There was a moat region to the northwest of the eyewall that became narrow 15 min later (Figure 4.1b). By 2030 UTC (Figure 4.1c) new returns developed in the northwest eye. With the northeast portion displaced inward slightly, the eyewall had taken on a letter "G" shape. At 2045 UTC (Figure 4.1d), the intensifying echoes in the western portion of the eye began to join the eyewall. These, along with the maintained "G" shape, resembled a new, smaller eyewall without a complete northern portion.

At 2100 UTC (Figure 4.1e), the inner echoes of the western eye were more dominant. Holes appeared between portions of the eastern eyewall, dividing it into three sections. The "G" shape remained, but by 2115 UTC (Figure 4.1f), the eyewall was very different. Its diameter decreased to about 75 km, encircled by quasi-regularly spaced "blobs" on all but the southeast portion. These features developed from the sections discussed in Figure 4.1e. They elongated and connected with each other so that by 2135 UTC (Figure 4.1g) they were part of the developing northwest eyewall. The "G" shape was less obvious as the inner, smaller eyewall formed. Nearly 10 min later (2144 UTC, Figure 4.1h), the newly formed band comprised the west to northwest portion of the still incomplete smaller eyewall.

The section circled in Figure 4.1h along the inner, northern edge of the eastern eyewall had an angled form, and may indicate an MV. This feature led the inward spiral of the eyewall seen at near 2200 UTC (Figure 4.2a). At this time, four sides of a

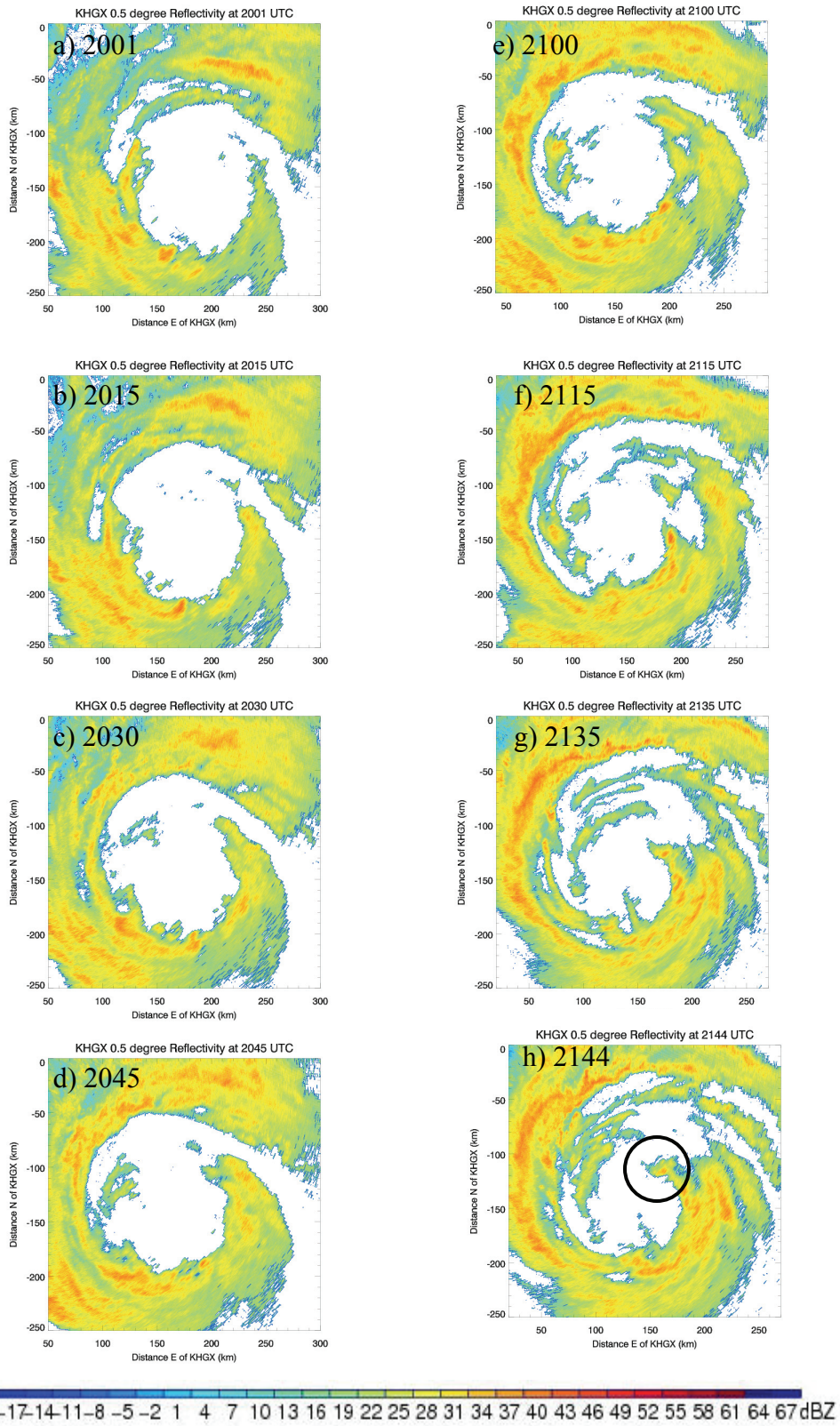

Figure 4.1: KHGX 0.5° reflectivity 2001-2145 UTC 12 Sept. [See text.]

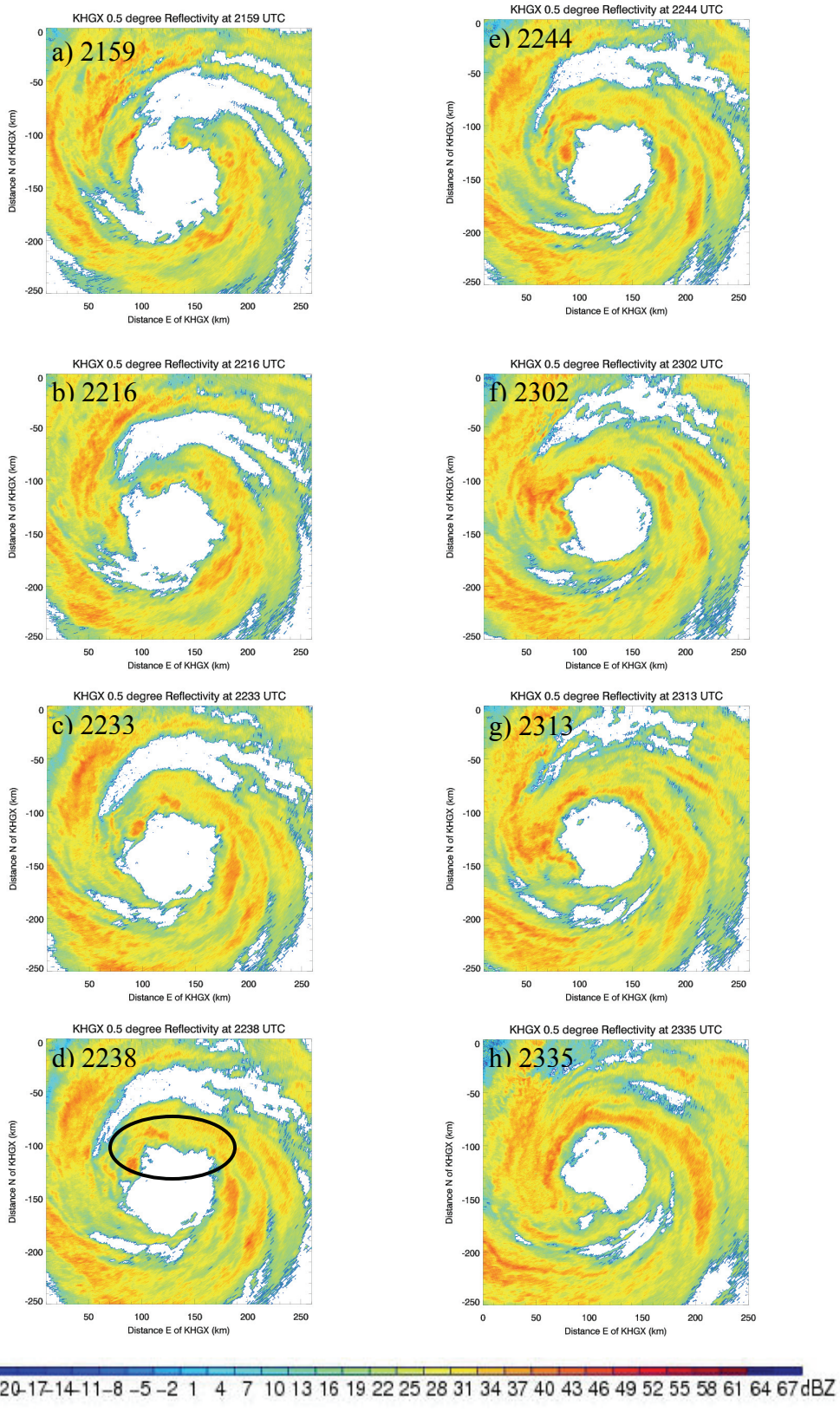

Figure 4.2: KHGX 0.5° reflectivity 2159-2335 UTC 12 Sept. [See text.]

nearly complete pentagonal shape were present. Just after 2215 UTC (Figure 4.2b), the inward spiraling edge from the E joined with the western side, closing the gap to the north. Echoes began developing in the southern part of the eyewall, with a ~25 km gap still evident in the southwest part of the new eyewall. It is possible that at least three MVs existed at this time: one near the leading edge of the eastern eyewall that has joined with the western side, and one each near the northeast and east vertices of the polygon.

The pentagonal pattern rotated cyclonically, and only a tiny open section remained in the southern eyewall at 2233 UTC (Figure 4.2c). In the next scan, the eyewall was complete with a diameter of about 75 km. The portion of the northern eyewall indicated in Figure 4.2d had a serpentine form. At 2244 UTC (Figure 4.2e), the formation persisted and the pentagonal shape started transitioning to a square. The vertex in the northwest portion of the eyewall at that time was the most distinct, forming nearly a right angle. Just after 2300 UTC (Figure 4.2f), this entity was in the western side of the eyewall, and the downwind Z took on an arced shape. This suggested the location of a possible MV downwind of the "kink" in the eyewall (as in KS01), and the curled formation of heightened Z suggested stronger localized updrafts, as shown by B06.

Just before 2315 UTC, the probable MV in the western eyewall was less obvious, but an arc in the Z persisted (Figure 4.2g). The southwestern eyewall began degrading, and the leading edge initiated another inward spiral. At 2335 UTC (Figure 4.2h) a triangular shaped eyewall emerged. The eye was echo free save for small areas to the northwest. A slight Z curl existed along the northwestern edge, and the southern portions of the eyewall did not line up as the detached southern eyewall progressed inward. In

12 min, the slight curl in the NW eyewall flourished and formed a near circle (2347 UTC, Figure 4.3a). The entity was again downwind of a vertex in the eyewall shape (north end of the triangle). Downwind portions of the eyewall were ragged, while upwind the inside edge of the eyewall was smooth. The diameter of the eye decreased to about 60 km.

At 2358 UTC (Figure 4.3b), the possible MV in the northwest eyewall was still evident but less defined, and the encroaching section to the S had clearly separated from the rest of the eyewall. Figure 4.3c shows that by 0015 UTC, the inward spiraling portion of the eyewall broke into two sections, and the northernmost piece had a hooked shape, circled in the figure. The triangle form of the eyewall began deteriorating, and an area in the north extended inward, toward the hook like feature. About 10 min later (0026 UTC 13 September, Figure 4.3d), the upper portion of the hook shape had nearly joined with the eyewall just upwind of the inward protrusion seen in Figure 4.3c. This formed a nearly circular feature, reminiscent of that discussed above at 2347 UTC (Figure 4.3a). The southern part of the hook formed its own, similar shape. These possible MVs were each about 15 km in diameter. The inward spiraling of the eyewall again resulted in a smaller eyewall.

Figure 4.3e shows that at 0038 UTC, the eyewall was open to the southeast, and increasing echoes developed near the lower portion of the previous hook feature. The southwest corner of the eyewall contained a new nearly circular echo free area along its inner edge, possibly another MV. At 0049 UTC, the broad triangle shape returned, and along the northern edge of the eyewall a stunning circular form (indicated in Figure 4.3f) developed from the earlier hook shape, about 15 km across. The likely MV was upwind of the northern vertex of the triangle shape. At the southwestern vertex, the other

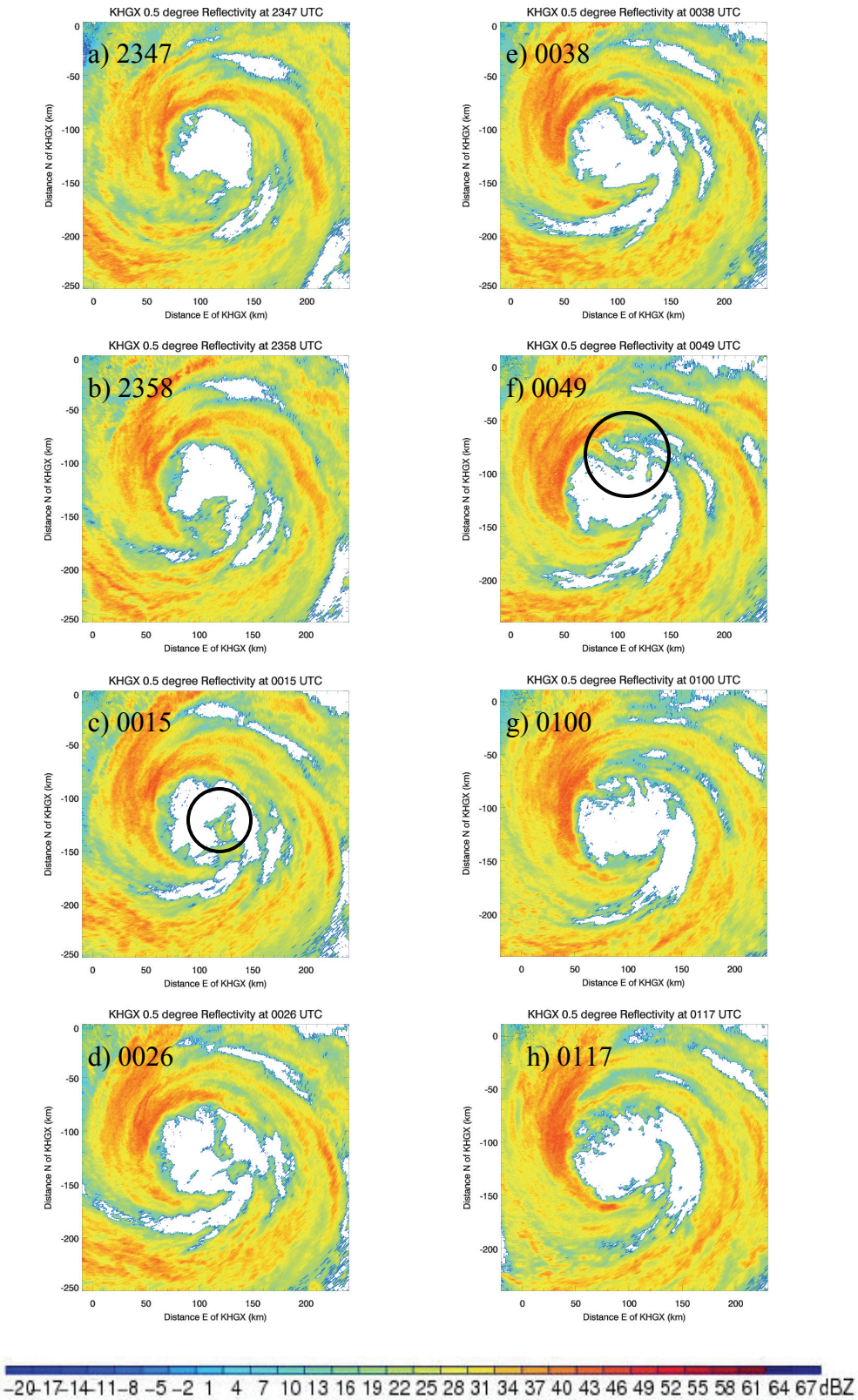

Figure 4.3: KHGX 0.5° reflectivity 2347 UTC 12 Sept.-0117 UTC 13 Sept. [See text.]

possible MV remained. The eastern portion of the eyewall was still open. The circular form in the northern eyewall maintained an echo free center and broadened by 0100 UTC (Figure 4.3g). Upwind of this, there were two protrusions from the inner edges of the northeastern eyewall. The triangle shape was becoming lost, but the feature to the southwest remained. As can be seen in Figure 4.3h, at 0117 UTC the circular form progressed downwind, and the inwardly spiraling section advanced to the east. There was about 20 km of gap in the northeastern eyewall. The Z signature of the possible MV in the southwest began to dissipate.

Near 0130 UTC (Figure 4.4a), the eyewall was essentially complete, and the echo free inclusion progressed further downwind to the west. At the northeast, a sharp turn in Z appears, circled in the figure. This developed over the next few minutes and by 0145 UTC the same feature was located near the northern corner of the square shape seen in Figure 4.4b. The diameter of the eye at this time was about 65 km, and the likely MV that previously contained an echo free area began to dissolve into the southwestern eyewall. At 0157 UTC (Figure 4.4c), the sharp Z curl formed the northwest vertex of a shape again transitioning from square to triangle. Inward protruding appendages in the north and west sections of the eyewall also indicated possible MVs. The triangle shape rotated cyclonically so that at 0214 UTC (Figure 4.4d) the vertex near the top of the shape at 0157 UTC (Figure 4.4c) was in the western eye. Parts of the eastern eyewall were thin, but by nearly 0230 UTC (Figure 4.5a) these broadened as the eyewall entered the dual-Doppler lobes.

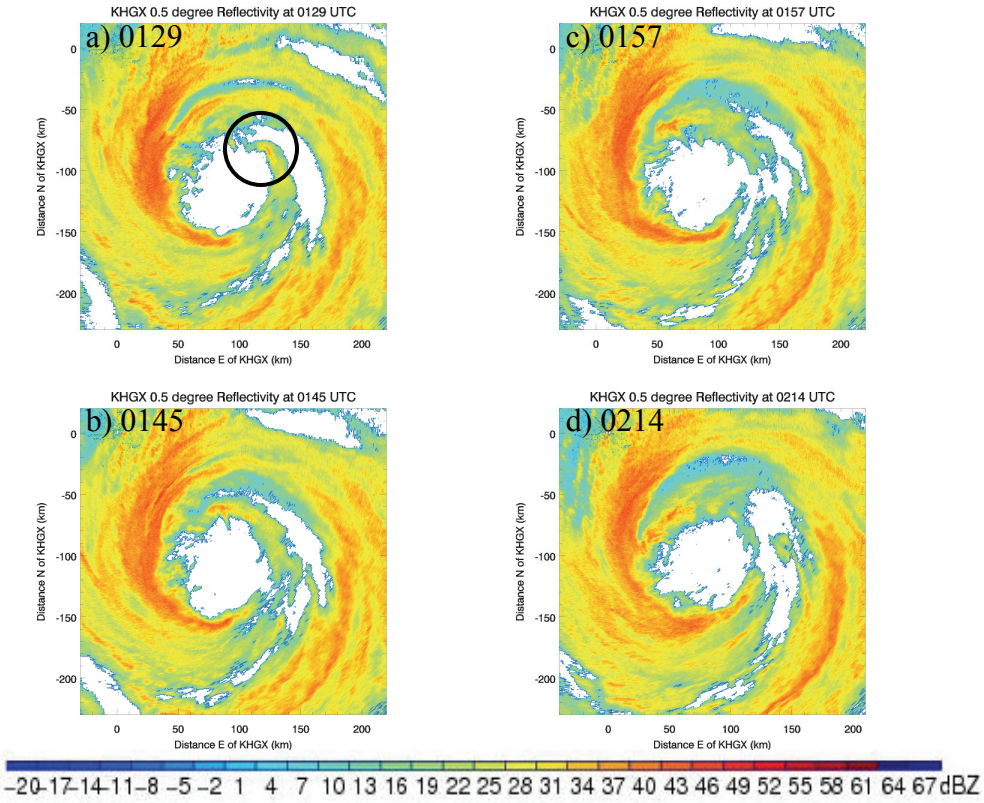

Figure 4.4: KHGX 0.5° reflectivity 0129-0214 UTC 13 Sept. [See text.]

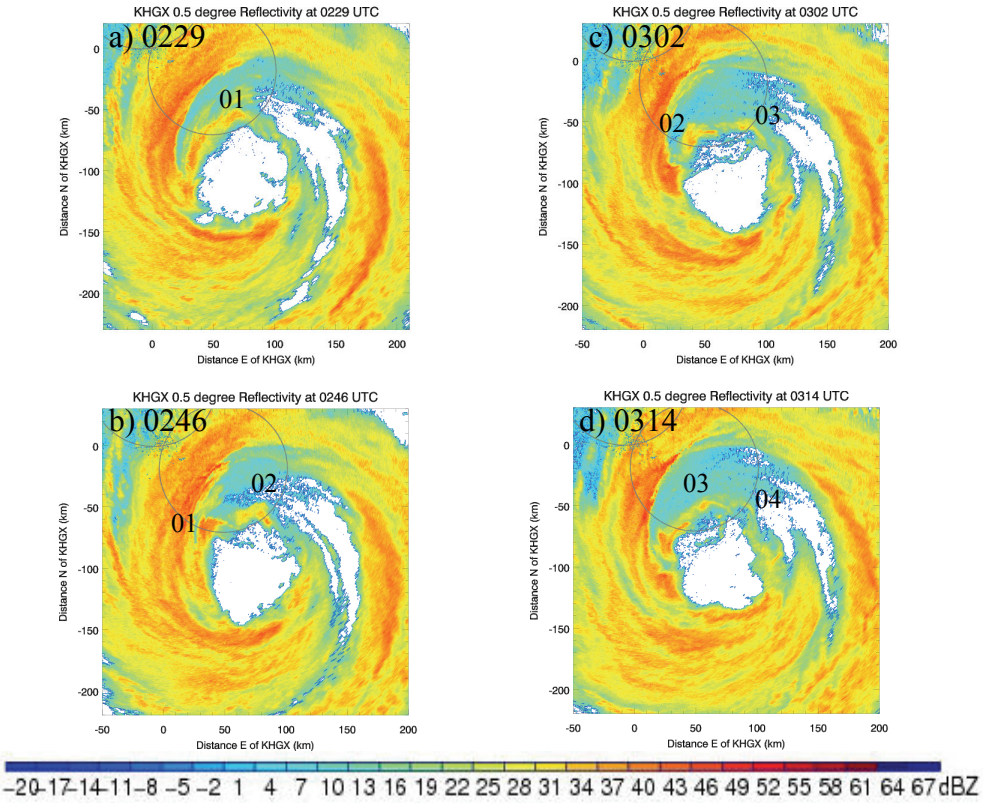

Figure 4.5: KHGX 0.5° reflectivity 0229-0314 UTC 13 Sept. [See text]

4.2 Within dual-Doppler lobes (0230-1300 UTC 13 September)

The dual-Doppler lobes are indicated on the remaining figures in this chapter. At 0229 UTC (Figure 4.5a), the northern vertex of the eyewall triangle was located just within the lobes. This marked the first feature used in the dual-Doppler analyses, MV01. Upwind, a new hook like feature developed. Arc shaped echoes have developed, attached to the southeastern eyewall. These echoes rotated along with the eastern side of the triangular eye. By about 0245 UTC (Figure 4.5b), a nearly complete oval shape formed the northern eyewall and contained a near right-angled section. This formed from the hook like area behind MV01, and having just crossed into the dual-Doppler domain, was labeled MV02. Southern and western portions of the eyewall maintained the triangle shape with few protuberant areas. Little change occurred over the next 15 min, and at 0302 UTC (Figure 4.5c) the triangle shape persisted. An area of 45+ dBZ sat along the southern vertex of the shape. The northern edge of the oval area from 0246 UTC contained two interesting features that formed obtuse angles: MV02, which started to exit the lobe, and MV03, which just entered the lobe. Upwind of the obtuse sections, an area of low Z encircled by higher values is present, and eventually became MV04. Each of these becomes significant in the proceeding chaotic transformation of the eyewall.

The three MVs mentioned above spread out rapidly over the next few minutes. Figure 4.5d shows them as three distinct bowed Z shapes in the northern eyewall at 0314 UTC. The area of heightened Z in the southern eyewall elongated and three markedly bowed Z sections formed. Radially outward from the eastern eyewall, a seventh arc occurred. By 0325 UTC (Figure 4.6a), the two bows in the southeastern eyewall merged, but the five other arcs endured, suggesting the presence of six possible

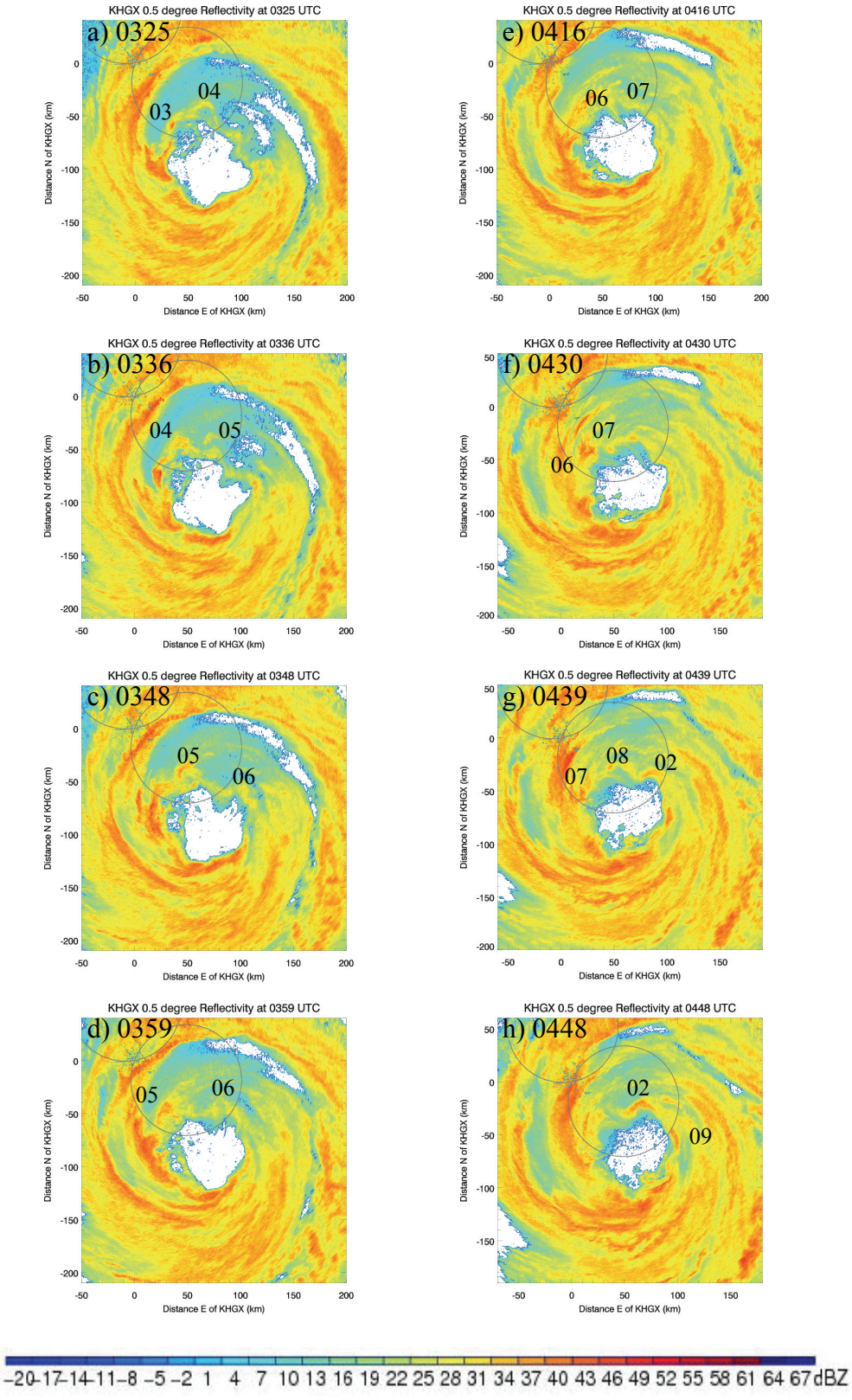

Figure 4.6: KHGX 0.5° reflectivity 0325-0448 UTC 13 Sept. [See text.]

MVs. About 10 min later (0336 UTC, Figure 4.6b) the seventh arc noted in Figure 4.5d comprised the upper portion of MV05 in the northern eyewall (upwind of MV04) at its first analysis time. All the MVs rotated cyclonically, but the three to the north remained closer together than the three to the S. Highest Z values (55 dBZ) were located in the western eyewall, along the edge of MV03. The southernmost bowed section of the eyewall (remains of MV01) was less evident after 0345 UTC (Figure 4.6c), while MV05 in the northern eyewall matured and the downwind portion of the probable MV06 (developing from the bowed section in the southeast of Figure 4.6a) in the northeast extended sharply into the eyewall.

Just prior to 0400 UTC (Figure 4.6d), MVs 03 and 04 weakened as they progressed southward. In the northwest eyewall, MV05 was still visible, and upwind probable MV06 maintained its nearly right-angled orientation. The bowed segment of the southern eyewall developed from MV02, and the shape of the eye once again approximated a triangle. About 15 min later (0416 UTC, Figure 4.6e), MV04 began to dissolve, and the leading edge of probable MV06 formed a small curled Z segment downwind of the sharp angle and an inward extending appendage upwind of the right angled section. Upwind of probable MV06, the first signs of MV07 entered the SW lobe at this time. By 0430 UTC (Figure 4.6f), MV07 continued to mature, and along the eastern eyewall MV02 began to strengthen. MVs 03 and 05 were still evident to the southwest. At this time the eye had an elliptical shape, approximately 65 km and 45 km across the major (E-W) and minor (N-S) axes, respectively. The form rotated over the next half hour with the MVs in place.

Figure 4.6g shows that by 0439 UTC MV02 reentered the SW lobe as the northeastern vertex of the oblate hexagon. Between here and the downwind MV07, a new bowed section developed into MV08. This MV did not persist, and seemed to merge with MV07. Itwas not visible at 0448 UTC (Figure 4.6h). Between MVs 02 and 03, another enhanced Z section formed and began to enter the SW lobe. This area evolved into MV09. Ten min later (0458 UTC, Figure 4.7a), MV02 maintained good positioning for dual-Doppler analysis, first analyses of MV09 were performed, and the leading edge of MV03 neared the SE lobe for the second time.

At 0507 UTC (Figure 4.7b), three features of interest sat within the SE lobe: MVs 02, 09, and 03. A triangular Z section that would become MV10 developed between MVs 03 and 05 (along the edge of the lobe) by 0516 UTC (Figure 4.7c). At this time, the northwest eyewall crossed the TX coast, but the MVs remained obvious. MV10 moved into the SE lobe by 0530 UTC (Figure 4.7 d), while MV02 began to leave. About 15 min later, MVs 03, 10, and 05 sat across the lobe, as the northern part of the oblate eyewall at 0554 UTC (Figure 4.7e). There was a larger leading portion associated with MV07, and to the west MVs 02 and 09 appeared less mature but still easily distinguishable.

Ten min later (0554 UTC, Figure 4.7f), MV05 was located adjacent to MV10. Around the rest of the approximately 60 km wide eye, MVs 03, 09, 02, and 07 persisted. By 0603 UTC (Figure 4.7g) these entities appeared crowded together in the lobe, but results indicated their continued independence. In the southern eyewall, MV02 became thinner and slightly elongated, while MV07 grew. This is obvious by 0617 UTC

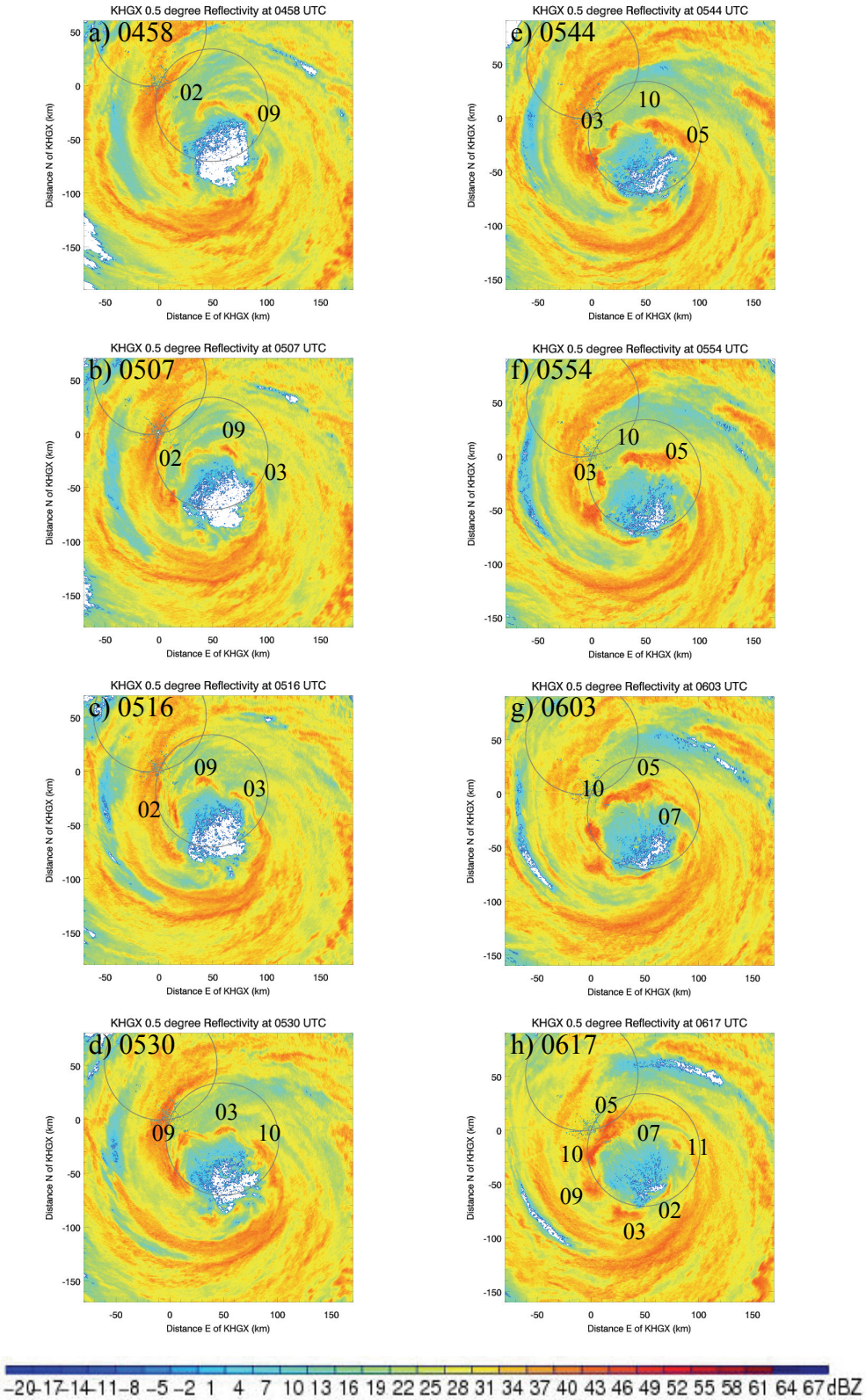

Figure 4.7: KHGX 0.5° reflectivity 0458-0617 UTC 13 Sept. [See text.]

(Figure 4.7h), as the clearer region of MV07 was about 20 km across. Elsewhere, MVs 05, 10, 03, 09, and 02 continued to rotate cyclonically with the system. A new, nearly right-angled portion of the inner eastern eyewall formed upwind of MV07. This short-lived section was investigated as feature 11 but not confirmed as an MV (i.e., it did not contain a vorticity signature). By 0631 UTC (Figure 4.8a), the eye had taken on a more symmetrical hexagon form approximately aligned along the SE lobe. Fifteen min later (0645 UTC, Figure 4.8b), the northwest eyewall was over Galveston Bay and nearly half of the eye had crossed the coastline. The hexagon had rotated but remained obvious, with an MV located near each vertex.

Ike's center crossed the Bolivar Peninsula at 0700 UTC, officially making landfall in the US. At about that time (Figure 4.8 c), MVs 07 and 02 were aligned along the baseline. Remaining in the SE lobe were MV09, which formed a near right angle, MV03, which developed a lower Z inner region, and MV10. MV05 also contained a lower Z region, but hugged the edge of the SE lobe. Between MVs 03 and 09, at 0709 UTC (Figure 4.8d), MV12 started to develop from an inward directed Z bow. MV05 reentered the lobe to the south, while MV07 skirted its western border and MV02 had become unidentifiable. At 0718 UTC (Figure 4.8e), MV05 was situated at the southern vertex of the eyewall. MV10 was at the southeast corner, and MV12 sat at the top. Between the latter, MV03 comprised the eastern eyewall.

Ten min later (0728 UTC, Figure 4.8f), the hexagonal eyewall elongated, with the positions of MVs 09, 10, 07, and 05 defining the northwest, northeast, southwest, and southeast vertices, respectively. At this time, MV09 entered the NW lobe for the first

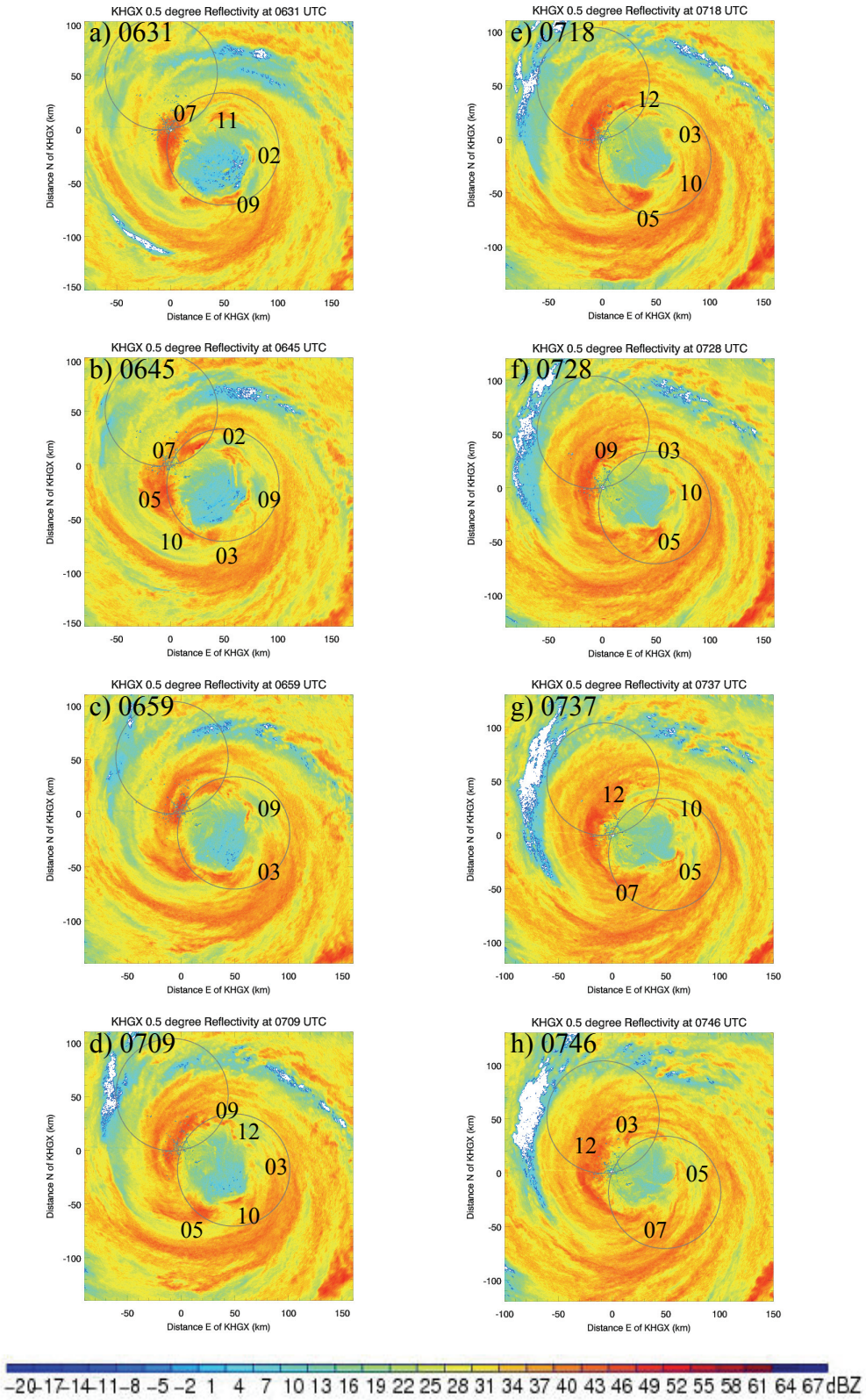

Figure 4.8: KHGX 0.5° reflectivity 0631-0746 UTC 13 Sept. [See text.]

analysis performed in that lobe, but it was near the baseline. In the SE lobe, the Z signatures of MVs 03 and 10 began to merge. About 10 min later, MV09 approached the edge of the NW lobe and MV12 sat very near the baseline in that lobe (0737 UTC, Figure 4.8g). At this time MVs 03 and 10 neared the northern edge of the SE lobe, but MV05 maintained good geometric placement, and MV07 came back into the SE lobe. By 0746 UTC (Figure 4.8h) MV03 is indistinguishable from MV10 in the Z field, and the eyewall's hexagonal shape began to wan. MV12 remained in the NW lobe, and MVs 05 and 07 in the SE lobe.

Once 0800 UTC arrived (Figure 4.9a), the eyewall once again took on a triangle form. At this time MV03 (after it was joined by MV10) was located downwind of the northern vertex, MV05 just upwind of the same corner, and MV07 near the southeastern vertex. Both MVs 09 and 12 occupied the southwest eyewall, with MV09 just inside the SE lobe and MV12 between the two lobes. A notch in the Z developed downwind of MV05 (upwind of MV03) and was examined as feature 13, but it did not contain a vorticity center. Nearly 15 min later (0814 UTC, Figure 4.9b), the entire eye had crossed the coastline. MVs 07, 09 and 12 were in the SE lobe, and MVs 10 and 05, along with non-MV13, were in the NW lobe. Radially outward from the thin band associated with MV07, an elongated area in the eastern eyewall degraded. By 0828 UTC (Figure 4.9c), MV07 (leading portion of the thin band) joined back to the downwind part of the eyewall and entered the NW lobe. MV05 and non-MV13 were also in this lobe at the time. In the SE lobe, MVs 09 and 12 remained and the hard-to-discern remnants of MV03 sat southwest of the baseline. By 0848 UTC (Figure 4.9d), non-MV13 had left the NW lobe, but MVs 05 and 07 where still distinct. Downwind of MV07, a new Z arc appeared.

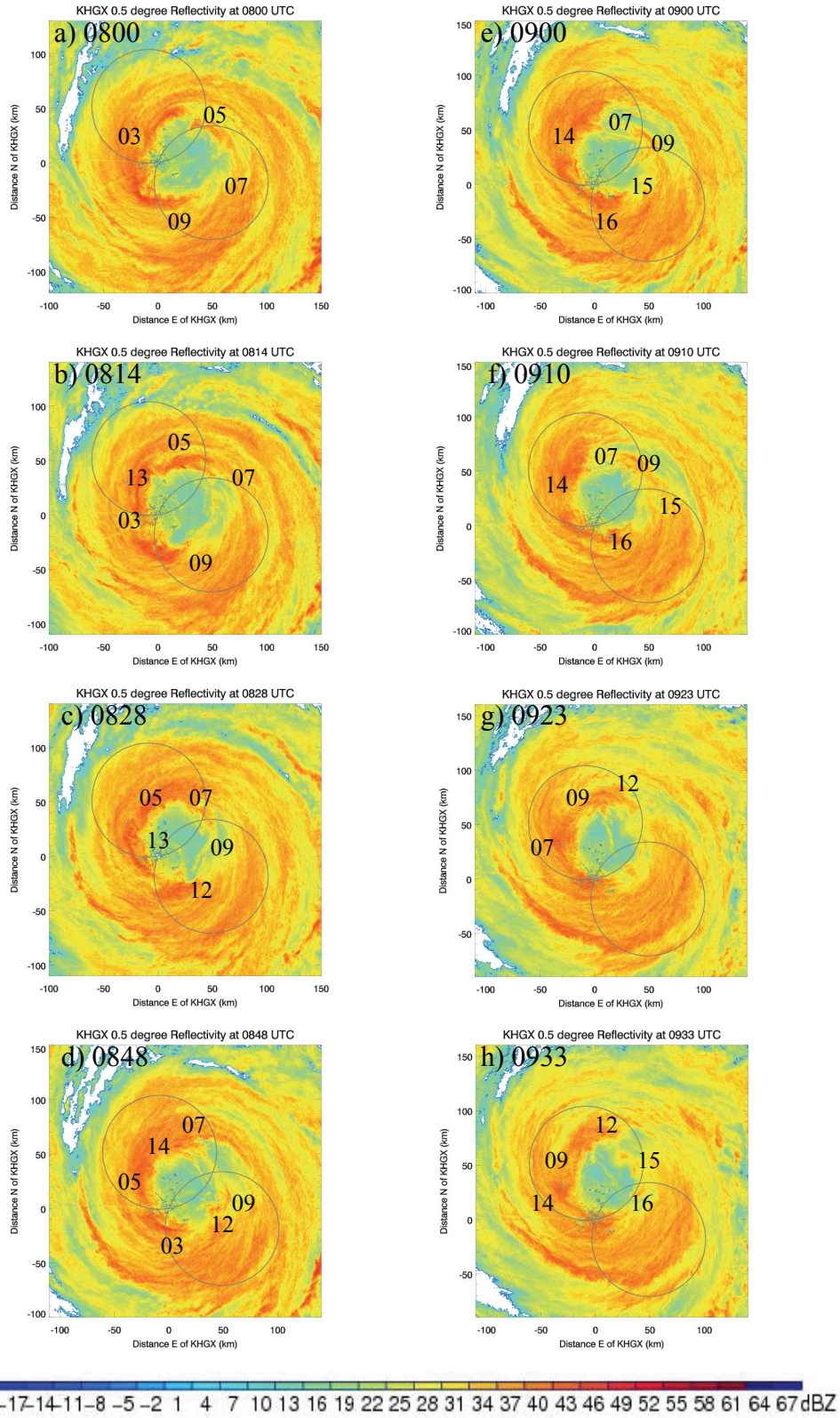

Figure 4.9: KHGX 0.5° reflectivity 0800-0933 UTC 13 Sept. [See text.]

This entity, much smaller than MV07, was MV14. MVs 09 and 12 remained in the SE lobe at this time.

At 0900 UTC (Figure 4.9e), the chaotic eyewall had a large dominant feature reminiscent of 0617 UTC (Figure 4.8h). This was again MV07. The clearer area adjacent to its upwind side developed from the moat region mentioned at 0814 UTC (Figure 4.9b). Upwind, MV09 formed a near right-angled shape near the northeastern edge of the baseline, and further upwind MV12 exhibited a nearly enclosed Z pattern. The arced Z signature upwind from MV12 is investigated as MV15, and behind it, what would become MV16 began to take shape near the boundary of the SE lobe. At this time, MV05 started to lose individuality in the Z field. By 0910 UTC (Figure 4.9f), MV07 had progressed to near the center of the NW lobe, but MV05 was indiscernible. MV14 moved on ahead of MV07. On the upwind edge of 09, 12 sat on the edge of the lobes. MVs 15 and 16 were the last features in the SE lobe. Thirteen min later (0923 UTC, Figure 4.9g), the eyewall was no longer dominated by MV07. It, along with MVs 14, 09, and 12 were contained by the NW lobe. A lower Z center appeared in MV09. At this time, the leading portion of MV15 entered the NW lobe (however, it was in the sector blocked out for the MAX truck cab).

At 0933 UTC (Figure 4.9h), MV12 had a more pronounced curl in Z at the northernmost portion of the eyewall. Downwind, MV09 began to diminish. MVs 15 and 16 were now both in the NW lobe, and MV14 was better defined in the southwestern eyewall Z. Figure 4.10a shows that by 0938 UTC MVs 12 and 15 were the most distinct features of the eyewall. In the S eyewall, 14 started to become less prominent. This was still the case at 0948 UTC (Figure 4.10b). At that time, MV15 appeared similar to how

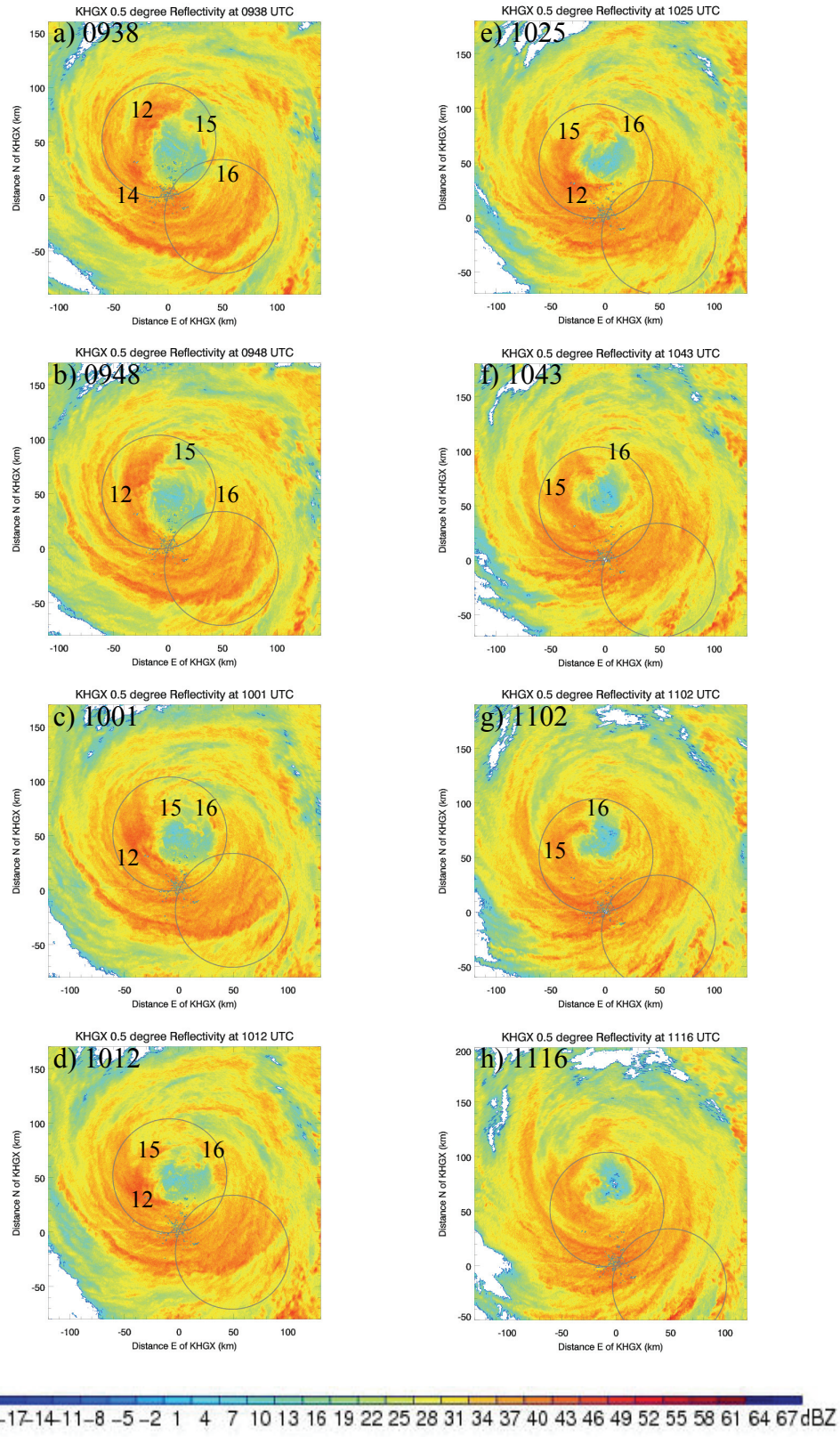

Figure 4.10: KHGX 0.5° reflectivity 0938-1116 UTC 13 Sept. [See text.]

MV07 did at 0617 UTC and 0900 UTC (Figures 4.8h, 4.9e), again in the same northeastern section of the eyewall. At 1001 UTC (Figure 4.10c), MV15 was still prominent in the northern eyewall. MV12 was now situated in the western eyewall. In the eastern eyewall, MV16 dominated. Along the baseline, another new arc shape formed. This developed to a likely MV at 1012 UTC (Figure 4.10d), but was not designated with a label in this study as it became ambiguous after leaving the area blocked out for the MAX truck cab (this also applied to later entities that appeared as the storm left the NW lobe). At this time, MVs 15 and 16 were in the northern eyewall, and MV12 displayed a vivid Z arc in the southwest eyewall.

Just before 1030 UTC (Figure 4.10e), MVs 15 and 16 prevailed in the northern eyewall. By this time, the unnamed feature noted at 1001 and 1012 UTC dissipated. In the southwest eyewall, MV12's arc shape became less marked. By 1043 UTC (Figure 4.10f), it was indistinguishable and MV16 was attached to the downwind side of the more pronounced MV15. About 15 min later (1102 UTC, Figure 4.10g), the eye appeared as two connected shapes: a smaller circle to the southwest bordering a N-S oriented ellipse. The southwestern section, really MV15, was about 15-20 km across, and the major axis of the ellipse was about 35 km. Figure 4.10h shows that by 1116 UTC this configuration rotated, and the northern eyewall began to exit the dual-Doppler domain.

By 1130 UTC (Figure 4.11a), the southern eyewall was all that remained in good placement in the NW lobe. The final analyses were performed on MVs 15 and 16 as they advanced to the edge of the resolvable domain. At 1144 UTC (Figure 4.11b), the Z associated with MV15 began to obscure the central eye. This effect was worse by

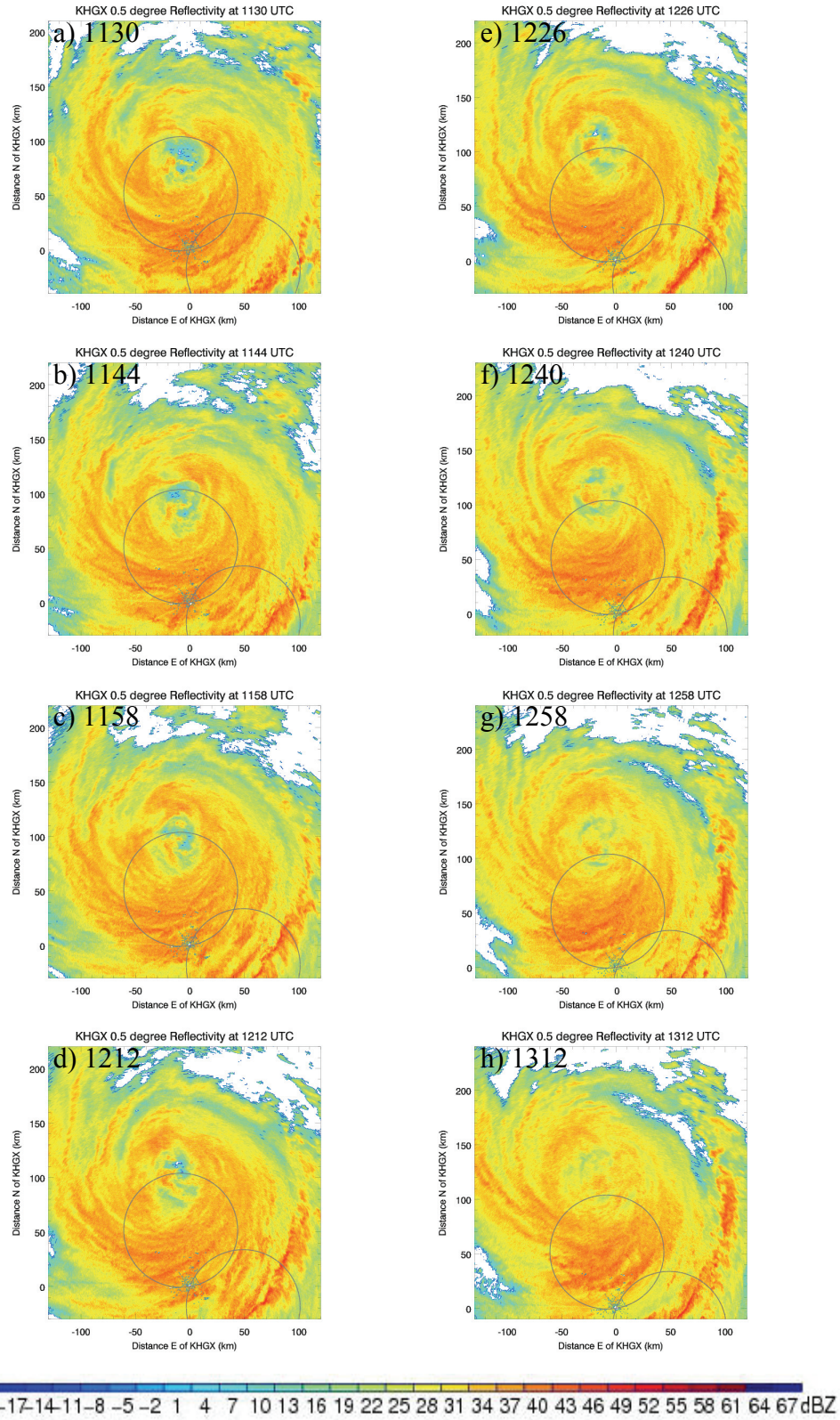

Figure 4.11: KHGX 0.5° reflectivity 1130-1312 UTC 13 Sept. [See text.]

1158 UTC (Figure 4.11c) and the triangle eyewall shape was lost. By 1212 UTC (Figure 4.11d) echoes extended across the eye. Figures 4.11e-h relay the progression of the eye and eyewall beyond the dual-Doppler lobes at 1226-1312 UTC. The central eye became increasingly obscured over this period as the hurricane moved inland.

Ike's eyewall evolution before and during landfall was complicated but not the first instance of such events. The multiple inward spiraling episodes of the eyewall resemble the transition of Guillermo's eyewall (Sitkowski and Barnes 2009). Prior to landfall, Ike was steered mainly by the subtropical ridge to its east and experienced moderate north to northeasterly shear (Section 2.2). Most MVs developed or strengthened as they moved though the upshear side of the eyewall, and their best Z appearance occurred on this N to NE side. Some completed multiple revolutions around the eye, and their behavior was akin to B06's conceptual model (Figure 2.4). Results for the analyzed features, most of which were confirmed as MVs (i.e., the entity was associated with a prominent local vorticity signature) are presented and discussed in the following chapters. Each pair of volume scans and the size of the small domain for each of the 166 dual-Doppler runs, along with values for resulting vorticity, vertical and horizontal winds, are listed in Table 3.1.

CHAPTER 5

RESULTS: RANGE OF MESOVORTEX STRUCTURAL CHARACTERISTICS

In total, 166 individual small domain analyses were completed. Only entities that demonstrated a clear local vorticity maximum in the low levels adjacent to the Z arc were deemed MVs, but some examined features did not meet this criterion. Horizontal characteristics at the 1.5 km level for each MV that passed through the dual-Doppler lobes and select Ike-relative radius-height sections through developed MVs are discussed in this chapter. The radius-height cross sections presented intersect the 1.5 km vorticity and vertical velocity maxima for high quality analyses of mature MVs (i.e., those located in a good geometry relative to the radars). The 1.5 km height was used to ensure the most complete sampling by both radars at the lowest possible heights. For features analyzed while at farther ranges (i.e., beyond about 60 km) from either radar, the lowest elevation sampled approaches 1 km, and is higher for farther ranges, especially for most MAX volume scans where the lowest elevation was 0.8°.

The goal of this chapter is to document the persistent, characteristic arrangements of the kinematic fields observed in Ike's eyewall MVs. The most outstanding result of this study is that arrangement of the MVs' vorticity and vertical velocity maxima progresses in a common fashion for each entity as it moves around the eye. Table 5.1 lists for each region of the eyewall the general locations of the aforementioned maxima

Table 5.1: Relative location of vertical velocity maximum to the MV vorticity center for various regions of the eyewall. Vorticity center generally occurs at the leading edge or near the center of the reflectivity arc. The SW eyewall is not listed because it was not as well sampled in the dual-Doppler lobes as other regions.

Eyewall Region	Maximum Vertical Velocity Location Relative to Vorticity Maximum	Examples: MV (Figure)
NE	E	07 at 0424 UTC (5.34)
N	Near	03 at 0535 UTC (5.13)
NW	W	05 at 0829 UTC (5.30)
W	SW	14 at 0910 UTC (5.68)
S	SW	07 at 0747 UTC (5.37)
SE	S	05 at 0728 UTC (5.19)
E	N	02 at 0630 UTC (5.5)

and examples of MVs that display each configuration. Figure numbers for each are given for convenience. Due to the configuration of the radars, extensive sampling of MVs in the SW eyewall was not possible, so MVs in this region are not included in the table. Recalling that Ike experienced a moderate amount (5-8 m s^{-1}) of northerly vertical shear in the hours prior to landfall (Section 2.2), the transitions of the favored updraft location are consistent with the conceptual model of B06 (Figure 2.4).

At 0700 UTC, Ike's center crossed the Bolivar Peninsula (i.e., made landfall) on the SE side of Galveston Bay. Features 12-16 developed after this time and are denoted herein as inland features or inland MVs. It is important to keep in mind that interaction with the coastline and changes to the hurricane as it moved inland and began weakening would have modified the dynamical processes generating and maintaining the MVs. Early in their existence, inland MVs exhibited characteristics akin to those that formed while at least half of the eyewall was still over the Gulf of Mexico, but obvious departures from the trends in Table 5.1 occurred in the inland MVs (e.g., Section 5.12).

5.1 Probable MV01

The portion of the eyewall that formed MV01 evolved from the SW corner of the square eyewall (left rear quadrant) at 0145 UTC. By 0229 UTC the eyewall was triangular in shape as MV01 entered the SE lobe (Figure 4.5a). After this time, its Z signature enhanced as it left the lobe. MV01 elongated by 0330 UTC and was indistinguishable shortly after. Unfortunately, there was only one analysis time available for this entity. Due to the location of MV01 near the far edge of the dual-Doppler region results for this time were not robust. There was a slight increase in the vorticity near the Z arc at 1.5 km, and a weak updraft/downdraft pair was collocated there. While not substantial at this time, a key result was the occurrence of outward (inward) radial flow on the upwind (downwind) side of the MV. Hand in hand with this, convergence near the middle of the Z curl and divergence at the leading side suggested a local modification to the cyclonic flow of the parent vortex. It will be shown that these characteristics are common among the entities analyzed throughout this chapter.

5.2 MV02

During the same square-triangle transition mentioned in Section 5.1, the hook like Z entity that formed MV02 appeared in the eastern eyewall (edge of the right front and rear quadrants) at 0214 UTC (Figure 4.4d). It passed through the SE lobe during the first four analysis times 0214-0304 UTC. Once MV02 exited the lobe it maintained individuality, and reentered the SE lobe for the next seven dual-Doppler runs starting at 0433 UTC. Within an hour it again moved outside the lobe, but as Ike moved toward the coast MV02 entered the lobe for its final analysis times from 0621-0641 UTC. MV02

completed two revolutions about the eye before it moved over the baseline and dissolved into the eyewall. It was visible for nearly 5 h.

Early analysis times for MV02 had similar difficulties as with MV01 in resolving the kinematic fields. The most optimal times for MV02 were 0458 and 0630 UTC, during its second and third trips through the SE lobe, respectively. Figures 5.1 and 5.4 provide context for the location of the smaller domains at these analysis times. Results for the 1.5 km vorticity and vertical velocity are given in Figures 5.2 and 5.5. In the earlier time, a pronounced vorticity maximum of 8.5 x 10^{-3} s^{-1} sat at the leading edge of the Z arc, and an updraft/downdraft pair straddled the E part of the arc with peak values of 6.4 m s^{-1} and 6.6 m s^{-1}. Figure 5.3 shows the radial component of the wind and the retrieved pressure perturbations at 0458 UTC. Localized inflow occurred on the downwind side and outflow on the upwind side of MV02, and contours of the retrieved pressure perturbation were nearly perpendicular to the radial wind, implying barotropic instability. Holton (2004) shows that barotropic instability can be thought of simply as a horizontal shear in the presence of a jet-like current. This is the case here as the radial wind component acts as a shear on the more prevalent tangential flow that would follow closed isobars, roughly parallel to the pressure perturbation lines in the figures.

Both radius-height sections indicated in Figure 5.2 are 20 km in length and begin 25 km from the center of Ike. Vertical sections of the vorticity, vertical velocity and flow along these lines are presented in Figures 5.7 and 5.8. Slight variations in 1.5 km values between the plan view and vertical cross section plots are attributable to the nearest-neighbor interpolation method used to generate the vertical sections. Highest vorticity in the vertical plane along the 332.2° azimuth occurred at the 1.5 km level (Figure 5.7).

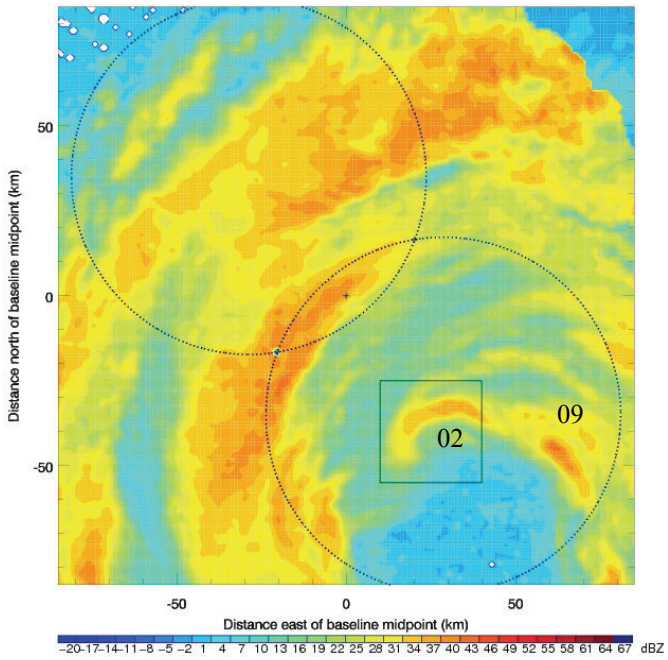

Figure 5.1: Context for 0458 UTC analysis of MV02.

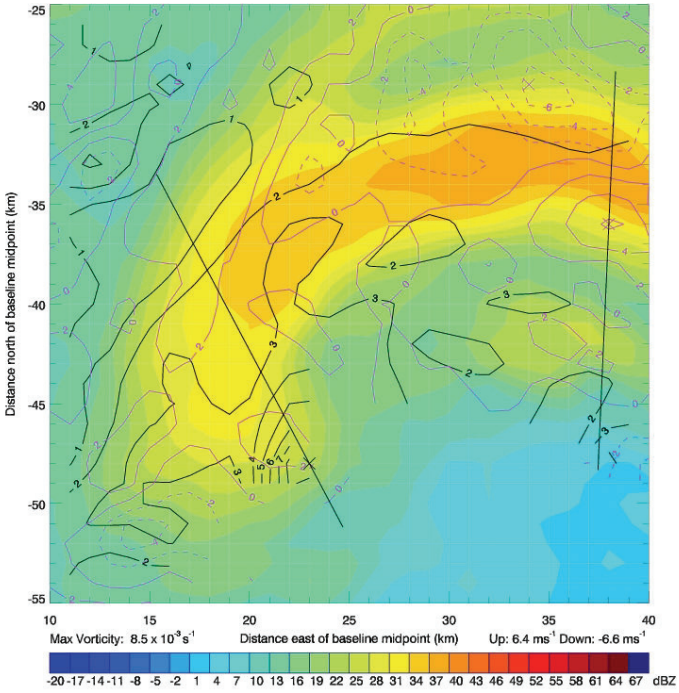

Figure 5.2: MV02 0458 UTC 1.5 km reflectivity (shaded, color bar), vorticity (black, x 10^{-3} s^{-1}) and vertical velocity (violet, m s^{-1}). Straight lines indicate vertical sections along Ike-relative radials at 332.2° and 2.5° azimuths extending 25-45 km in range from the storm center.

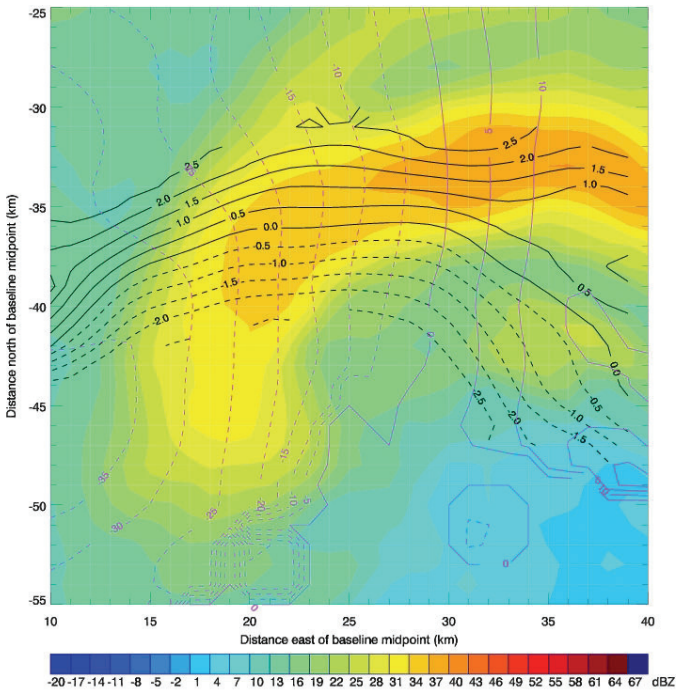

Figure 5.3: MV02 0458 UTC 1.5 km reflectivity (shaded), pressure perturbation (black, hPa) and radial wind (violet, m s^{-1}).

An area of elevated vorticity can be seen aloft at 8.5 km and 37-40 km range. The maximum updraft was 4.4 m s^{-1}, located at the 2.5 km height and 13 km radially outward from the vorticity center. The radial flow in this plane was inward at all levels. At the azimuth of maximum 1.5 km upward motion (2.5°, Figure 5.5) this direction was opposite at all heights, consistent with Figure 5.3. Peak vorticity in this vertical plane was 9.5 x 10^{-3} s^{-1} at the 8.0 km level, above the largest low level reflectivity of the MV. Maximum vertical motion was 6.5 m s^{-1}, located at the 3.0 km height on the inward side of the reflectivity signature.

During its third pass through the SE lobe, MV02 was situated in the eastern eyewall at 0630 UTC, as shown in Figure 5.4. Vorticity and vertical motion at this

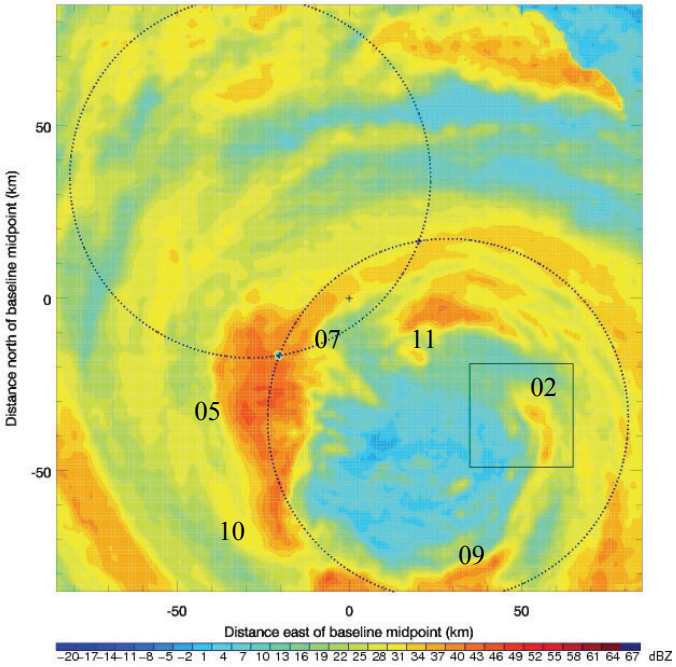

Figure 5.4: Context for 0630 UTC analysis of MV02.

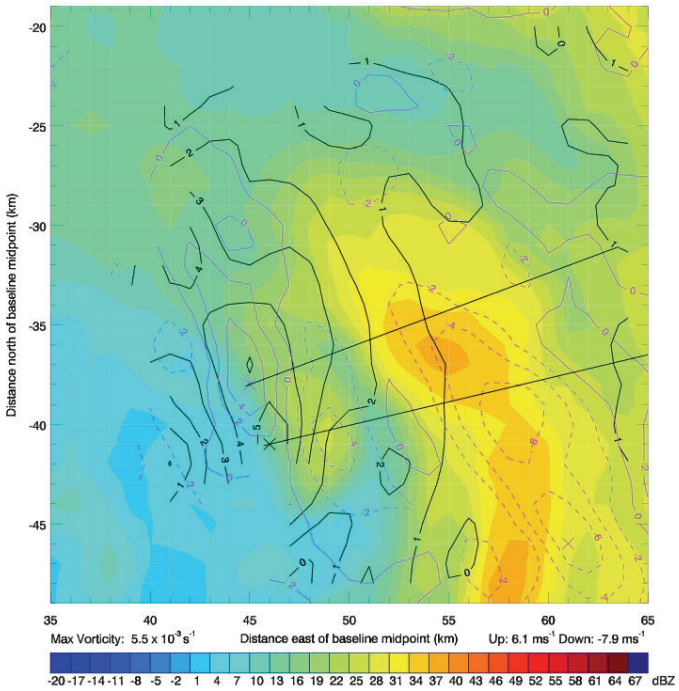

Figure 5.5: MV02 0630 UTC 1.5 km reflectivity (shaded, color bar), vorticity (black, x 10^{-3} s^{-1}) and vertical velocity (violet, m s^{-1}). Straight lines indicate vertical sections along Ike-relative radials at 76.7° and 69.5° azimuths extending 25-45 km in range from the storm center.

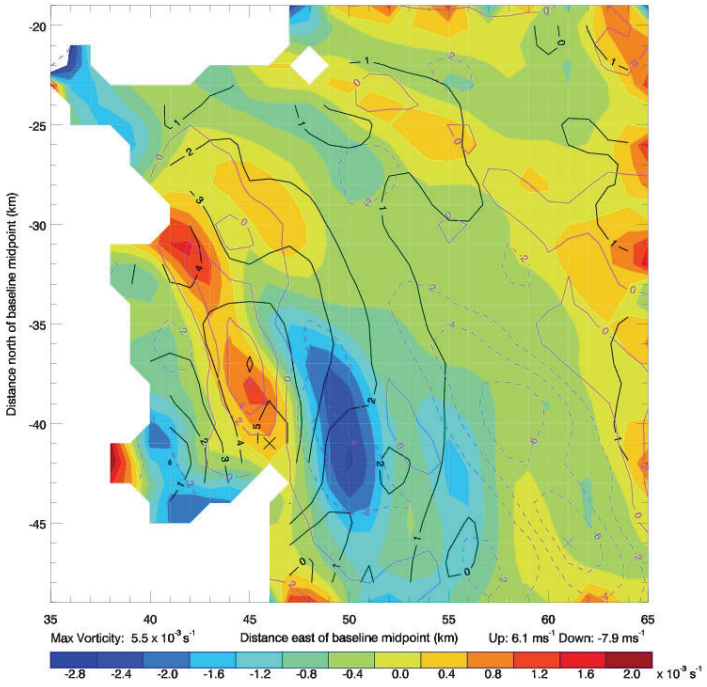

Figure 5.6: MV02 0630 UTC 1.5 km divergence (shaded, color bar), vorticity (black, x 10^{-3} s^{-1}) and vertical velocity (violet, m s^{-1}).

time (Figure 5.5) depicted an updraft/downdraft pair at the front portion of MV02, near the vorticity maximum, as opposed to over the heightened reflectivity as in the previously discussed time. Here, the trailing region of the mesovortex was characterized by downward motion. Figure 5.6 shows convergence to the right of the vorticity peak, just upstream of the vertical velocity maximum. The presence of divergence at the leading part of MV02 agreed with the configuration in the MV01 analysis.

The radius-height sections indicated in Figure 5.5 are 20 km long and begin at 22 km range from the storm center. Along the 1.5 km vorticity peak line (76.7°, Figure 5.9), maximum vorticity in the vertical plane remained at the 1.5 km height, and the largest upward motion value (2.1 m s^{-1} at 3.5 km height) occurred 2 km radially

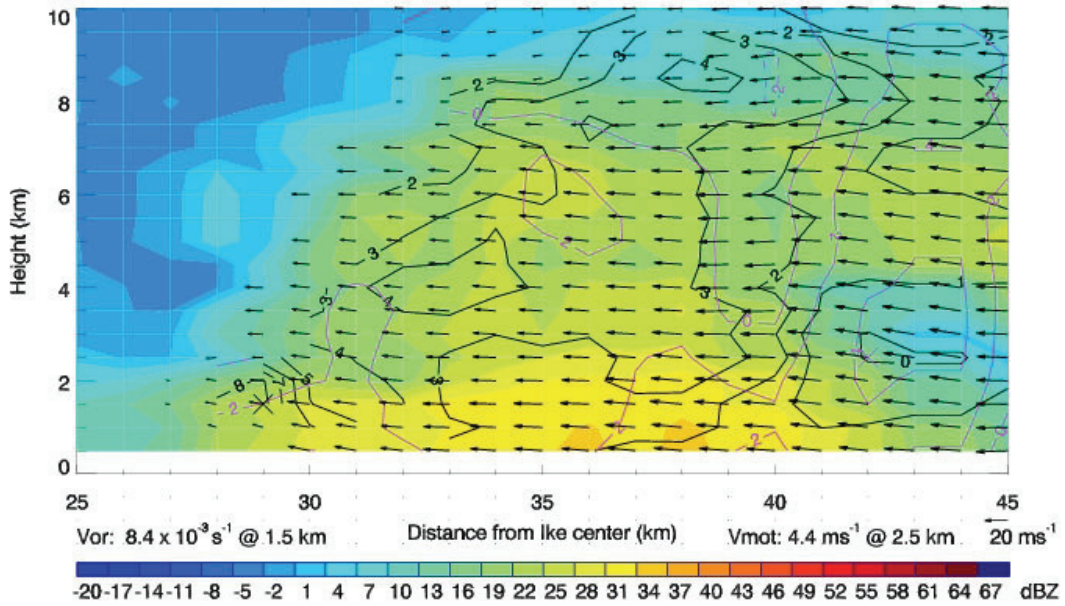

Figure 5.7: MV02 0458 UTC Ike-relative 332.2° azimuth reflectivity (shaded, color bar), vorticity (black, x 10^{-3} s^{-1}), vertical velocity (violet, m s^{-1}) and wind vectors (scaled 20 m s^{-1} vector above color bar).

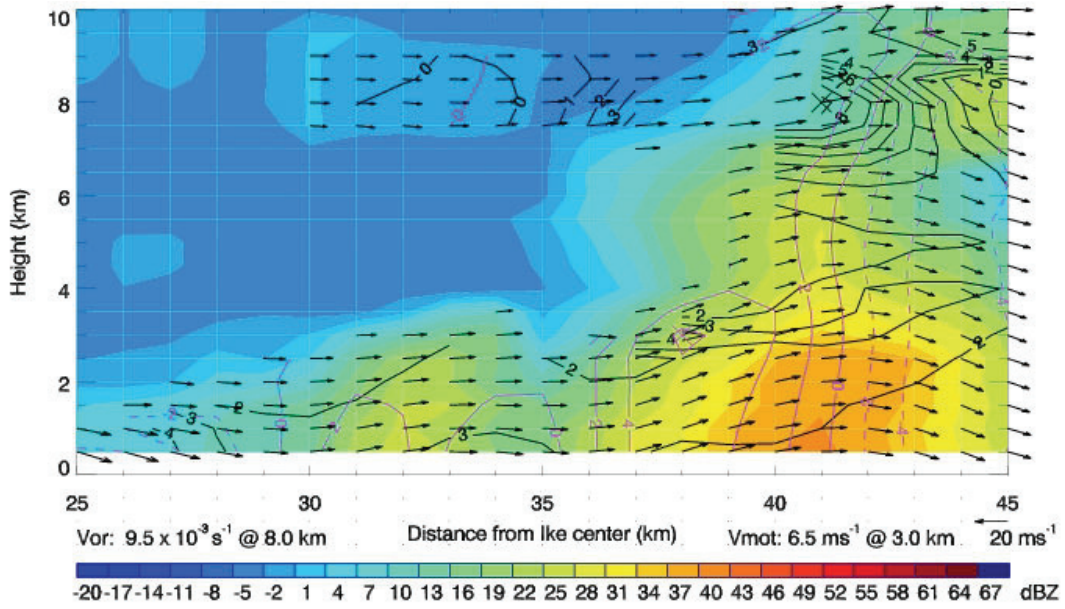

Figure 5.8: MV02 0458 UTC Ike-relative 2.5° azimuth reflectivity (shaded, color bar), vorticity (black, x 10^{-3} s^{-1}), vertical velocity (violet, m s^{-1}) and wind vectors (scaled 20 m s^{-1} vector above color bar).

inward form there. The cross section for the plane through the 1.5 km updraft maximum (69.5° azimuth) is shown in Figure 5.10. The largest vorticity was 6.3 x 10^{-3} s^{-1}, located at the 3 km height, above the innermost part of the Z signature. Areas of slightly enhanced vorticity at the 4 and 6 km levels were also present. The flow in both azimuthal planes was outward up to about 33 km range and radially inward beyond this. The prominent leading updraft and the elongated region of downward motion over the highest Z signature of MV02 (refer to Figure 5.8) were clear in both vertical planes. Figure 5.11 shows the divergence field along the 69.5° azimuth. Elevated divergence (convergence) is depicted by multiple closed contours above this updraft (downdraft), consistent with expectation.

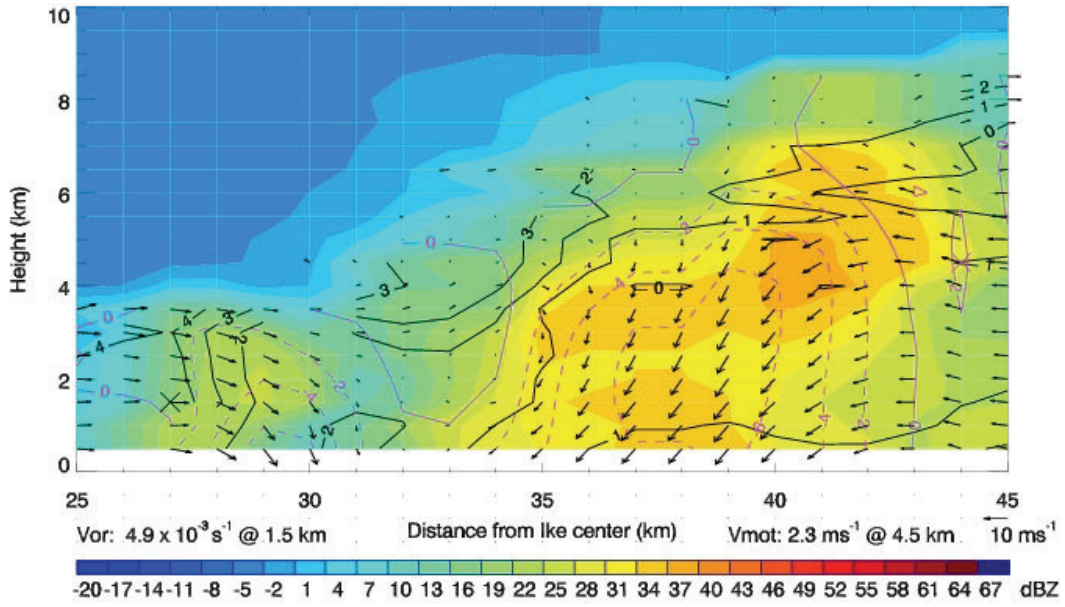

Figure 5.9: MV02 0630 UTC Ike-relative 76.7° azimuth reflectivity (shaded, color bar), vorticity (black, x 10^{-3} s^{-1}), vertical velocity (violet, m s^{-1}) and wind vectors (scaled 10 m s^{-1} vector above color bar).

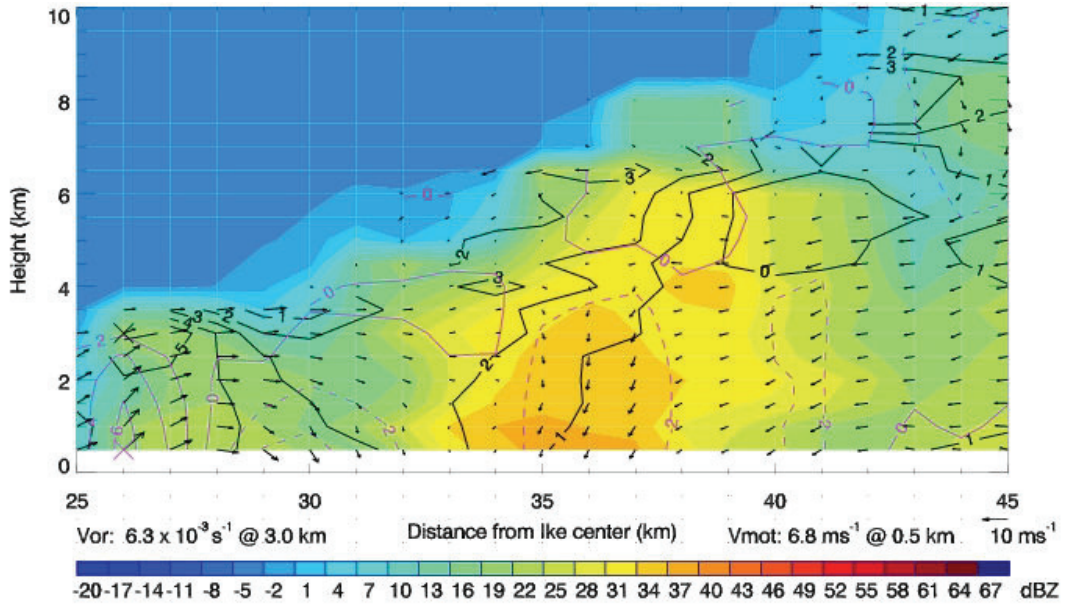

Figure 5.10: MV02 0630 UTC Ike-relative 69.5° azimuth reflectivity (shaded, color bar), vorticity (black, x 10^{-3} s^{-1}), vertical velocity (violet, m s^{-1}) and wind vectors (scaled 10 m s^{-1} vector above color bar).

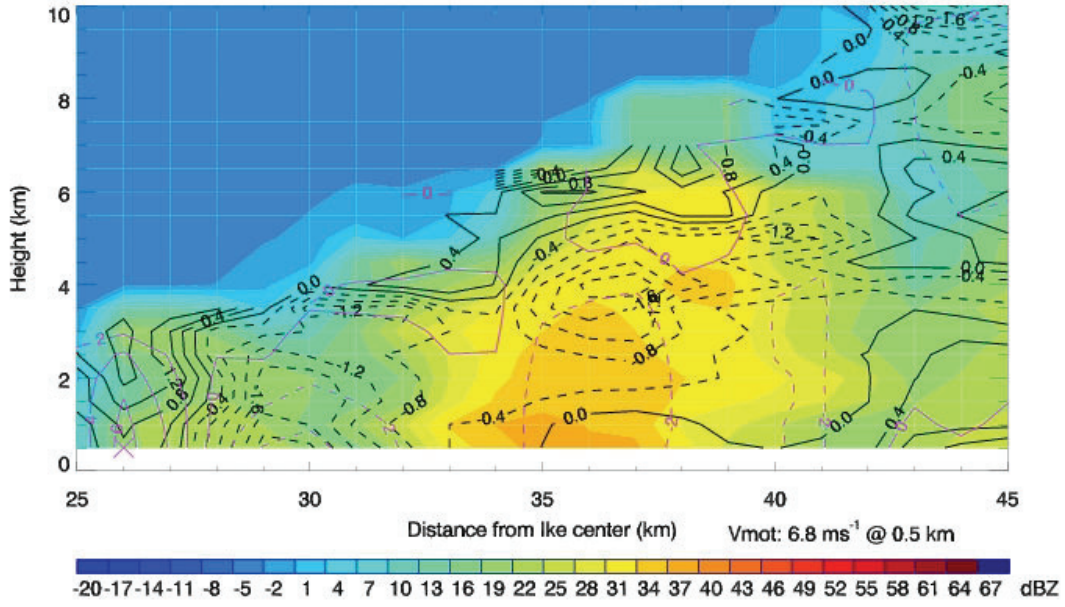

Figure 5.11: MV02 0630 UTC Ike-relative 69.5° azimuth reflectivity (shaded, color bar), divergence (black, x 10^{-3} s^{-1}) and vertical motion (violet, m s^{-1}).

5.3 MV03

Near when MV02 first entered the SE lobe, a new bowed section of inner eyewall Z formed at 0250 UTC (Figure 4.5c) in the northeastern eyewall (right front quadrant) and became MV03 as it traveled toward the SE lobe. Over the next 5 h, MV03 completed more than two full loops around the eye. Four sets of analyses were completed. The first was for 0302-0325 UTC, when MV03 moved through the northern eyewall at far extent of the SE lobe. Next was 0507-0554 UTC, as it traveled from the E to the W side of the eyewall. The most optimal geometry for MV03 occurred during this period (see Figure 5.12). MV03 later entered the SE lobe in the S portion of the eyewall and progressed N from 0654-0728 UTC. It neared the baseline at 0730 UTC and continued around the eye inside the NW lobe long enough for a few more dual-Doppler runs between 0747-0809 UTC. During this last time frame MV10 merged with it. After this, MV03 moved toward the S eyewall and was obscured by about 0815 UTC.

Distance from the radars and the presence of an intense rainband between them and MV03 led to incomplete results for the early analysis times. Of note, however, is that the peaks in both vorticity and updraft were nearly collocated at the leading portion of the MV for all the early analyses. As MV03 traversed the SE lobe for the second time, results were more robust. Vertical motion at early analysis times for this pass (i.e., 0507 and 0516 UTC) was most vigorous at the trailing, eastern end of MV03 than at its leading portion. Magnitudes of these updrafts were about 18 m s^{-1}, which is quite impressive considering previous work on the vertical motion in hurricanes. Using flight level (varying from 0.5-6.1 km) data from over 100 aircraft eyewall penetrations in four mature TCs, Jorgensen et al. (1985) found maximum velocities in the top 10% of eyewall

updrafts (downdrafts) rarely exceeded 9 m s^{-1} (6 m s^{-1}). Black et al. (1996) used airborne Doppler velocity data from seven Atlantic hurricanes to show that over 70% of vertical motions fell within the ± 2 m s^{-1} range, and only about 5% of eyewall vertical velocities exceeded 5 m s^{-1}. Many of the vertical velocities reported here (Table 3.1) exceeded these values, but care needs to be taken when viewing them as there are multiple sources of error inherent in their retrieval.

The most optimal location of MV03 occurred at 0535 UTC (Figures 5.12), when it was in the N of the elliptical eye. At this time, Figure 5.13 shows peak 1.5 km vorticity at 0535 UTC was 6.2 x 10^{-3} s^{-1}, just inward of the maximum upward velocity of 6.8 m s^{-1} (a higher value occurred near the edge of the domain). An additional updraft/downdraft pair slightly smaller in magnitude existed at the trailing end of the MV. Consistent with characteristics of previous entities, Figure 5.14 shows that the divergence field indicated converging flow into the center and diverging flow ahead of MV03. Contours of the radial wind in the same figure are nearly perpendicular to those of the retrieved pressure perturbations and indicate radially outward flow on the eastern part of MV03 and radially inward flow at the W side. These results paint a consistent picture of the impact of the mesovortex on the primary cyclonic flow and the secondary circulation of the hurricane.

Because the vorticity and vertical velocity maxima occurred very near each other at 0535 UTC, the two radial planes indicated in Figure 5.13 contain nearly identical results. The line along 341.1° intersects the 1.5 km vertical motion maximum. Figure 5.15 shows the flow in this plane and the vorticity and vertical velocity contours. Largest vorticity occurred at the lowest level of the domain, within a 4 x 10^{-3} s^{-1} contour

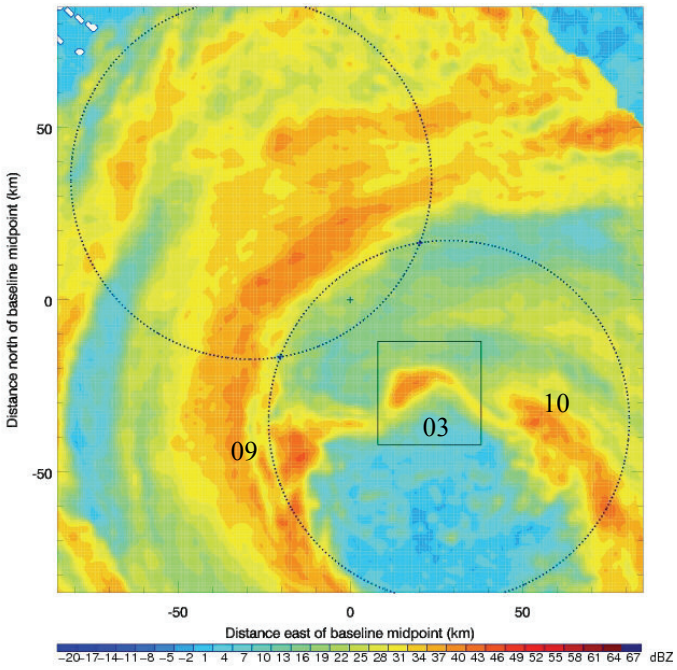

Figure 5.12: Context for 0535 UTC analysis of MV03.

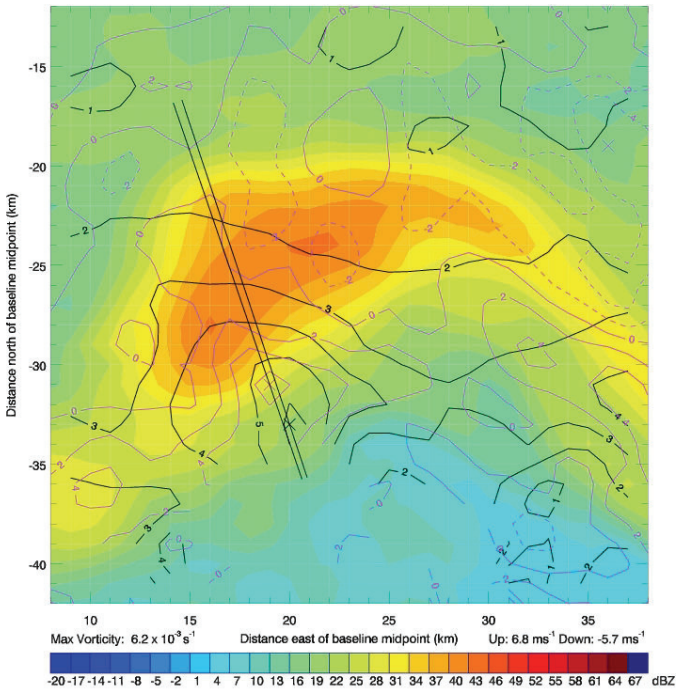

Figure 5.13: MV03 0535 UTC 1.5 km reflectivity (shaded, color bar), vorticity (black, x 10^{-3} s^{-1}) and vertical velocity (violet, m s^{-1}). Straight lines indicate vertical sections along Ike-relative radials at 341.7° and 341.1° azimuths extending 30-50 km in range from the storm center.

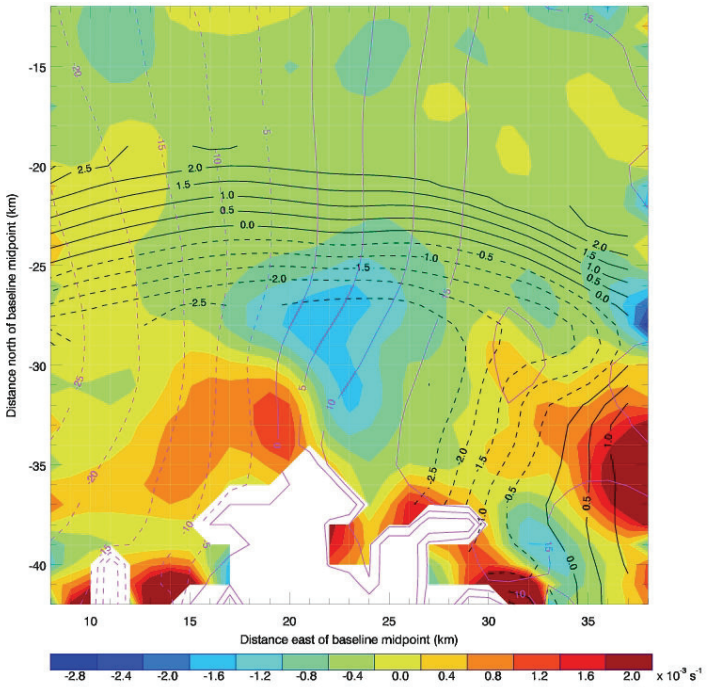

Figure 5.14: MV03 0535 UTC 1.5 km divergence (shaded, color bar), pressure perturbation (black, hPa) and radial wind component (violet, m s^{-1}).

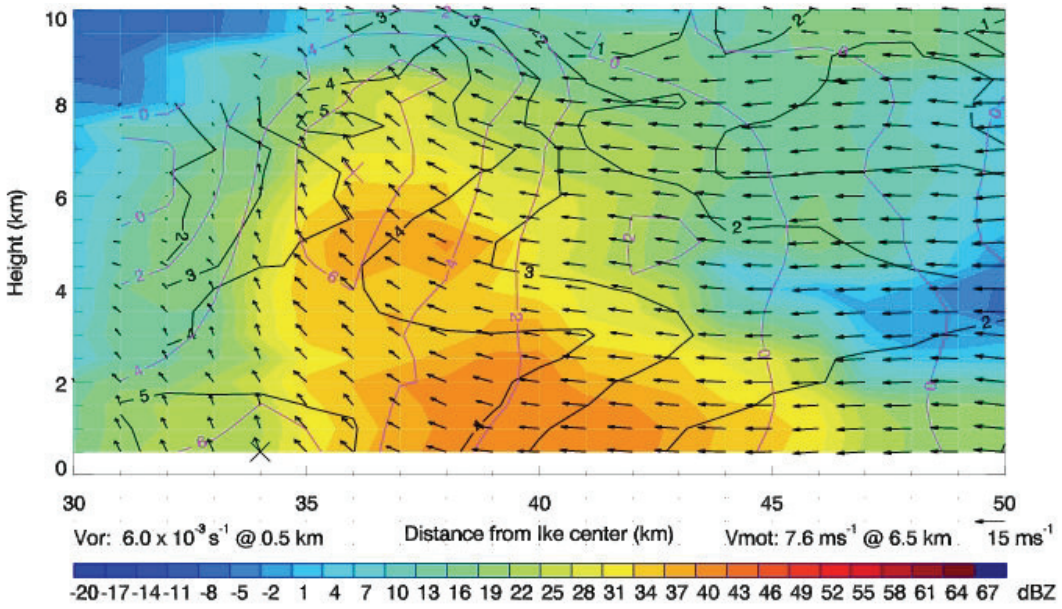

Figure 5.15: MV03 0535 UTC Ike-relative 341.1° azimuth reflectivity (shaded, color bar), vorticity (black, x 10^{-3} s^{-1}), vertical velocity (violet, m s^{-1}) and wind vectors (scaled 15 m s^{-1} vector above color bar).

extending up past the 8 km level along the inward side of MV03. A secondary vorticity peak existed above and radially inward from the updraft maximum. Wind field vectors depicted inward and upward motion across the sections, consistent with Figure 5.14 and the characteristic TC deep layer inflow. The largest vertical motion occurred near the center of the 4 x 10^{-3} s^{-1} contour at 6.5 km, and a closed 5 x10^{-3} s^{-1} contour appeared above and inward of the updraft maximum. The elevated vorticity aloft can be ascribed to the stretching of the column by the updraft and the tilting imparted on it by the inward component of the wind, as well as the vertical advection of the large low level vorticity by the updraft.

At 0654 UTC, MV03 entered the SE lobe for a third time (Figure 4.8c). As MV03 moved through the eyewall, the orientation of the vertical velocity maximum relative to its vorticity center changed. A brief account is provided here, and similar results found for later MVs in better locations in the lobes are shown later in this chapter. When MV03 was in the southeastern and eastern eyewall, the vorticity maximum was near the middle of the arc in Z and the largest updraft velocities were radially outward from the vorticity peak. With the MV N of Ike's center, the maximum updraft was located at the front of the MV, ahead of the vorticity center, which was still in the central part of the Z signature. Once MV03 crossed near the baseline and reached the northwestern eyewall just before 0800 UTC, the updraft moved to the SE of the vorticity center. At this point, the merger of MV10 into MV03 began. Early analyses showed two vorticity centers, each with a convergence/divergence couplet, but these quickly meshed together.

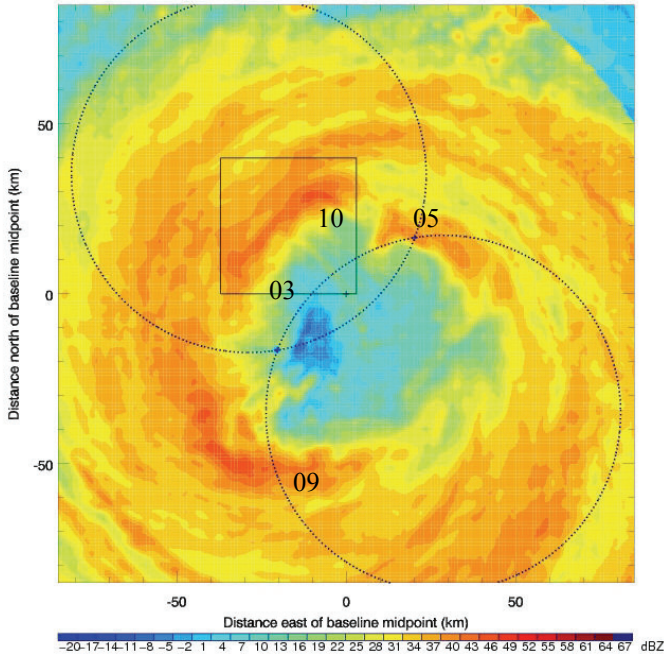

Figure 5.16: Context for 0801 UTC analysis of MV03.

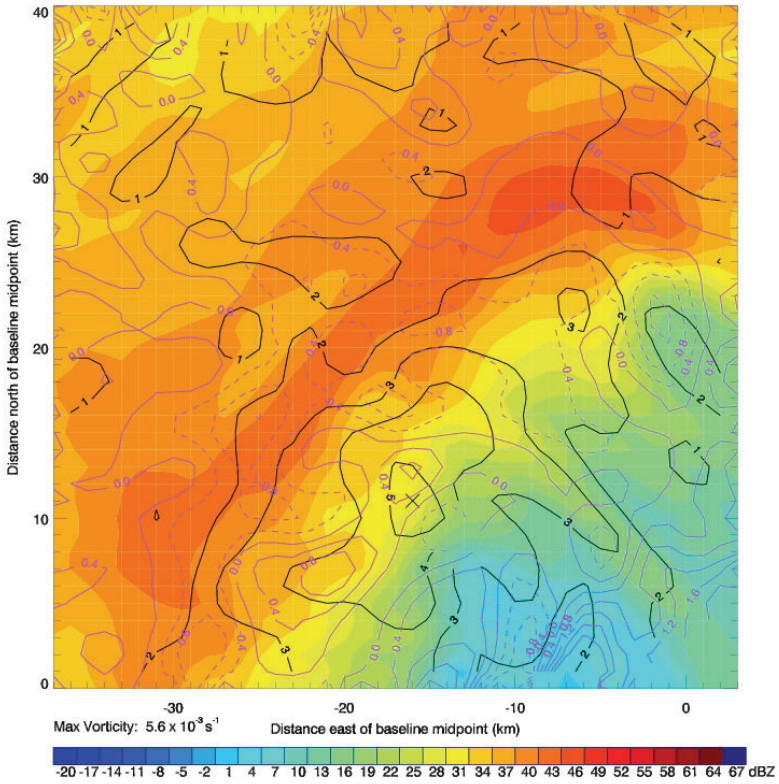

Figure 5.17: MV03 0801 UTC 1.5 km reflectivity (shaded, color bar), vorticity (black, x 10^{-3} s^{-1}) and divergence (violet, x 10^{-3} s^{-1}).

Figure 5.16 provides context for the 0801 UTC analysis. The Z arc of MV10 was connected to that associated with MV03 at this time. Vertical motions associated with each MV were less than half their previous values (within ± 3 m s^{-1}), and each was situated just ahead of the vorticity peaks. The 1.5 km vorticity and divergence fields are given in Figure 5.17. The vorticity peak of MV03 was located at the middle of the Z signature for the new, combined MV. A small closed 3 x 10^{-3} s^{-1} contour was all that remained of MV10's center. Pockets of convergence previously associated with the 2 independent features began to combine on the NE side of the vorticity maximum. An arrangement developed that mimics the organizations shown in Figures 5.13 and 5.14, with convergence along the inner side of the middle part of the Z signature and divergence at the leading portion of the segment.

5.4 MV04

The next structure of interest developed upwind of MV03 but remained for only a short time. At 0314 UTC (Figure 4.5) the leading edge of MV04 entered the far portion of the SE lobe. It progressed quickly through the lobe and left about half an hour later. Within the same amount of time, evidence of MV04 became ambiguous at best, and by 0430 UTC it was unidentifiable. While ideal results were unattainable for this entity, values reported in Table 3.1 indicate that the strengths of the vorticity center and primary updraft of MV04 were comparable to that of other MVs in Ike.

5.5 MV05

What became MV05 originated as the angled Z section in the eastern eyewall (right rear quadrant) at 0302 UTC, upwind of the developing MV04 (Figure 4.5c). While MV04 was in the SE lobe, MV05 formed a circular Z pattern as it approached the

SE lobe (Figure 4.6a,b). Like MVs 02 and 03, MV05 completed two full revolutions about the eye over the course of 6 h. It entered the SE lobe for its first foray through the dual-Doppler domain near 0330 UTC and progressed around the eye to form the SW vertex of the oblate hexagonal eyewall at 0430 UTC (Figure 4.6f). MV05 reentered the SE lobe in the northeastern eyewall just before 0600 UTC. About 20 min later it neared the baseline and skirted the edge of the lobe. A third pass through the SE lobe began near 0710 UTC (Figure 4.8d) with MV05 in the southern eyewall. It continued N across the baseline a second time into the NW lobe where the last set of analyses was carried out. After exiting the NW lobe, MV05 dissolved from view as Ike moved inland. MV05 was significant in that analysis was at least possible (even if it did not produce robust results) in nearly every part of the eyewall.

Earliest analysis times for MV05 had similar concerns as the earliest analyses of the previous MVs since MAX was embedded within a heavy rainband and the small domain was located toward the far end of the SE lobe. When MV05 reentered the lobe it was in the northeastern eyewall just prior to 0600 UTC. Results at these times were similar to those shown in Section 5.3 for MV03. The vorticity center of the feature was located at the forward side, and the maximum updraft was near it.

The final set of analyses of MV05 in the SE lobe began as it sat in the S of the eyewall at 0713 UTC. Initially, the maximum updraft was SW of the MV center, but as MV05 migrated N around the eye, the region of highest upward motion transitioned to SE of the vorticity peak. Middle stages of this transition were clear at 0728 and 0738 UTC (Figures 5.18, 5.20), while MV05 was near the center of the SE lobe. Figure 5.19 shows the 1.5 km updraft maximum directly S of MV05's vorticity center.

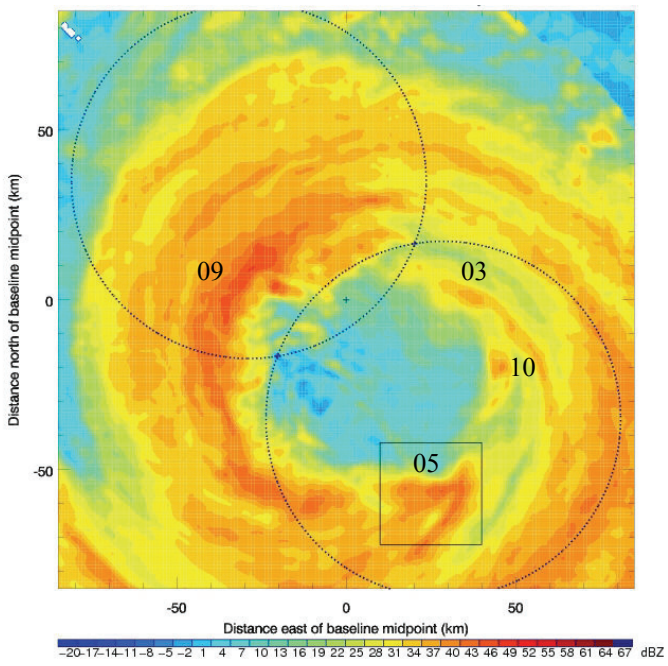

Figure 5.18: Context for 0728 UTC analysis of MV05.

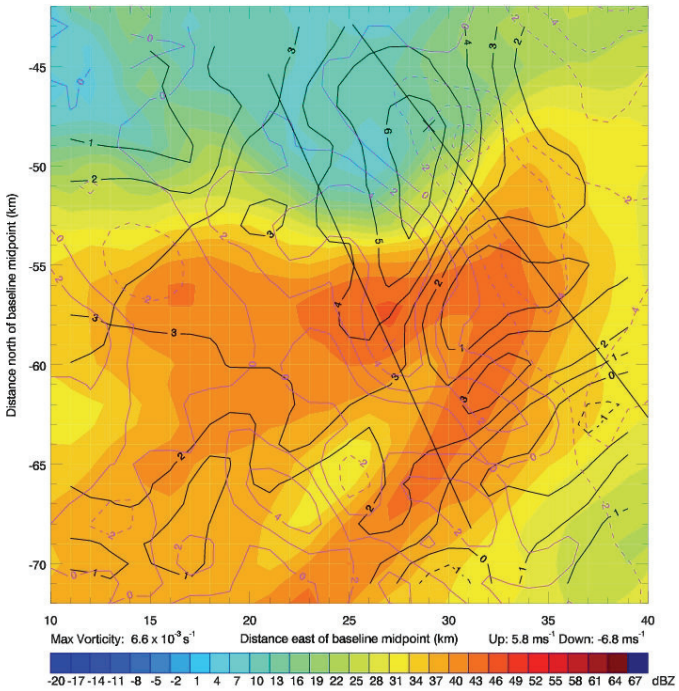

Figure 5.19: MV05 0728 UTC 1.5 km reflectivity (shaded, color bar), vorticity (black, x 10^{-3} s^{-1}) and vertical velocity (violet, m s^{-1}). Straight lines indicate vertical sections along Ike-relative radials at 143.1° and 155.9° azimuths extending 22-47 km in range from the storm center.

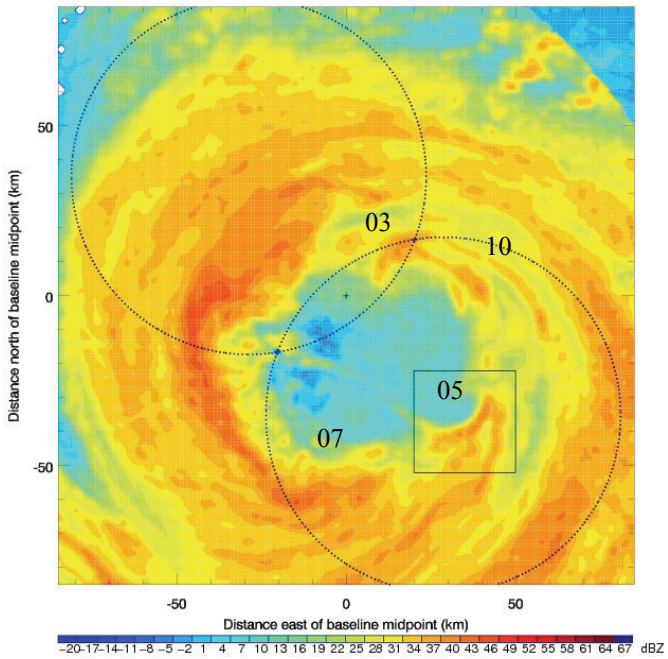

Figure 5.20: Context for 0738 UTC analysis of MV05.

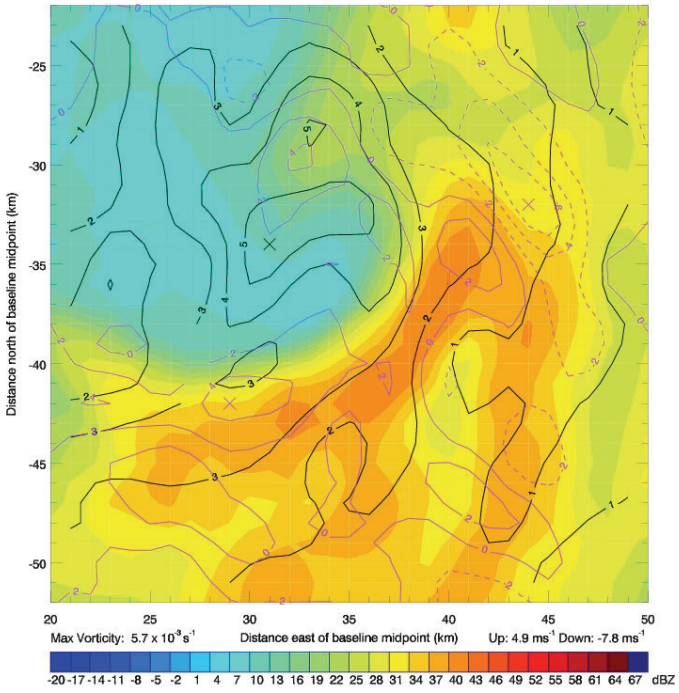

Figure 5.21: MV05 0738 UTC 1.5 km reflectivity (shaded, color bar), vorticity (black, x 10^{-3} s^{-1}) and vertical velocity (violet, m s^{-1}).

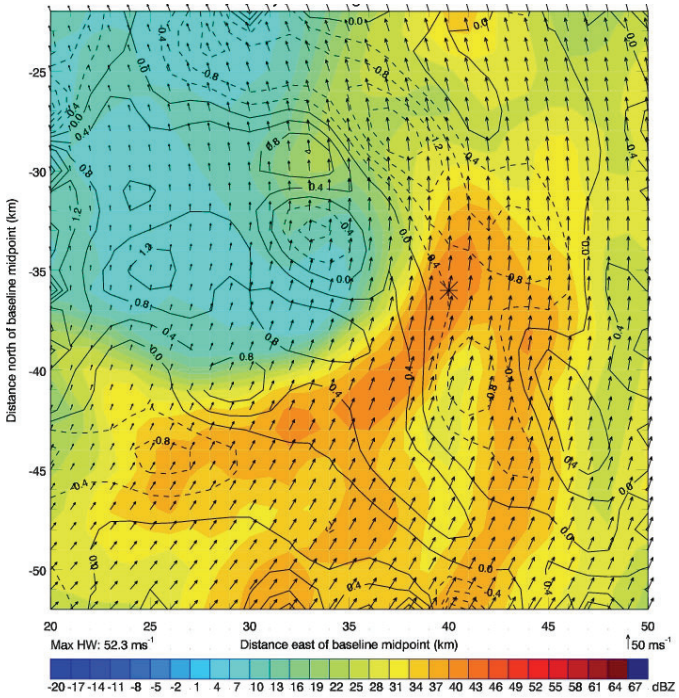

Figure 5.22: MV05 0738 UTC 1.5 km reflectivity (shaded, color bar), divergence (black, x 10^{-3} s^{-1}) and wind vectors (scaled 50 m s^{-1} vector above color bar).

This orientation remained 10 min later, as seen in Figure 5.21. Maximum horizontal wind speed for both of these times was clearly associated with the MV, as depicted in Figure 5.22 for 0738 UTC. This figure also presents the divergence field, which portrays the convergence imposed on the strong northerly component of the larger cyclonic flow by the local vorticity center at the leading edge of the MV. This result depicts the influence of the MV vorticity center on the broader TC cyclonic flow. The convergence commonly seen at the middle of these features was displaced more toward MV05's back end, upwind of the primary updraft.

Because MAX was embedded in the northern eyewall at 0738 UTC, vertical cross sections are shown from the 0728 UTC analysis. Results for this time were similar to those of 10 min later, but provide a better representation of MV05's vertical structure as the signal from MAX was less attenuated. The vertical sections start 22 km from the

center of the hurricane and extend out 25 km, as indicated in Figure 5.18. Along the 143.1° azimuth plane (1.5 km vorticity maximum), the 3 x 10^{-3} s^{-1} contour climbed up to 7 km, shown in Figure 5.23. Within that contour, the largest vorticity in the plane occurred at 0.5 km, situated underneath the 1.5 km peak. Maximum upward motion in the plane was 2.7 m s^{-1}, located at the 7.5 km height and radially outward from the highest low level reflectivity (40 km range). A layer of elevated vorticity existed directly above this, centered at the 9.5 km height. The wind field was inward at all heights, and a downward component persisted at all levels below 4 km. Figure 5.24 shows that the divergence at this time was consistent with the presence of the upward motion aloft and the downward tending flow below it. Convergence occurred through much of the area below the positive vertical motion contours; divergence prevailed above them, and was maximized over the point of peak upward velocity.

At 0728 UTC, the 155.9° azimuth intersects the 1.5 km updraft maximum. Vorticity and vertical velocity contours and wind vectors in this plane are shown in Figure 5.25. The most striking aspect of this image is the location of the highest vorticity value relative to the vertical velocity peak and direction of the total flow in the plane. Maximum vorticity was again seen downwind of the updraft maximum (as noted also in results for MV03). Largest values of these were 5.8 x 10^{-3} s^{-1} and 5.8 m s^{-1}, found at the heights 3.5 km and 1.5 km, respectively. Pockets of elevated vorticity values were present aloft at 6 km and above. The innermost of these was centered directly above the updraft at 37 km range, and a second was focused at 43 km range. Figure 5.26 shows the divergence field in this plane. Beneath the upward velocity maximum, divergence values

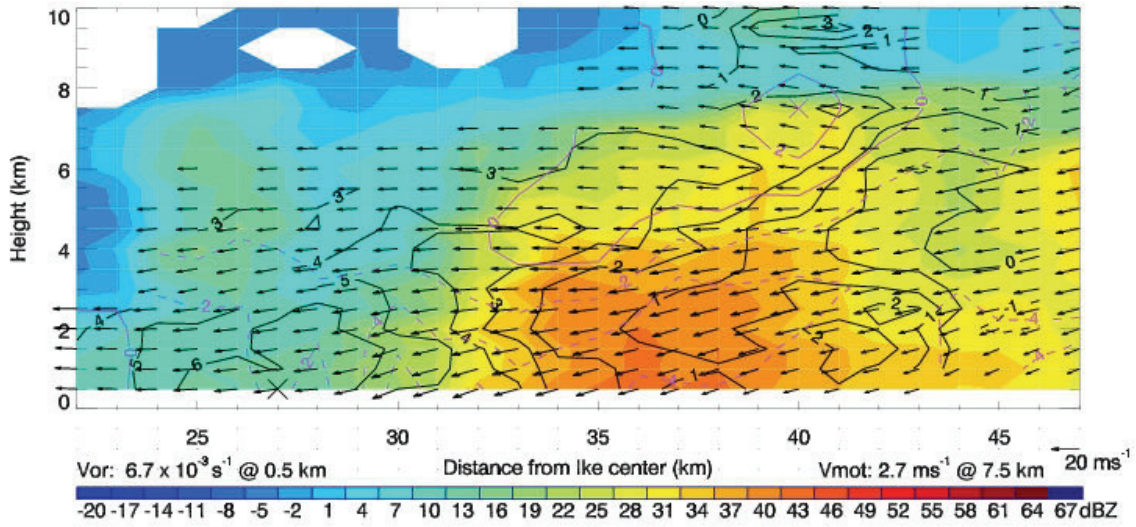

Figure 5.23: MV05 0728 UTC Ike-relative 143.1° azimuth reflectivity (shaded, color bar), vorticity (black, x 10^{-3} s^{-1}), vertical velocity (violet, m s^{-1}) and wind vectors (scaled 20 m s^{-1} vector above color bar).

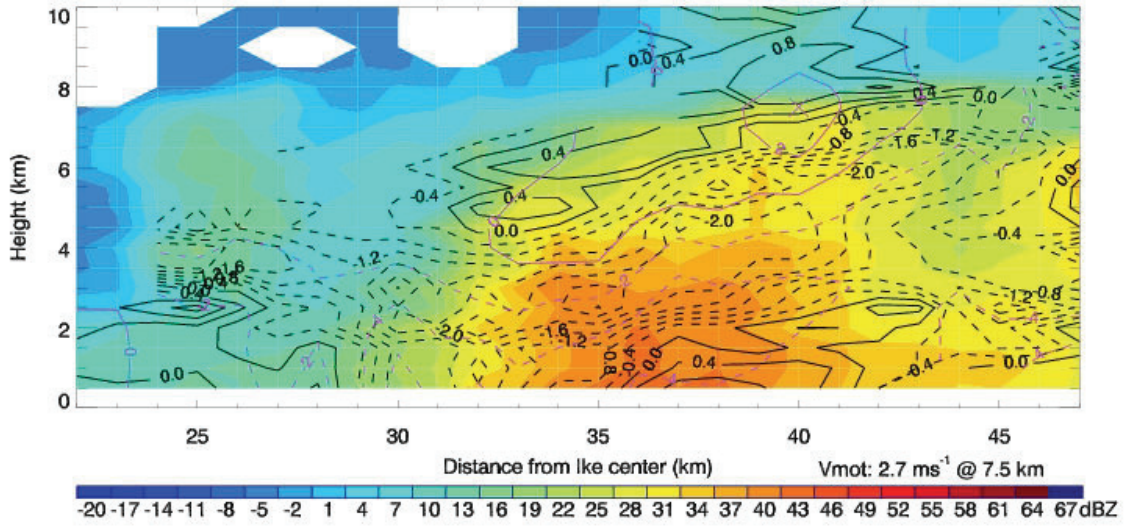

Figure 5.24: MV05 0728 UTC Ike-relative 143.1° azimuth reflectivity (shaded, color bar), divergence (black, x 10^{-3} s^{-1}) and vertical motion (violet, m s^{-1}).

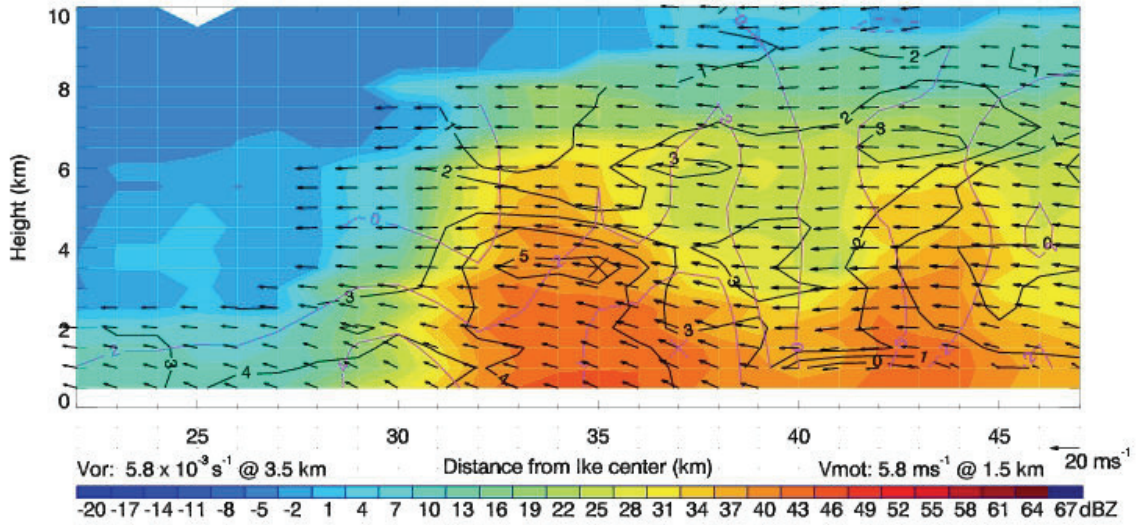

Figure 5.25: MV05 0728 UTC Ike-relative 155.9° azimuth reflectivity (shaded, color bar), vorticity (black, x 10^{-3} s^{-1}), vertical velocity (violet, m s^{-1}) and wind vectors (scaled 20 m s^{-1} vector above color bar).

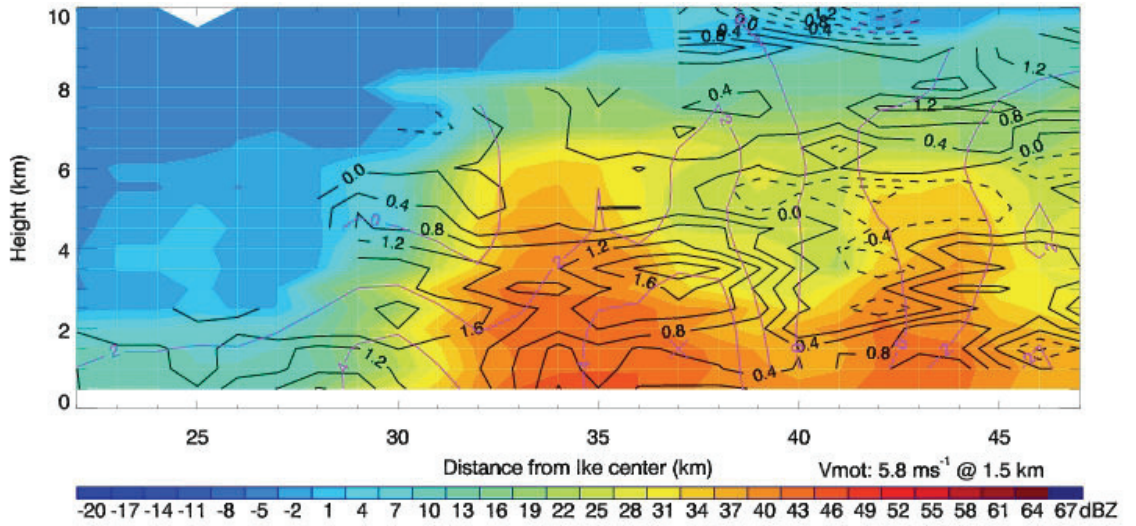

Figure 5.26: MV05 0728 UTC Ike-relative 155.9° azimuth reflectivity (shaded, color bar), divergence (black, x 10^{-3} s^{-1}) and vertical motion (violet, m s^{-1}).

fell to zero at 0.5 km. Under this height, convergence presumably occurred but was unresolved in this analysis. Above the peak vertical velocity, divergence values increased and a closed 2 x 10^{-3} s^{-1} occurred directly over the 4 m s^{-1} contour at the 3.5 km height.

At about 0800 UTC, MV05 crossed the baseline and emerged in the NW lobe in the northern eyewall. The first analysis was degraded due to the blocking of the MAX truck cab, but subsequent analyses portrayed the continued transition of the updraft location. When MV05 was in the northern eyewall, the primary updraft was located E of the vorticity center, having progressed cyclonically from its previous position at 0738 UTC. The configuration was reminiscent of that seen for MV02 at 0458 UTC (Figure 5.2). Next, MV05 progressed to the northwestern and then western eyewall. As it was situated in these locations, the maximum upward velocities moved to the W of the vorticity center. This transition was evident at 0819 and 0829 UTC, when MV05 was near the center of the NW lobe as shown in Figures 5.27 and 5.28.

Plots of the vorticity and vertical velocity at both times are given in Figures 5.29 and 5.30. In the 0819 UTC analysis, the peak updraft occurred behind the vorticity center, similar to that analyzed for MV02. This was entirely different at 0838 UTC, when the maximum vertical velocity was located W of the vorticity peak. As with earlier MVs, Figure 5.31 shows that the 0819 UTC radial wind component changed direction across the feature, and the shift was nearly coincident with the location of the vorticity center. The 0829 UTC divergence field in Figure 5.32 depicts converging flow near the middle of the feature, just upwind of the updraft, and diverging flow at the front of the

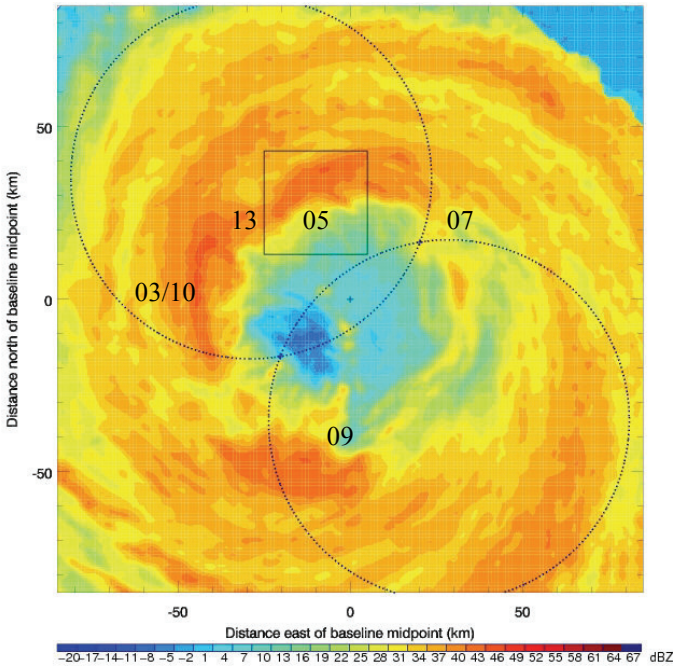

Figure 5.27: Context for 0819 UTC analysis of MV05.

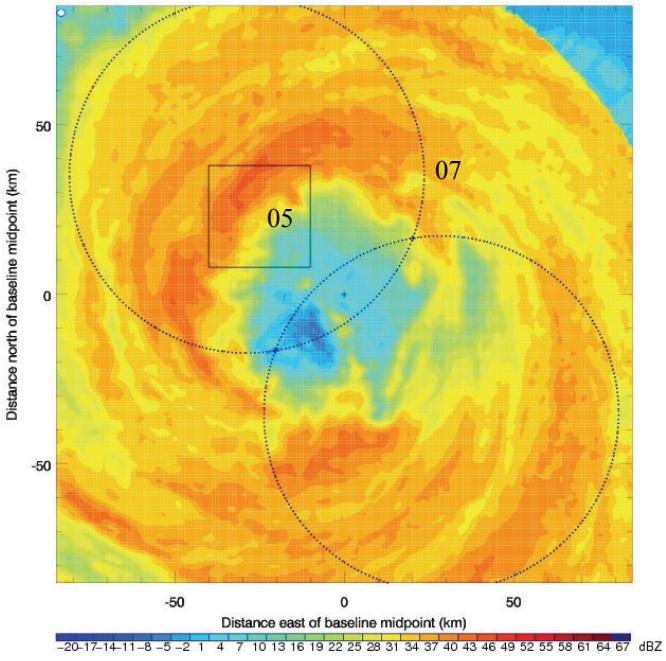

Figure 5.28: Context for 0829 UTC analysis of MV05.

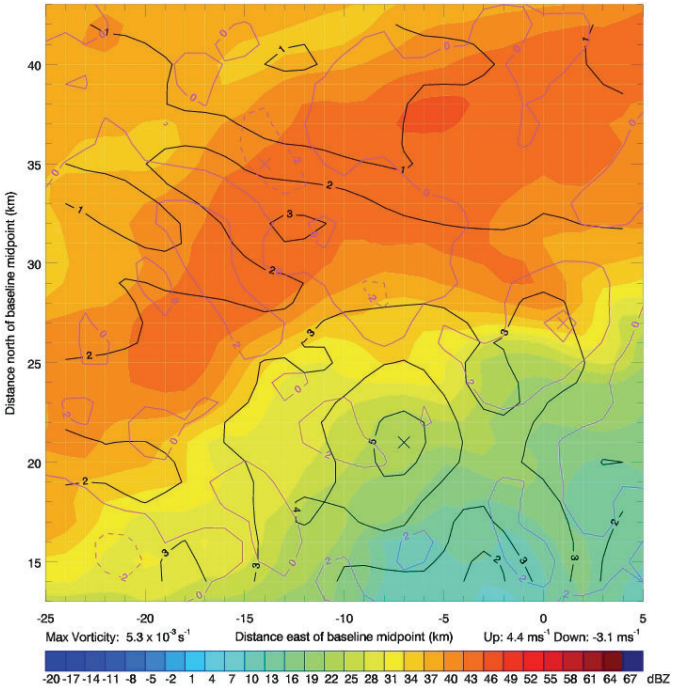

Figure 5.29: MV05 0819 UTC 1.5 km reflectivity (shaded, color bar), vorticity (black, x 10^{-3} s^{-1}) and vertical velocity (violet, m s^{-1}).

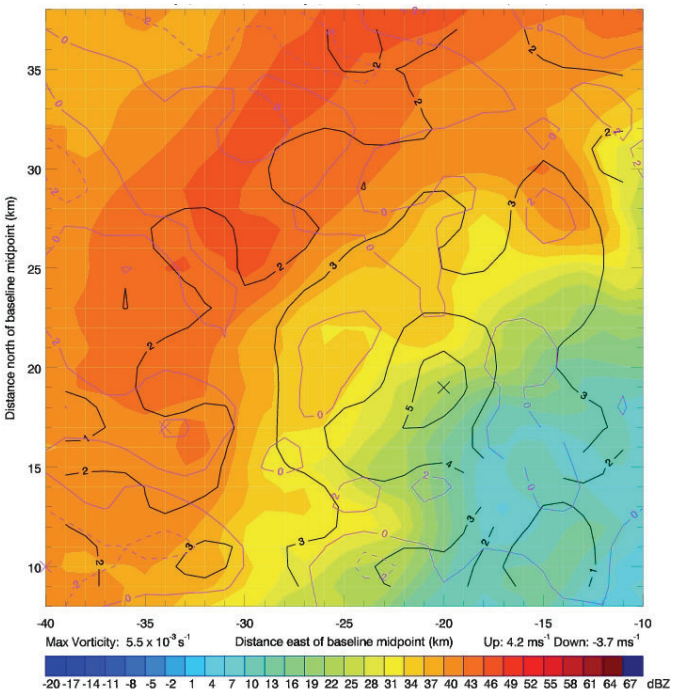

Figure 5.30: MV05 0829 UTC 1.5 km reflectivity(shaded, color bar), vorticity (black, x 10^{-3} s^{-1}) and vertical velocity (violet, m s^{-1}).

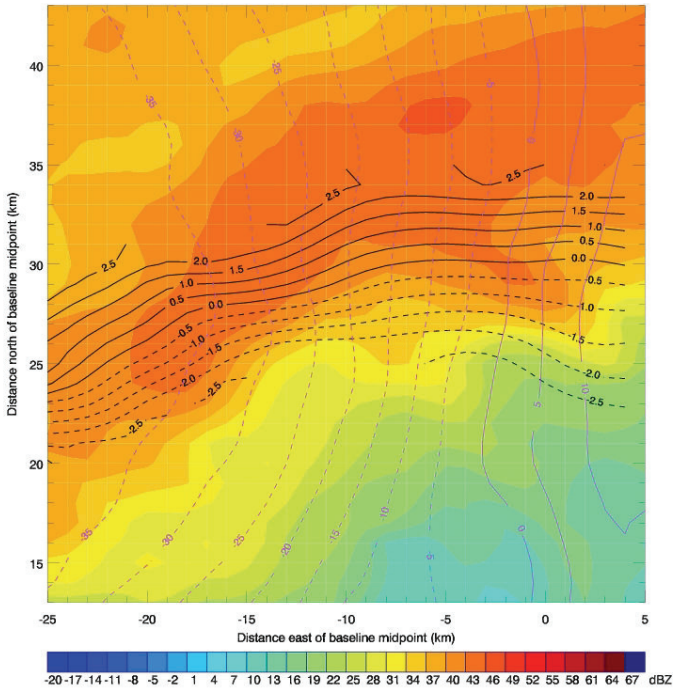

Figure 5.31: MV05 0819 UTC 1.5 km reflectivity (shaded, color bar), pressure perturbation (black, hPa) and radial wind (violet, m s^{-1}).

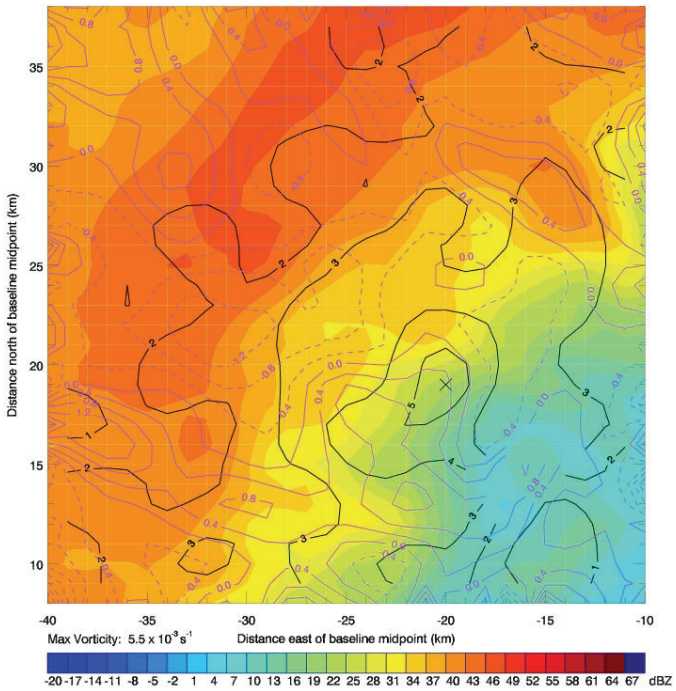

Figure 5.32: MV05 0829 UTC 1.5 km reflectivity (shaded, color bar), vorticity (black, x 10^{-3} s^{-1}) and divergence (violet, x 10^{-3} s^{-1}).

Z signature. This configuration was consistent the location of peak vorticity, and compared well to behavior of other MVs, such as was shown for MV03 in Figure 5.14.

After 0830 UTC, the last three analyses were completed with MV05 in the western and southwestern eyewall. At these times the updraft moved to the forward facing side of the MV. Vertical velocity also increased, but the 21.7 m s^{-1} value indicated on the last line for MV05 in Table 3.1 needs to be conservatively viewed as the 0900 UTC analysis domain skirted the outer edge of the lobe near the baseline.

5.6 Probable MV06

Contrary to the long-lived MV05, the location and timing of MV06 allowed for only a few dual-Doppler runs. It was first evident a the leading section of the inward spiraling eyewall at 0117 UTC (Figure 4.3h). In time MV06 constituted the southernmost vertex of the triangle shape at 0246 UTC, and when the eyewall was convoluted by 0314 UTC MV06 was located at the SE corner. MV06 made only one pass through the SE lobe, then progressed around the eyewall for at least another hr before it became ambiguous ahead of MV07 at about 0500 UTC. Limited results from the few available times contained similar characteristics to other northern eyewall MVs.

5.7 MV07

The next feature of interest was first evident in Z as the arc at the SE corner of the eyewall (right rear quadrant) at 0348 UTC (Figure 4.6c). MV07 formed from the front most portion of this arc in progression behind MV06 and entered the SE lobe at about 0415 UTC (Figure 4.6e). MV07 passed through the SE lobe three times and the NW lobe once as it completed about 2.5 loops around the eye within 6 h. In the first few analysis times, it was in the northern eyewall. During its second pass in the SE lobe, MV07

moved from the eastern to northeastern eyewall starting near 0600 UTC. After this it hugged the lobe boundary and emerged back into the lobe at 0728 UTC in the southwestern eyewall. It crossed the baseline and entered the NW lobe near 0830 UTC in the NE eyewall (Figure 4.9c). While in the nothern eyewall, MV07 began to lose its distinction. During MV07's existence, two smaller entities developed just ahead and behind it. These features (11 and 14) are discussed later in this chapter.

The first analyses of MV07 in the SE lobe revealed a distinct vorticity peak associated with the curled Z segment, the clear signature of an MV. Optimal location (and thus most accurate retrievals) of MV07 during this interval occurred at 0424 UTC, when it occupied the northern eyewall as shown in Figure 5.33. It is important to note that at this time both radars were affected by rain attenuation, obvious in the degrading of Z beyond about 20 km E of the baseline midpoint. Despite this limitation, though, results for this time were still good. Figures 5.34 and 5.35 present results at 1.5 km.

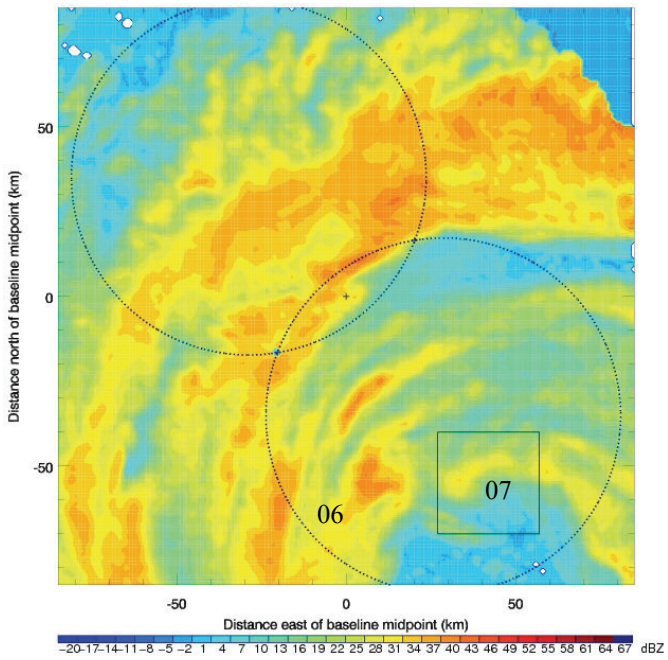

Figure 5.33: Context for 0424 UTC analysis of MV07.

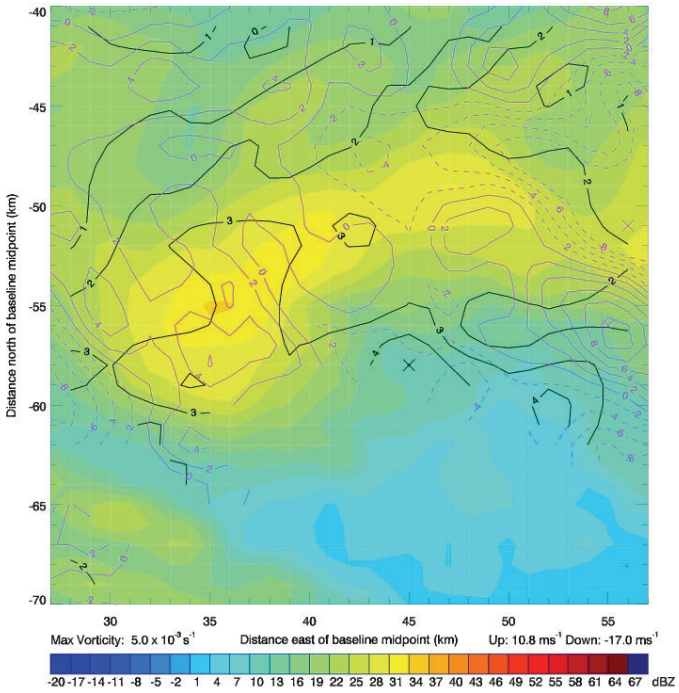

Figure 5.34: MV07 0424 UTC 1.5 km reflectivity (shaded, color bar), vorticity (black, x 10^{-3} s^{-1}) and vertical velocity (violet, m s^{-1}).

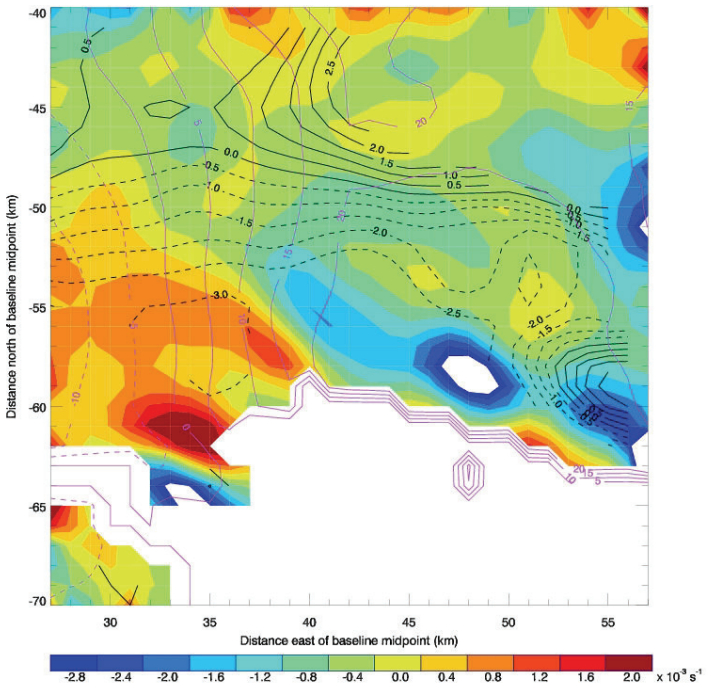

Figure 5.35: MV07 0424 UTC 1.5 km divergence (shaded, color bar), pressure perturbation (black, hPa) and radial wind component (violet, m s^{-1}).

The 5 x 10^{-3} s^{-1} vorticity peak was at the center of the Z arc, and the most prominent updraft was located to the E, an arrangement that has become very familiar for northern eyewall MVs. Contours of the radial wind in Figure 5.35 indicate outward (inward) flow at the trailing (leading) sides of MV07, showing the impact of the mesovortex on the TC's larger scale circulation in a way consistent with other MVs. Pressure perturbation contours were again generally perpendicular to the radial wind component and suggested a localized minimum of at least -3.0 hPa in the region of enhanced divergence at the leading portion of the feature. This result draws to mind the work of KS01 and B06 that used numerical models to demonstrate that MVs could contain isolated pressure minima. Their findings agreed well to the localized pressure minima observed in the MVs of Andrew (Willoughby and Black 1996) and Hugo (Marks et al. 2008). To the E, convergence in the region of inflow into MV07's center was similar to configurations of previous features.

By about 0600 UTC, MV07 was much larger than the previously discussed MVs, with a diameter of about 30 km across the Z arc (Figure 4.7g). As it moved from the E to northwestern eyewall, the preferred location of the updraft transitioned from the eastern, rear side of the MV to the more western, forward side, following similar organizational behavior as noted above for MVs 03 and 05. Upwind of MV07 during this pass through the SE lobe, non-MV11 developed in the Z field at 0610 UTC (Figure 4.7h).

Over the next hour, MV07 continued around the eye but passed over the baseline and rotated just along the outside edge of the SE lobe. When it finally reentered the dual-

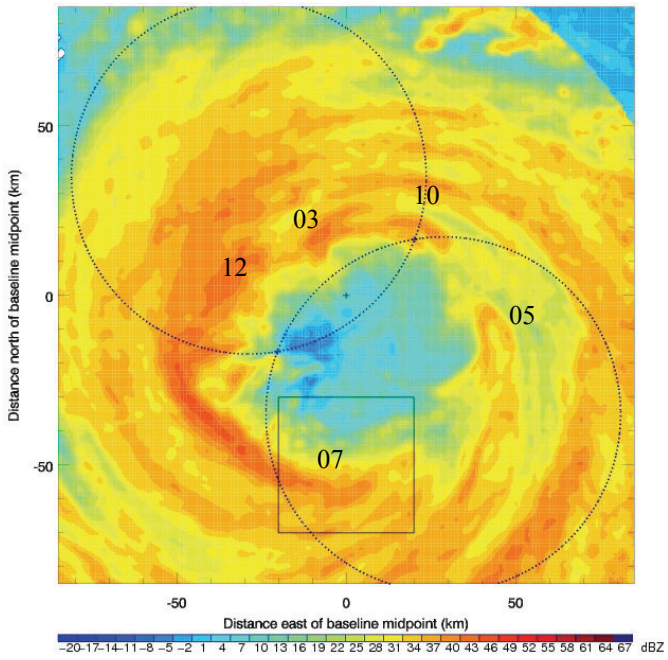

Figure 5.36: Context for 0747 UTC analysis of MV07.

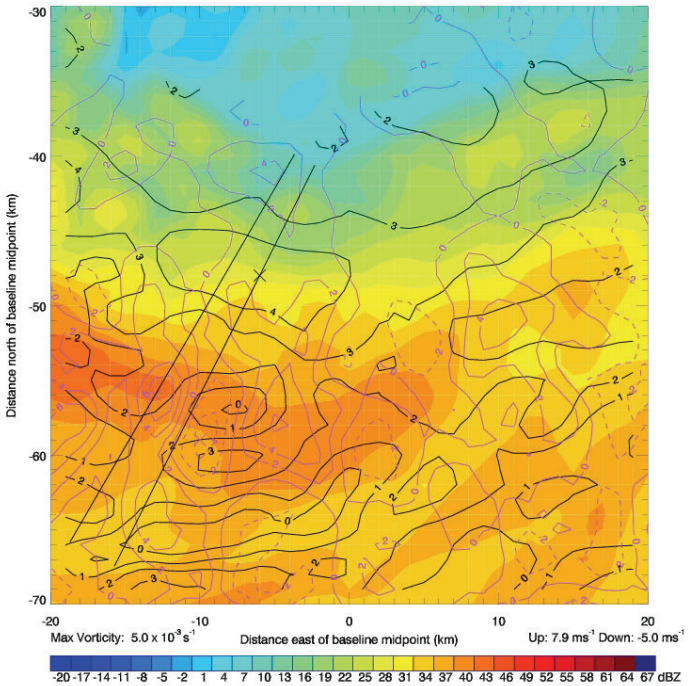

Figure 5.37: MV07 0747 UTC 1.5 km reflectivity (shaded, color bar), vorticity (black, x 10^{-3} s^{-1}) and vertical velocity (violet, m s^{-1}). Straight lines indicate vertical sections along Ike-relative radials at 206.6° and 210.1° azimuths extending 25-55 km in range from the storm center.

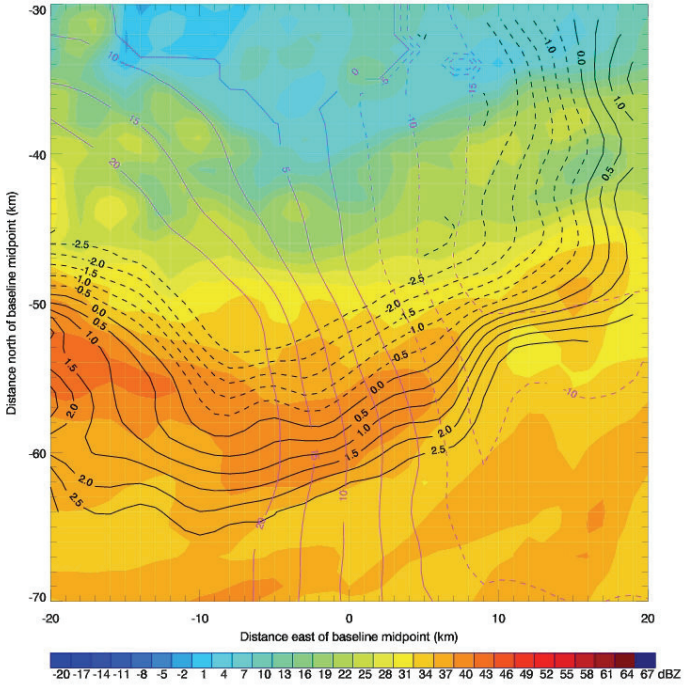

Figure 5.38: MV07 0747 UTC 1.5 km reflectivity (shaded, color bar), pressure perturbation (black, hPa) and radial wind component (violet, m s^{-1}).

Doppler domain, it formed the SW vertex of the oblate hexagonal eyewall. Context for the smaller analysis domain at 0747 UTC is given in Figure 5.36. At the previous analysis time, an elongated 4 x 10^{-3} s^{-1} contour enclosed the vorticity peak. The strip of elevated vorticity was less prominent but still clear in the 0747 UTC analysis, shown in Figure 5.37. The Z field had a distinct arc shape, and an updraft/downdraft pair sat SW of the vorticity peak. This pair contained the maximum updraft. Figure 5.38 shows contours of the radial wind component for this time, which indicated inward flow at the front of the MV and outward flow to the back. The isopleths were again approximately perpendicular to the pressure perturbation lines. The Z, vorticity, and vertical velocity signatures associated with MV07 decreased as it moved into the E eyewall, and the updraft location transitioned to SE of the vorticity peak.

Radius-height sections at 0747 UTC intersect the vorticity and updraft maxima at azimuths of 206.6° and 210.1°, respectively (refer to Figure 5.37). These start at a range of 25 km from the storm center and extend 30 km. Figure 5.39 shows the 206.6° plane, where largest vorticity was found directly beneath the 1.5 km peak at the 0.5 km height. Vorticity values in the plane beyond 43 km range rarely exceeded 2 x 10^{-3} s^{-1}. The highest upward velocity was 4.9 m s^{-1} and occurred at the 2 km height radially out from the Z signature. Downward motion was evident at 41-46 km range (the pair to the updraft maximum at 1.5 km). As can be seen in Figure 5.40, divergence occurred beneath this area, not surprisingly in the region where the low level Z increased and began to spread outward. The wind field in this plane was almost entirely radially outward, save for the vertical components imposed by the updraft and downdraft, consistent with Figure 5.38.

The 210.1° azimuth plane at 0747 UTC contains the peak updraft associated with 07 (Figure 5.37). Maximum vorticity in this plane occurred at the same range as height

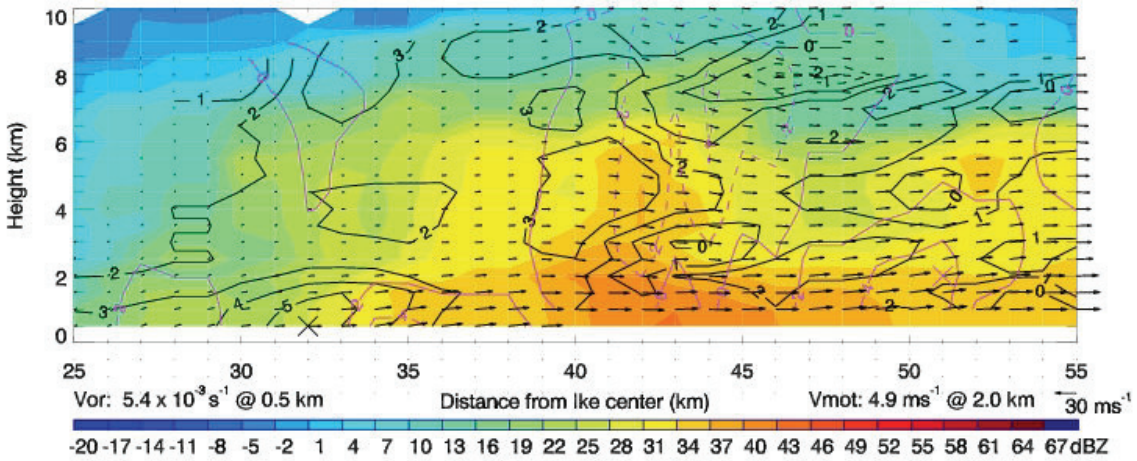

Figure 5.39: MV07 0747 UTC Ike-relative 206.6° azimuth reflectivity (shaded, color bar), vorticity (black, x 10^{-3} s^{-1}), vertical velocity (violet, m s^{-1}) and wind vectors (scaled 30 m s^{-1} vector above color bar).

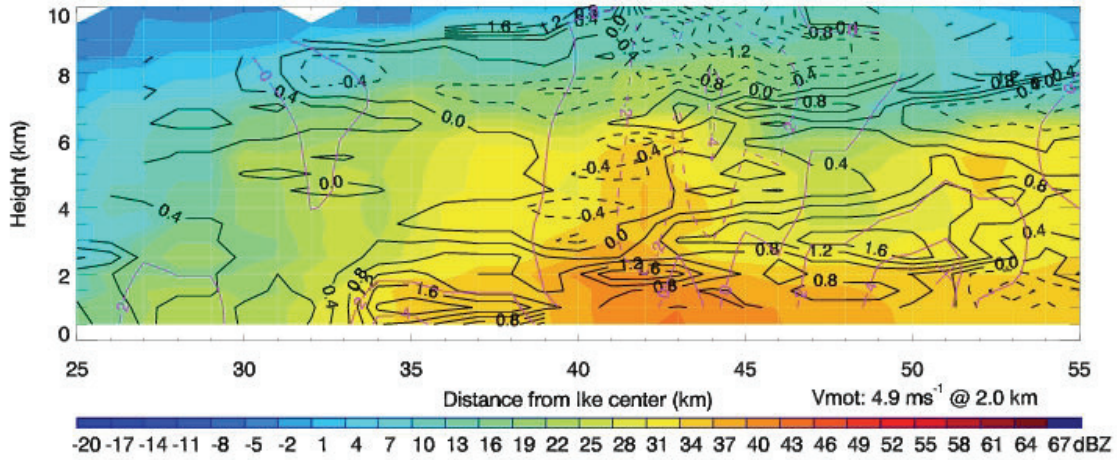

Figure 5.40: MV07 0747 UTC Ike-relative 206.6° azimuth reflectivity (shaded, color bar), divergence (black, x 10^{-3} s^{-1}) and vertical motion (violet, m s^{-1}).

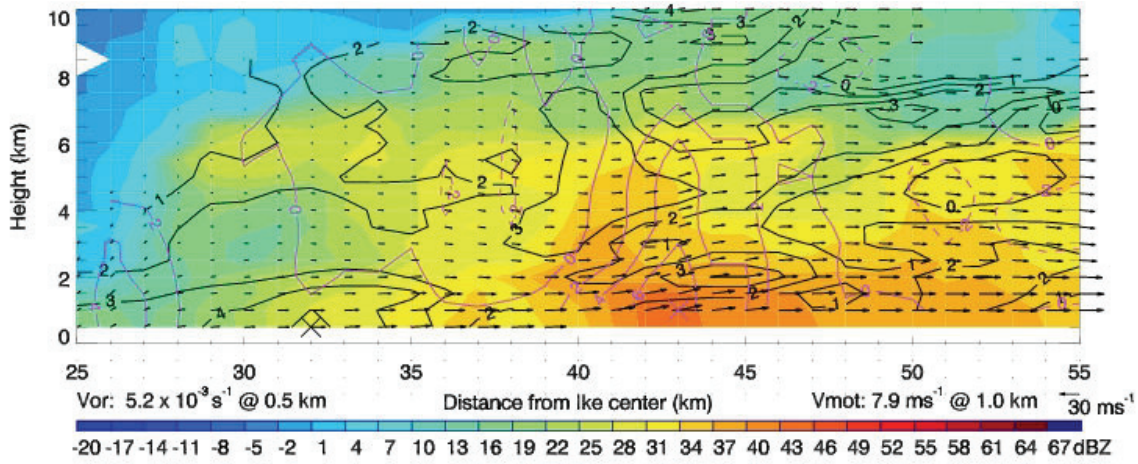

Figure 5.41: MV07 0747 UTC Ike-relative 210.1° azimuth reflectivity (shaded, color bar), vorticity (black, x 10^{-3} s^{-1}), vertical velocity (violet, m s^{-1}) and wind vectors (scaled 30 m s^{-1} vector above color bar).

as in the 206.6° section. The peak vertical motion was 7.9 m s^{-1}, situated at 43 km range and 1 km height, shown in Figure 5.41. As with other MVs in Ike, a pocket of enhanced vorticity occurred downwind of the updraft, seen as the closed 4 x 10^{-3} s^{-1} contour centered at about 44.5 km range and 2 km height.

After 0747 UTC, MV07's 1.5 km vorticity decreased and never reached 5 x10^{-3} s^{-1} again (refer to Table 3.1). At 0755 UTC (context given in Figure 5.42) MV07's vorticity center elongated and the peak values of it and the maximum updraft began to decrease, seen in Figure 5.43. The radius-height sections indicated range from 22-52 km from Ike's center. Vorticity and vertical motion in the plane along 177.2° were unremarkable in light of the cross sections through MV07 at previous times. Maximum values of both were found at the 0.5 km level and there was little structure in either field above the lowest levels. The wind field was directed inward at all heights, demonstrating the characteristic front edge inflow. The plane along 190.3° passes through the 1.5 maximum updraft. Vorticity, vertical velocity and vectors of the field are given in Figure 5.44. The updraft peaked at 6 m s^{-1} at 42 km range and 1 km height. Below 2 km, winds were directed outward from 30 km range to the end of the section. Elsewhere, the radial component was inward. Maximum vorticity in the plane occurred at 33 km range at the lowest height in the domain, and there was a slight elevation in the vorticity values above the peak updraft velocity, consistent with earlier results. Aloft, there was a vorticity *minimum*, as indicated by the closed -1 x 10^{-3} s^{-1} contour centered at 42 km range and 8 km height. The upper levels of hurricanes are characterized by outflow in an anti-cyclonic direction, and this result may be an artifact of that circulation. Largest divergence values occurred at 43 km range and 3 km height, just above the updraft

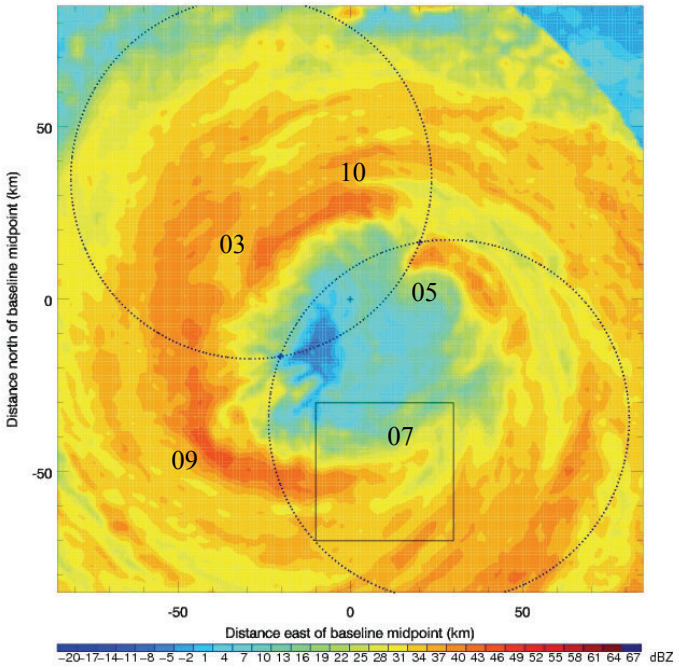

Figure 5.42: Context for 0755 UTC analysis of MV07.

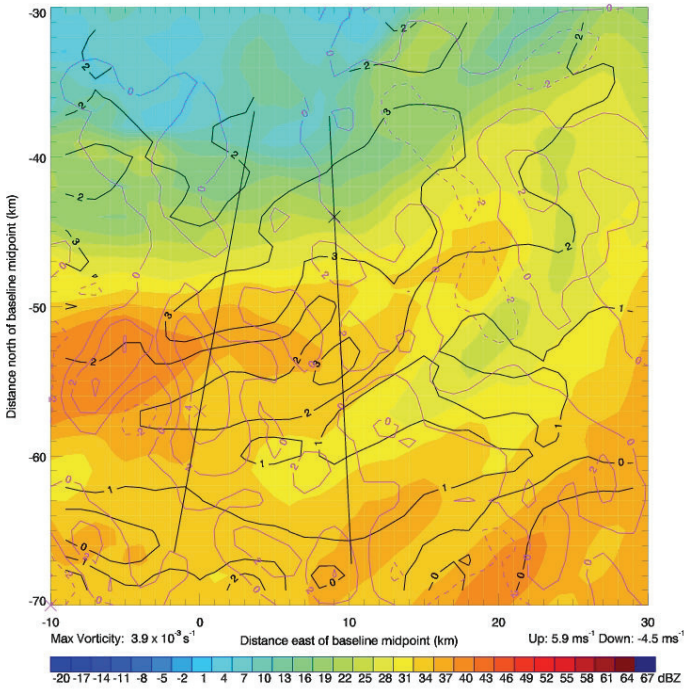

Figure 5.43: MV07 0755 UTC 1.5 km reflectivity (shaded, color bar), vorticity (black, x 10^{-3} s^{-1}) and vertical velocity (violet, m s^{-1}). Straight lines indicate vertical sections along Ike-relative radials at 177.2° and 190.3° azimuths extending 22-52 km in range from the storm center.

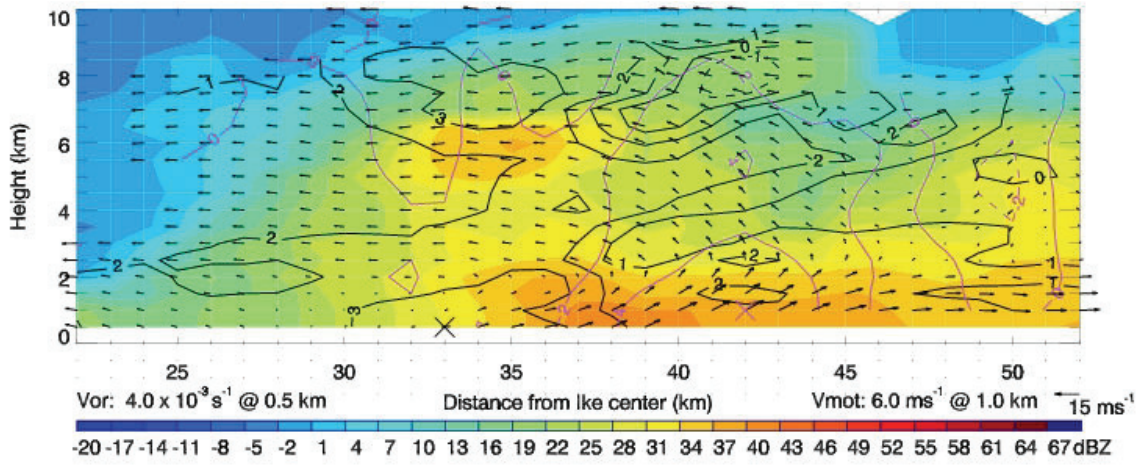

Figure 5.44: MV07 0755 UTC Ike-relative 190.3° azimuth reflectivity (shaded, color bar), vorticity (black, x 10^{-3} s^{-1}), vertical velocity (violet, m s^{-1}) and wind vectors (scaled 15 m s^{-1} vector above color bar).

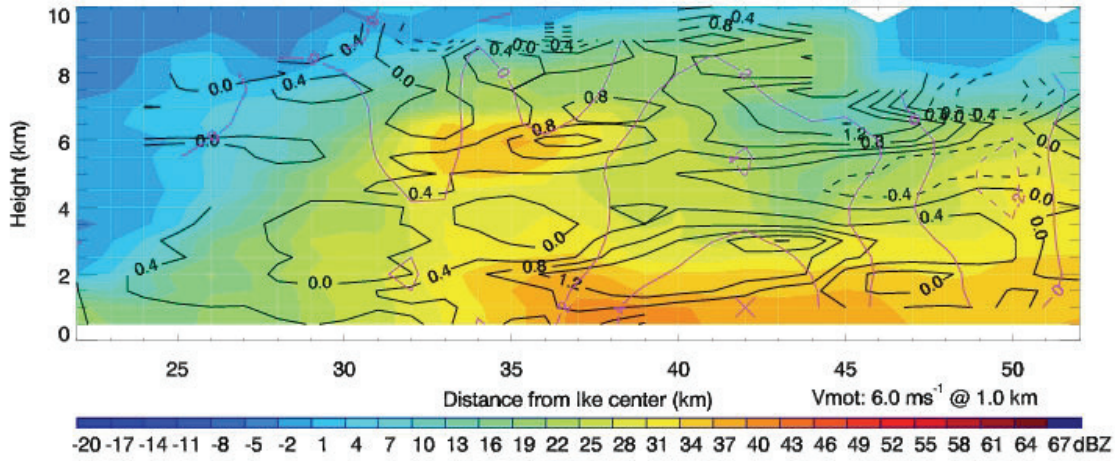

Figure 5.45: MV07 0755 UTC 190.3° azimuth reflectivity (shaded, color bar), divergence (black, x 10^{-3} s^{-1}) and vertical motion (violet, m s^{-1}).

maximum and near the vertical level at which the wind field transitioned to radially inward flow, as shown in Figure 5.45.

After MV07 crossed the baseline, analyses were done in the NW lobe. At these analysis times (0848-0910 UTC), MV07's Z signature became disheveled and its vorticity center was absorbed into the eyewall behind the stronger, developing MV14. The 0910 UTC analysis depicted this well, and is shown in Figures 5.46 and 5.47. What remains of MV07's center was located at the point 34 km W and 55 km N of the baseline midpoint. Peak vorticity in the domain was actually related to 14, and trumped the value of MV07's dissolving core (note that values in Table 3.1 related to 14 in these analyses agree well with those found in the runs where the small domain is focused only on 14).

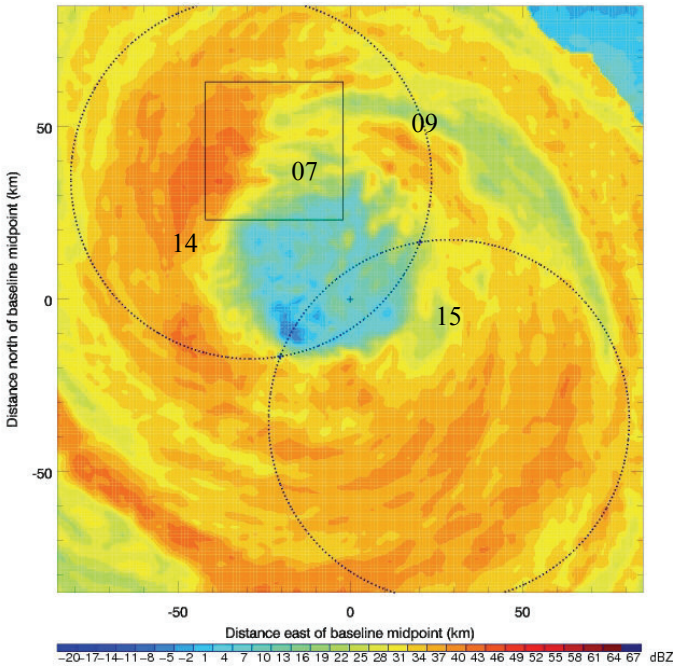

Figure 5.46: Context for 0910 UTC analysis of MV07.

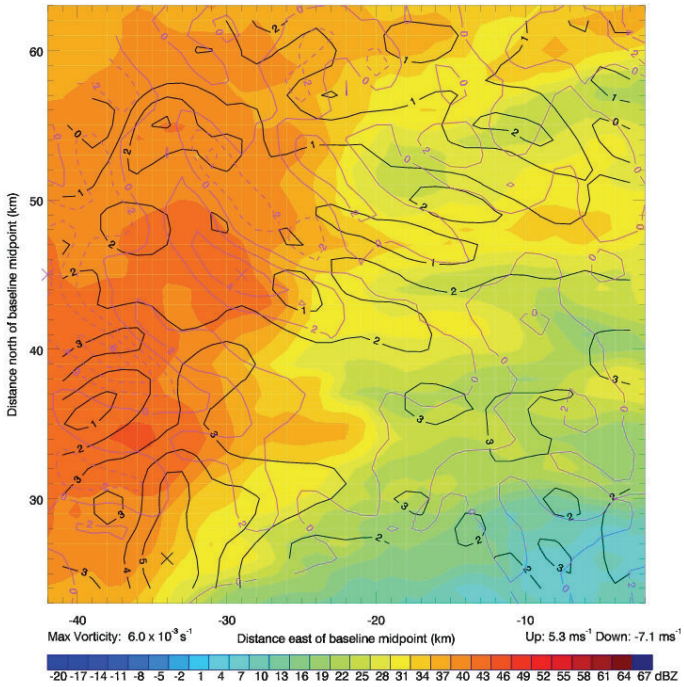

Figure 5.47: MV07 0910 UTC 1.5 km reflectivity (shaded, color bar), vorticity (black, x 10^{-3} s^{-1}) and vertical velocity (violet, m s^{-1}).

5.8 MV08

Another very short-lived entity, MV08 appeared in the northern eyewall between MVs 07 and 02 just after 0430 UTC (Figure 4.6g). Analyses indicated it contained its own local vorticity peak, first in a "bull's eye" pattern as in MVs 02 and 03 in the northern eyewall at 0458 and 0535 UTC (Figures 5.2 and 5.13), respectively, then as an elongated strip as shown in MV07 at 0755 UTC (Figure 5.43). Perhaps because of the development of MV07 ahead and the more vigorous MV02 behind it, MV08 quickly disappeared from view. Beyond 0440 UTC, it was indistinguishable.

5.9 MV09

Like MV05, MV09 had a long life and existed in nearly every part of the eyewall within the dual-Doppler region. It was first evident in the southeastern eyewall (right

rear quadrant) as the arced Z segment between MVs 02 and 03 at 0430 UTC (Figure 4.6f). During its first progression in the SE lobe, MV09 moved from the northeastern to northwestern eyewall. It reentered the lobe in the SE eyewall at about 0630 UTC, traveled N around the eye, and crossed the baseline at about 0715 UTC (Figure 4.8e). From there, it entered the NW lobe for a brief time before making a last pass through the SE lobe from 0800-0848 UTC. Next, MV09 again entered the NW lobe for the final analysis times. In total, MV09 completed more than two revolutions about the eye over the course of 5 h.

Horizontal and vertical organization of MV09 from 0458-0535 UTC were similar to that shown for earlier northern eyewall MVs (see Sections 5.2, 5.3 and 5.5). The vorticity center was located at the front of the Z signature, and the maximum updraft transitioned from the trailing side to leading edge of MV09 as it moved from NE to NW of Ike's center. In the vertical, MV09 contained elevated vorticity maxima, arranged downwind of updrafts, as was shown for earlier MVs. Vorticity and vertical velocity maxima during MV09's second pass in the lobe (0630-0704 UTC) demonstrated the same preferred locations as in MV05 while it also moved through the eastern eyewall (Section 5.5). With MV09 in the southeastern and eastern eyewall the maximum updraft favored the outer portion of the entity (SE of the vorticity peak). As MV09 moved to the northeastern then western eyewall in the NW lobe, this location translated toward to the front of the feature.

While MV09 moved from the southern to eastern eyewall in its last pass through the SE lobe (0801-0848 UTC), the horizontal structure of the vorticity peak elongated along its inner edge. Figure 5.48 shows the context for the 0838 UTC analysis. Prior to

0800 UTC, MV09's vorticity center was generally patterned in a "bull's eye" set up. Once it entered the SE lobe, analyses showed an elongated pattern, as seen in Figure 5.49 for the good geometry at 0838 UTC. The corresponding divergence field (Figure 5.50) showed convergence into the MV center, but MV09's effect on the radial wind component was less obvious. More inward motion was found at the front of MV09, but there was no shift to outward flow on its backside. Pressure perturbation contours bent inward at its middle, contrary to the smoother isopleths shown earlier for stronger MVs.

Radius-height sections through 09 at 0838 UTC go along 20-50 km range from Ike's center and are located along the lines shown in Figure 5.49. Wind vectors and contours of vorticity and vertical velocity in each plane are given in Figures 5.51 and 5.52. Flow along both azimuths was predominantly inward, and the vertical motion field was generally less vigorous than in vertical sections though MVs at earlier times. In the 143.6° plane the highest vorticity occurred at the lowest height in the domain and 34 km

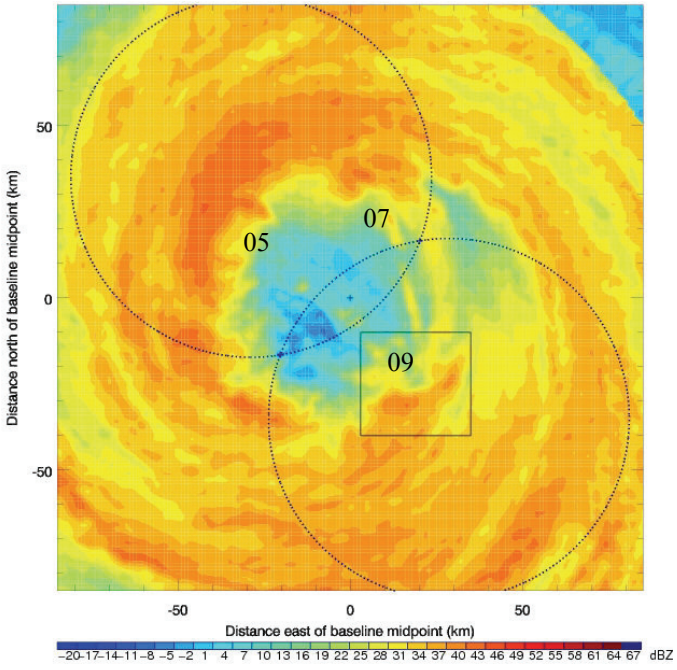

Figure 5.48: Context for 0838 UTC analysis of MV09.

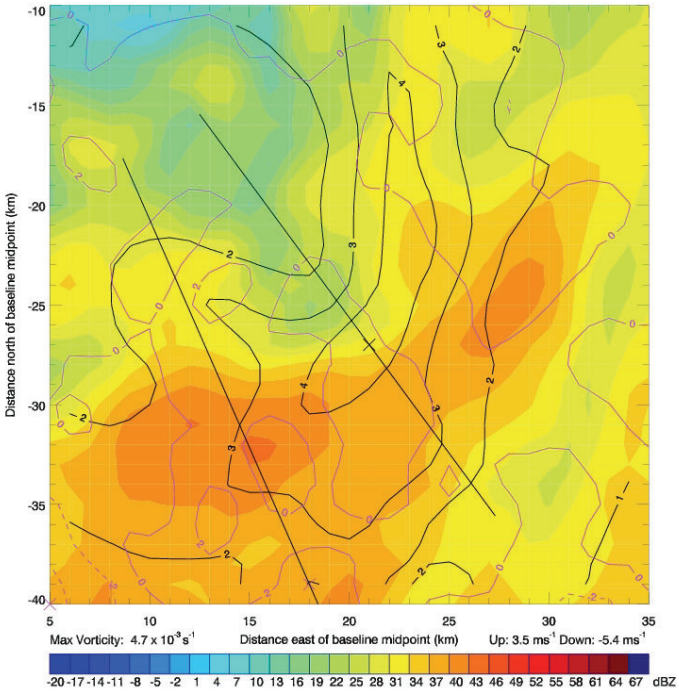

Figure 5.49: MV09 0838 UTC 1.5 km reflectivity (shaded, color bar), vorticity (black, x 10^{-3} s^{-1}) and vertical velocity (violet, m s^{-1}). Straight lines indicate vertical sections along Ike-relative radials at 143.6° and 156.4° azimuths extending 20-45 km in range from the storm center.

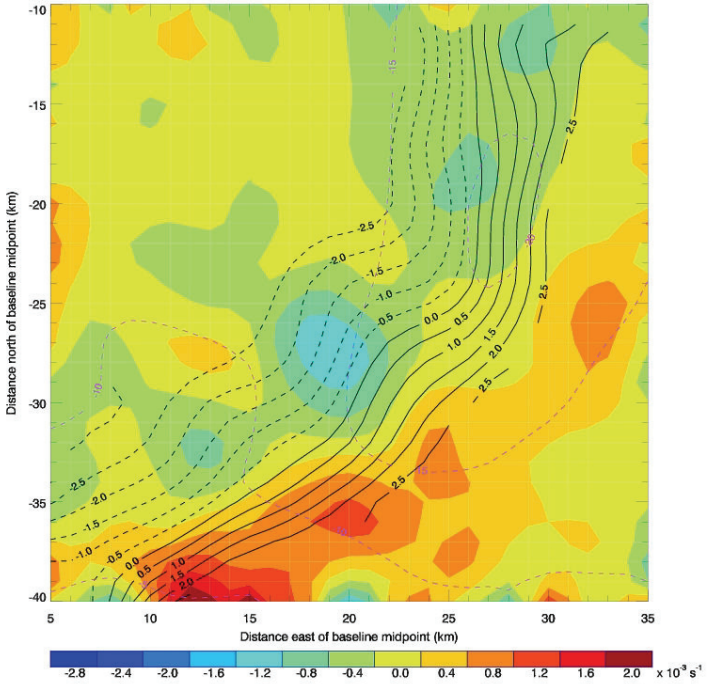

Figure 5.50: MV09 0838 UTC 1.5 km divergence (shaded, color bar), pressure perturbation (black, hPa) and radial wind component (violet, m s^{-1}).

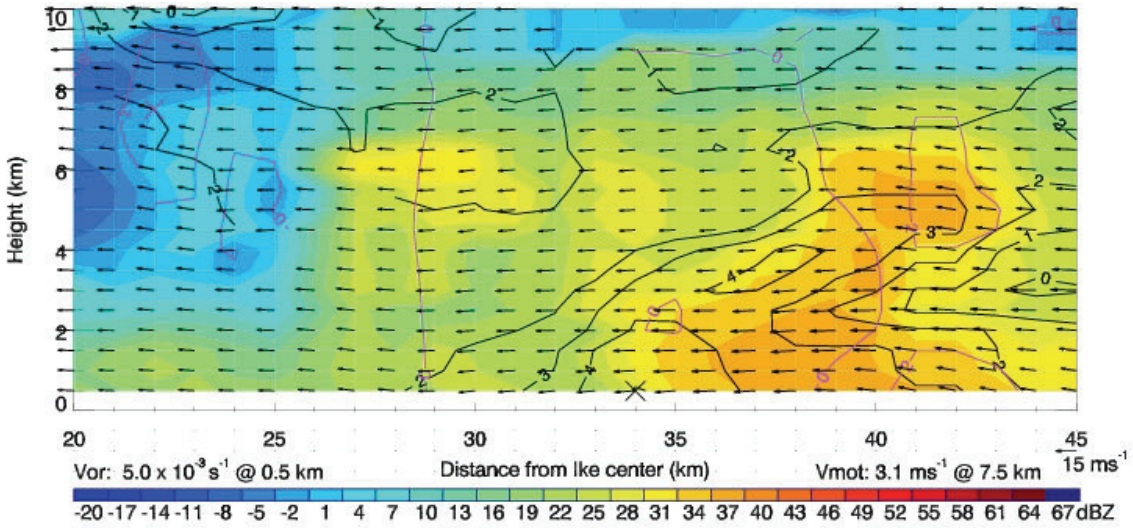

Figure 5.51: MV09 0838 UTC Ike-relative 143.6° azimuth reflectivity (shaded, color bar), vorticity (black, x 10^{-3} s^{-1}), vertical velocity (violet, m s^{-1}) and wind vectors (scaled 15 m s^{-1} vector above color bar).

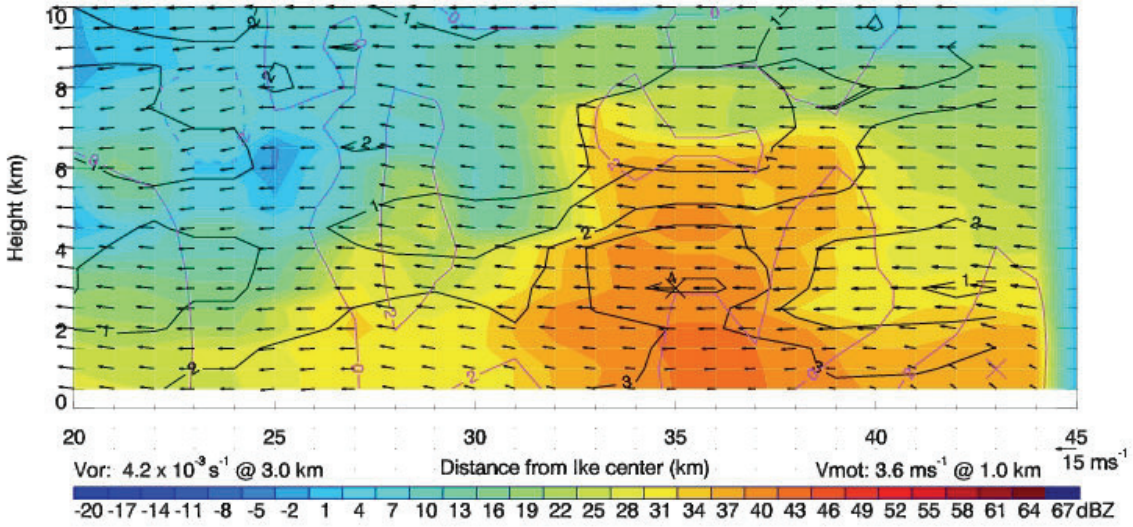

Figure 5.52: MV09 0838 UTC Ike-relative 156.4° azimuth reflectivity (shaded, color bar), vorticity (black, x 10^{-3} s^{-1}), vertical velocity (violet, m s^{-1}) and wind vectors (scaled 15 m s^{-1} vector above color bar).

range. The 3 x 10^{-3} s^{-1} contour that encloses this point extended radially outward and up to 5.5 km. By 156.4°, though, the same contour level reached 1 km lower and was less extensive in range, but the peak vorticity in the plane was contained in it at the 3 km height 35 km from the storm center. Maximum vertical velocity in this plane was slightly stronger and located just beneath the 1.5 km maximum.

The first analysis of MV09 in the NW lobe for its last set of analysis times was suspect as it was in the region blocked out for the truck cab of the MAX. Proximate times, however, gave a good look at the feature as it occupied the northwestern eyewall before its Z signature disappeared. Figure 5.53 provides context for the last analysis run on MV09. While the value of the peak 1.5 km vorticity was higher than at the previously shown time (0838 UTC), it remained oriented in an elongated strip, as shown in Figure 5.54. In the analysis times proceeding this (the next available is 0949 UTC),

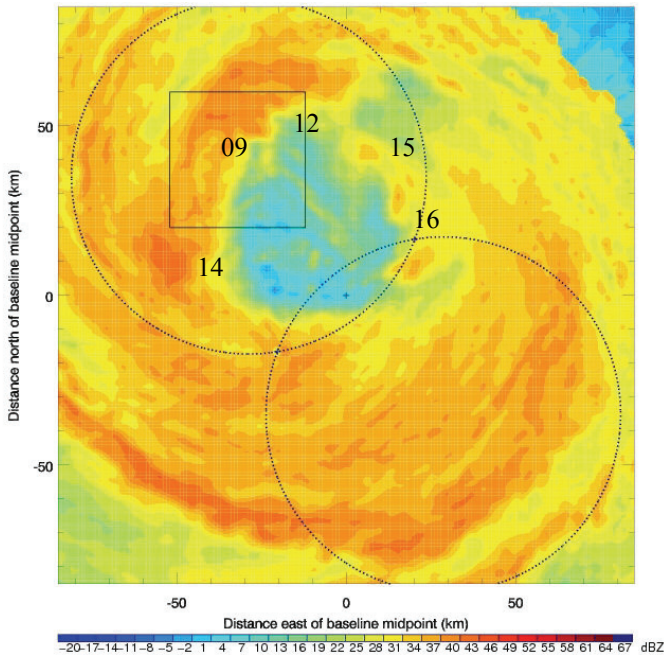

Figure 5.53: Context for 0933 UTC analysis of MV09.

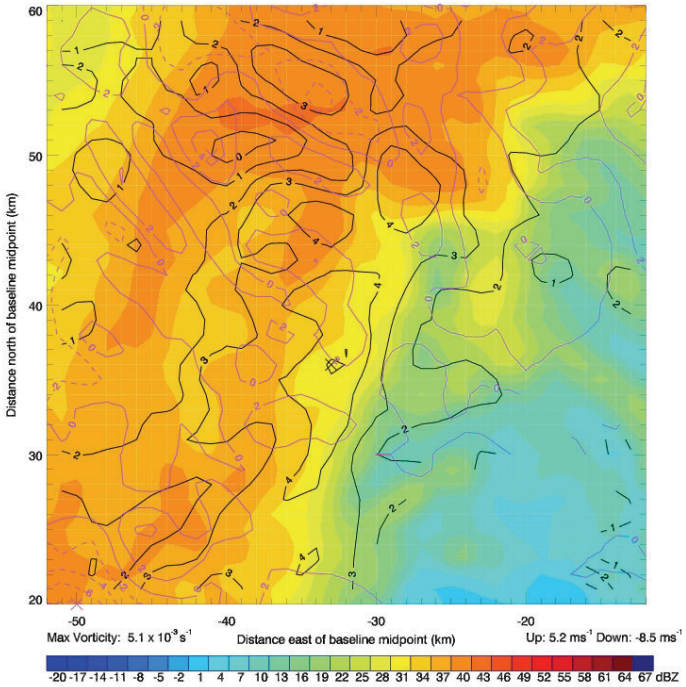

Figure 5.54: MV09 0933 UTC 1.5 km reflectivity (shaded, color bar), vorticity (black, x 10^{-3} s^{-1}) and vertical velocity (violet, m s^{-1})

the Z kink that had accompanied the feature was not clear, and MV09 was not visible in the eyewall evolution beyond 0945 UTC (Section 4.2, Figure 4.10b).

5.10 MV10

Beginning at 0516 UTC (Figure 4.7c), the section of the eyewall between MVs 03 and 05 elongated and started taking on is own arced shape as the initial stages of MV10 in the eastern eyewall (right rear quadrant). MV10 completed two passes through the SE lobe before it merged with MV03. During its first pass in the SE lobe at 0525-0612 UTC, MV10 moved from the northeastern to northwestern eyewall. It hugged the edge of the lobe on its way back S, and reentered the lobe in the southern eyewall at about 0700 UTC. MV10 then traveled up the eastern eyewall before its merger with MV03 just inside the NW lobe near 0800 UTC. While distinct on its own, MV10 completed one revolution of the eyewall in just under 3 h.

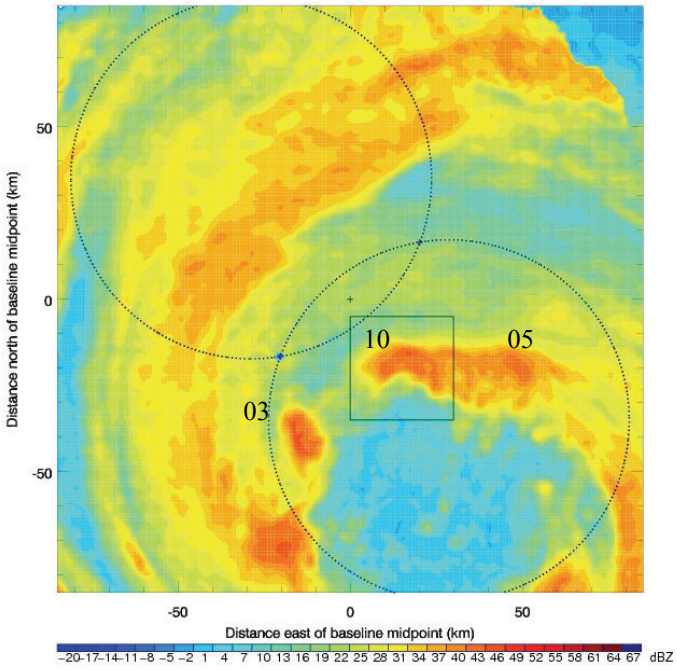

Figure 5.55: Context for 0554 UTC analysis of MV10.

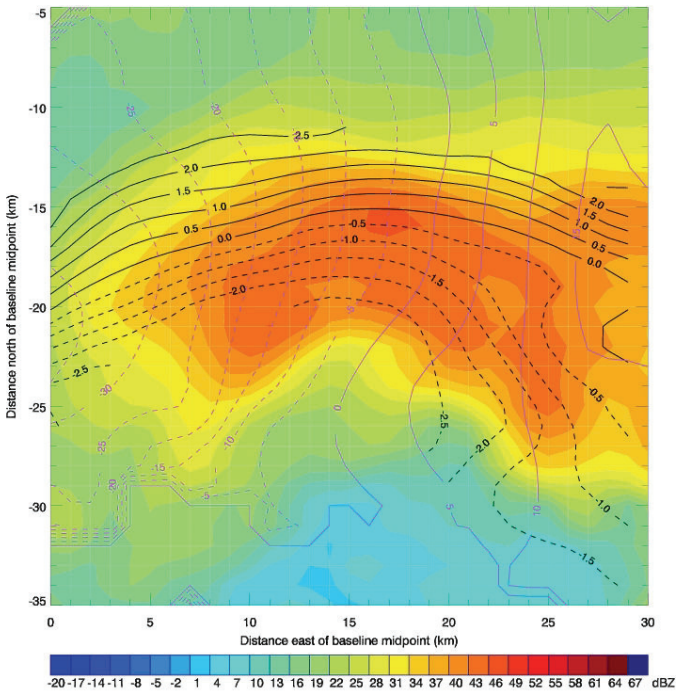

Figure 5.56: MV10 0554 UTC 1.5 km reflectivity (shaded, color bar), pressure perturbation (black, hPa) and radial wind component (violet, m s^{-1}).

At the earliest analysis times, the configuration of the updrafts relative to the vorticity peak followed the trends shown for previous MVs. The maximum vorticity was just down wind of the kink or arc in the Z field, and the peak vertical velocity transitioned from the rear side to the leading edge as MV10 moved from NE to NW of the eye, akin to behavior noted for MVs 03, 05 and 09 in previous sections. When MV10 was in the best geometric placement of its first pass (0554 UTC, context given in Figure 5.55), a nearly closed -2.5 hPa contour suggested lower pressure in central part of the MV (see Figure 5.56). This is very similar to that shown for MV07 at 0424 UTC in Figure 5.35.

When MV10 reentered the SE lobe near 0700 UTC, results showed a pattern like that of MV05 at 0728-0738 UTC (Figures 5.20 - 5.26). The preferred area of upward motion transitioned as MV10 occupied the eastern eyewall. Figure 5.57 shows context for the MV's location at 0728 UTC. The 1.5 km vorticity peak lead the northward moving entity and the updraft maximum was located near the center of the Z signature, E of the largest vorticity (Figure 5.58). This progression depicted the patterns that occurred in previous eastern eyewall MVs. Convergence imposed on the cyclonic flow by MV10's vorticity center led to the location of maximum horizontal winds on the outer side of the MV, as was the case for MV05 when it was in the southeastern eyewall (refer to Figure 5.22).

The range of the radius-height cross sections indicated in Figure 5.58 extend 20-45 km from Ike's center. Because of the location of the vorticity peak at the NW corner of the domain, results along the 57.1° azimuth are limited. Figures 5.59 and 5.60 show retrieved fields along the vertical section passing through the 1.5 km maximum vertical motion (81.0° azimuth). As noted for previous results, divergence was strongest

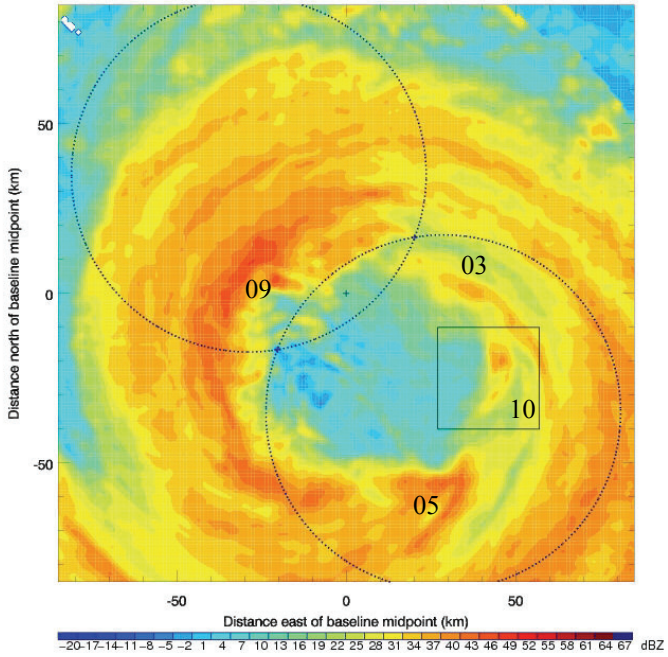

Figure 5.57: Context for 0728 UTC analysis of MV10.

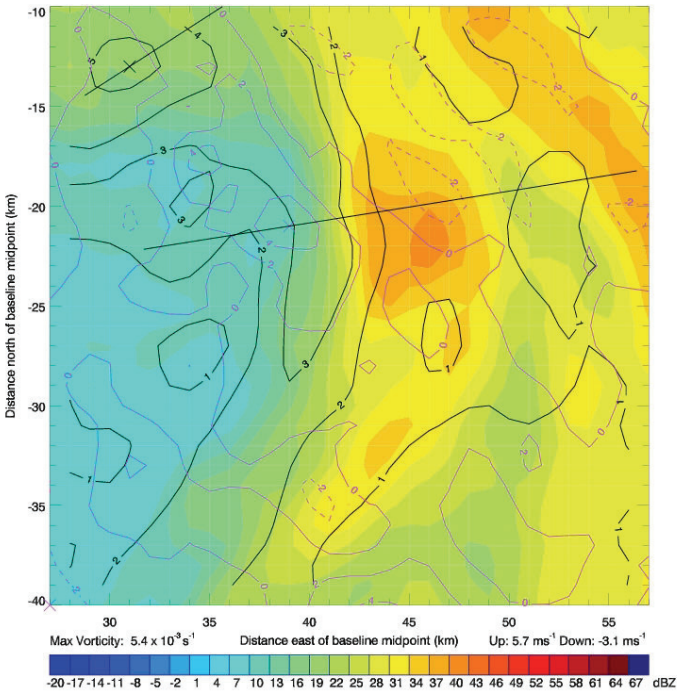

Figure 5.58: MV10 0728 UTC 1.5 km reflectivity (shaded, color bar), vorticity (black, x 10^{-3} s^{-1}) and vertical velocity (violet, m s^{-1}). Straight lines indicate vertical sections along Ike-relative radials at 57.1° and 81.0° azimuths extending 20-45 km in range from the storm center.

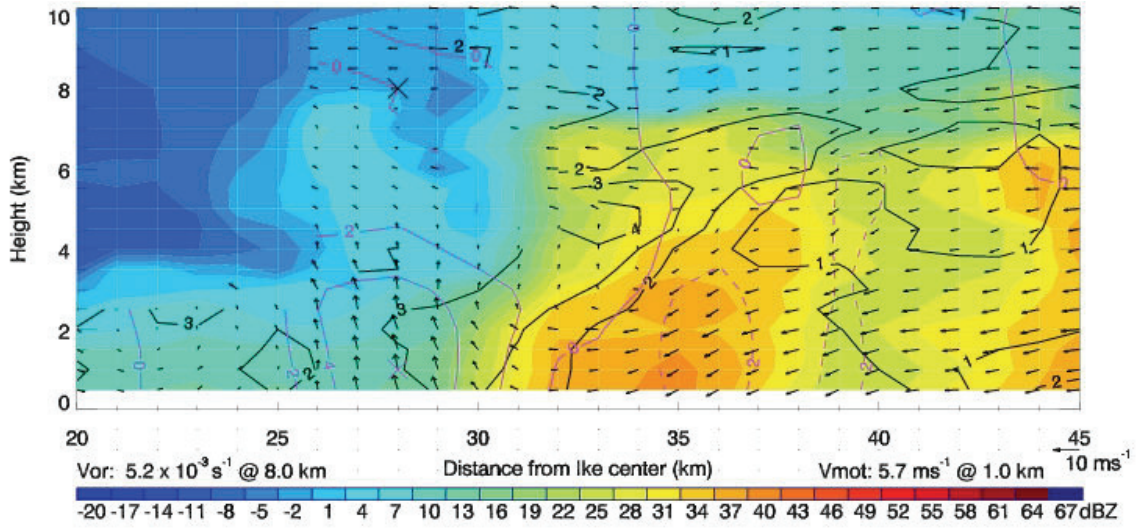

Figure 5.59: MV10 0728 UTC Ike-relative 81.0° azimuth reflectivity (shaded, color bar), vorticity (black, x 10^{-3} s^{-1}), vertical velocity (violet, m s^{-1}) and wind vectors (scaled 10 m s^{-1} vector above color bar).

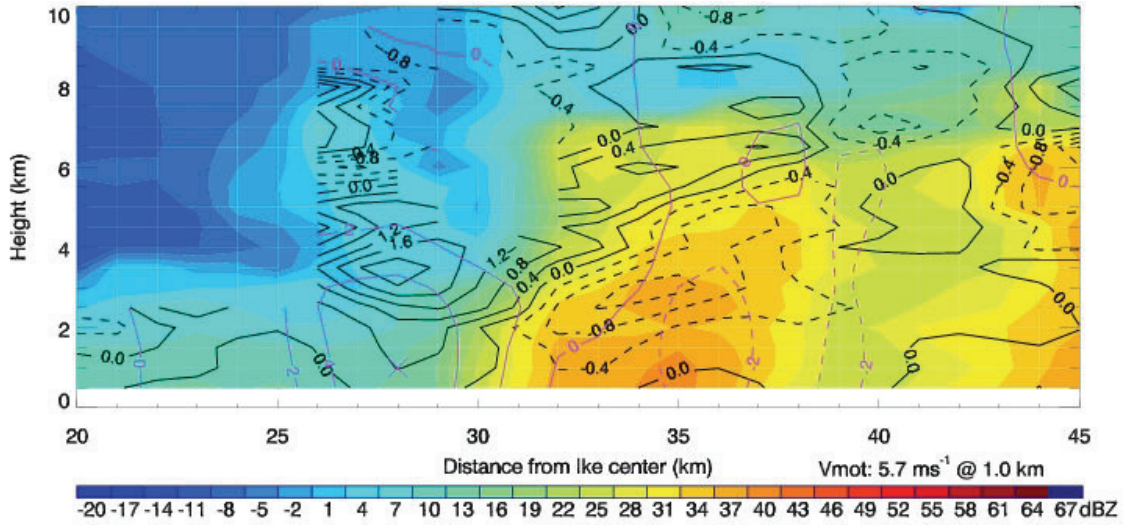

Figure 5.60: MV10 0728 UTC Ike-relative 81.0° azimuth reflectivity (shaded, color bar), divergence (black, x 10^{-3} s^{-1}) and vertical motion (violet, m s^{-1}).

above the updraft maximum at 28 km range, and convergence occurred over the downdraft centered at about 35.5 km range. The radial wind component was inward beyond the updraft, and outward along the inner side of it. Maximum vorticity occurred near the edge of the resolved area. The 3 x 10^{-3} s^{-1} contour exhibited the tower-like appearance seen in previous MVs, reaching up to about 5.5 km and extending outward along the inner edge of the eyewall.

Final analysis times of MV10 were during its merger with MV03 in the northwestern eyewall. At 0801 UTC (Figure 5.17), one vorticity center was evident for the merging entities. This combined feature did not persist long enough to circle back into the SE lobe, but the results from the last analyses on MVs 03 and 10 in the NW lobe clearly showed the MVs merging together (see Section 5.3).

5.11 Non-MV11

The small, short-lived entity investigated as feature 11 formed near 0615 UTC (Figure 4.7h) as a notch in the Z field along the inner edge of MV07 when it was at its largest. The peak vorticity in the analyses of 11 was never above that of MV07, and other fields were not robust at any of the analysis times. After MV07 and 11 crossed the baseline and exited the SE lobe near 0630 UTC, feature 11 became lost in the Z field. For these reasons, feature 11 could not be deemed an MV.

5.12 Inland MV12

At 0700 UTC, as Ike made landfall, a slight Z curl appeared between MVs 09 and 03 (Figure 4.8d). This area became MV12, and was distinguishable for about 1.5 revolutions about the eye. The most interesting results for 12 were at the last analysis

times, when it broke from the arrangements seen for previous MVs. Overall, MV12 completed about 1.5 loops about the eye within 3.5 h.

Early analyses of 12 were performed as it appeared in the SE lobe. Results for these early times were difficult to interpret as little was resolved in the analysis domain. MV12 crossed the baseline after this, and the next two analyses (0738 and 0747 UTC) occurred near the baseline. At these times, MV12 was in the northwestern eyewall and the vorticity peak was located at the front of the Z signature, led by the point of maximum vertical motion, similar to the configuration seen for MV05 at 0829 UTC (Figure 5.30). The second pass MV12 made in the SE lobe began near 0830 UTC, and afforded only a few analysis times as only the southeastern eyewall remained in the lobe. Results for these times indicated that 12's structure was not unlike that of MV05 when it, too, occupied the southeastern eyewall about 1 h earlier (Figures 5.18 - 5.22).

Once MV12 was back in the NW lobe, its associated Z attached to that of downwind MV09 (Figure 4.9g). At the first two analysis times, the structure of MV12 remained similar to that seen in previous northern eyewall MVs: Maximum vorticity occurred near the front or middle of the Z arc, and peak vertical velocities were located to the E; convergence existed at the inner part of the Z signature with divergence at its leading edge, and isopleths of pressure perturbation were orthogonal to those of the radial wind component, which was inward (outward) and the MV's front (back) side (akin to the configurations shown for MV02 at 0458 UTC and MV07 at 0424 UTC in Figures 5.1 - 5.3 and 5.33 - 5.35).

Things changed drastically by 1001 UTC, for which spatial context and results are provided in Figures 5.61- 5.63. The derived vorticity field contained three closed

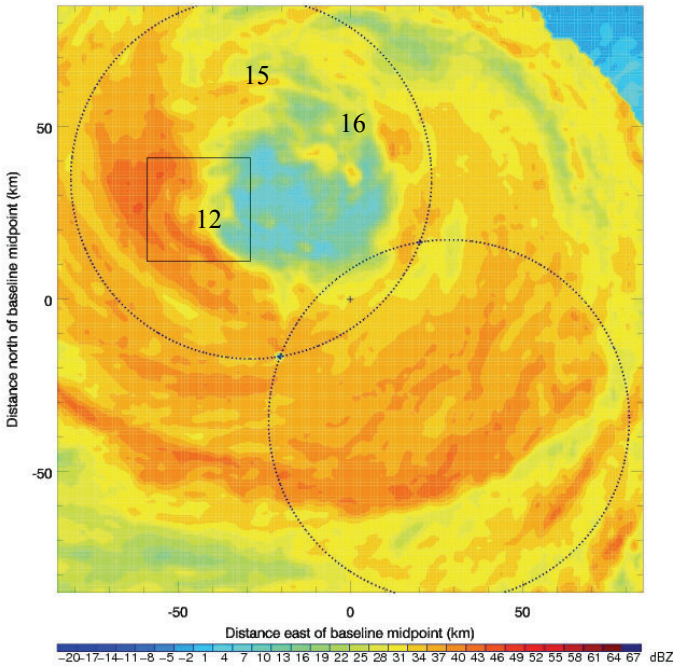

Figure 5.61: Context for 1001 UTC analysis of MV12.

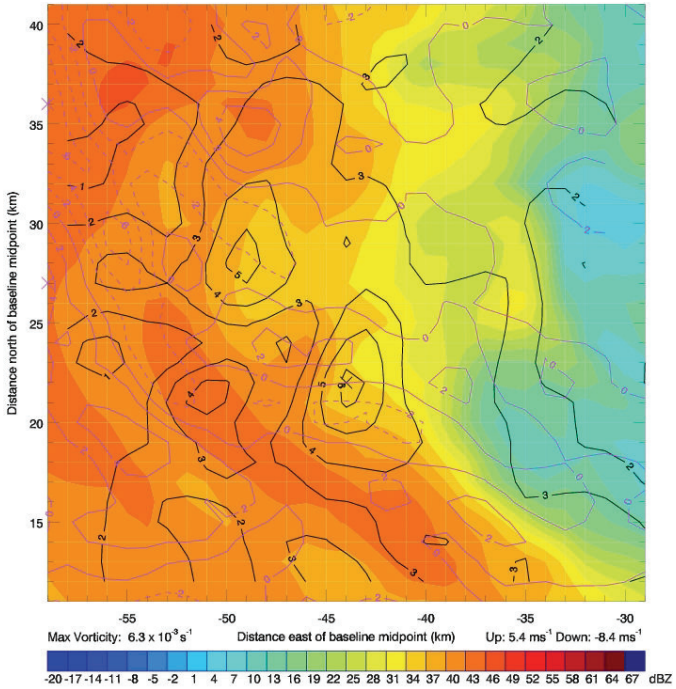

Figure 5.62: MV12 1001 UTC 1.5 km reflectivity (shaded, color bar), vorticity (black, x 10^{-3} s^{-1}) and vertical velocity (violet, m s^{-1}).

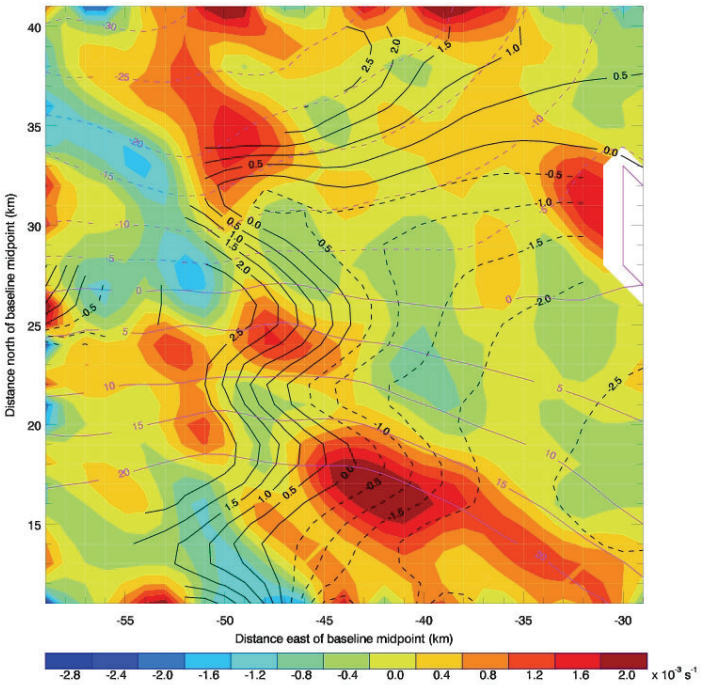

Figure 5.63: MV12 1001 UTC 1.5 km divergence (shaded, color bar), pressure perturbation (black, hPa) and radial wind component (violet, m s^{-1}).

contours of 4 x 10^{-3} s^{-1}, two of 5 x 10^{-3} s^{-1} , and a peak vorticity value of 6.3 x 10^{-3} s^{-1}. All of these vorticity areas occurred near the kink in Z, with the peak value downwind of the others. The very fast development of these peaks was as striking as their demise: Figures 5.64 - 5.66 show that by 1025 UTC, the largest vorticity contour tended toward a strip formation and values at the center of the Z signature were about half or less than the largest value less than half an hour before. Favored locations for vertical motion at these two times was also different than seen for previous MVs. At 1001 UTC, a closed 4 m s^{-1} contour existed to the N and the strongest updrafts were ahead and W of the three vorticity cores. A weaker area of ascent was located just at the middle of them. When the vorticity field had relaxed by 1025 UTC, the maximum updraft occurred in an elongated strip S of largest vorticity.

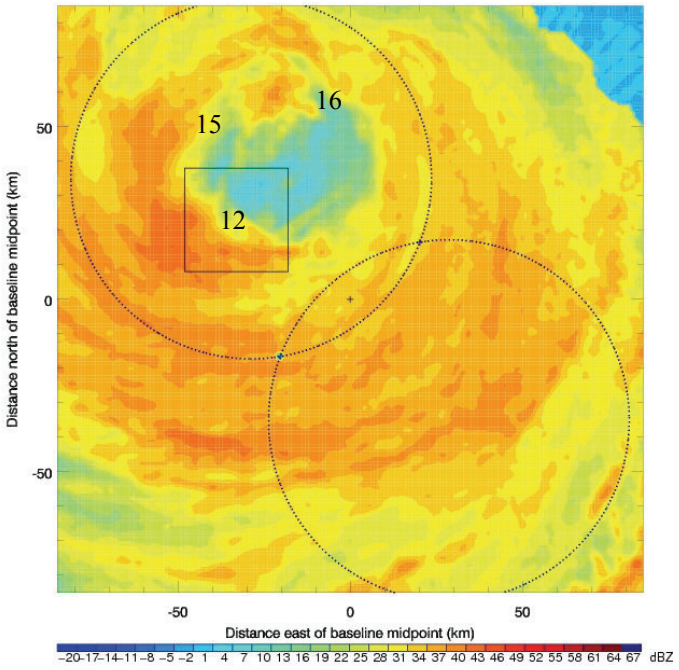

Figure 5.64: Context for 1025 UTC analysis of MV12.

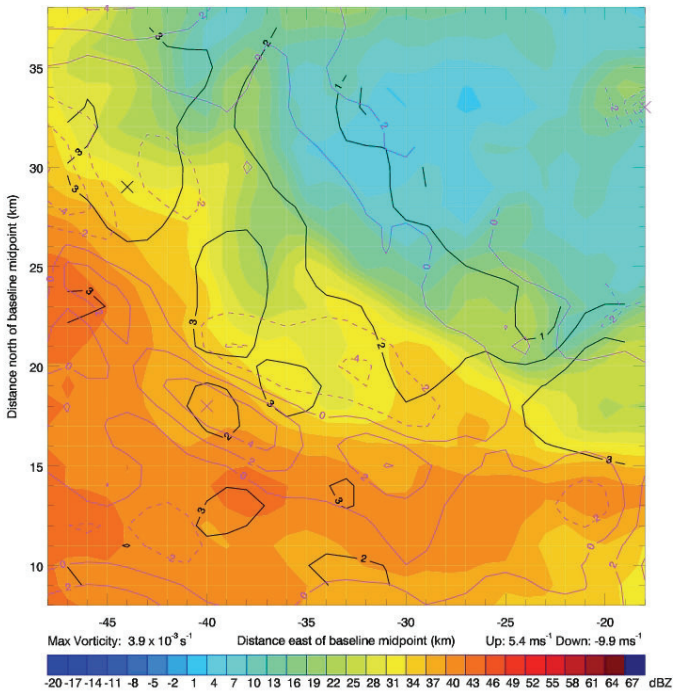

Figure 5.65: MV12 1025 UTC 1.5 km reflectivity (shaded, color bar), vorticity (black, x 10^{-3} s^{-1}) and vertical velocity (violet, m s^{-1}).

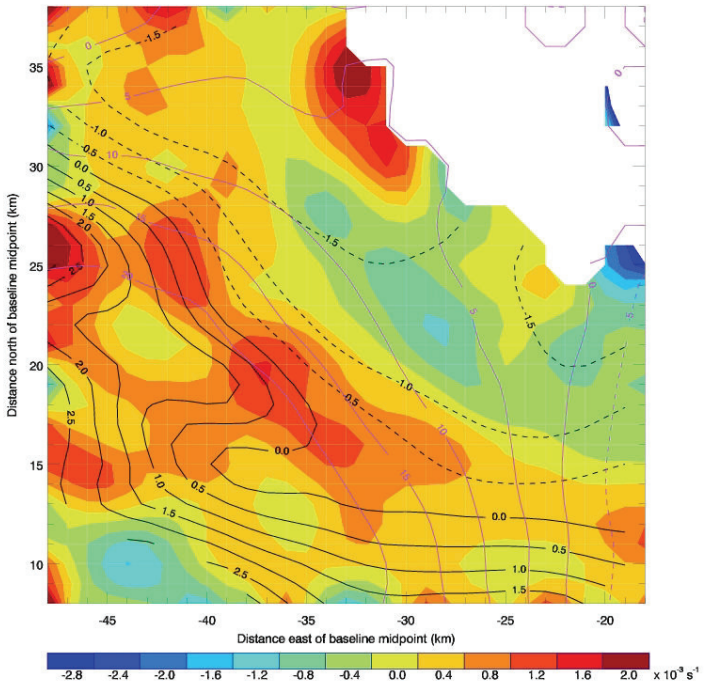

Figure 5.66: MV12 1025 UTC 1.5 km divergence (shaded, color bar), pressure perturbation (black, hPa) and radial wind component (violet, m s^{-1}).

Pressure perturbation and radial wind components behaved erratically at 1001 and 1025 UTC. Not only did the directions of the radial component reverse from the more standard set up (in at the leading and out at the trailing side of the MV), but the pressure perturbation contours zigzaged across MV12, in an extreme version of the inward bend noted at 0838 UTC for MV09 (Figure 5.50). The radial wind component became entirely outward, and the pressure perturbation field contained a fold into the eyewall at 1025 UTC. Slight convergence occurred on the inner side of the Z curl at 1001 UTC, but less than half an hour later any resemblance to the divergence field of previous MVs was gone.

The unique characteristics of MV12 at the later analysis times point to more questions. Behavior of the kinematic fields near 1001 UTC did not follow the trends seen for other MVs. As Ike moved inland and weakened (it was downgraded to tropical storm

status about 8 h later), the eye gradually became obscure. Interactions between MVs and land, in addition to changes in the boundary layer of the storm resulting from the increased surface roughness, are likely to have modified the dynamics that led to MV formation and maintenance. The erratic results for the last analyses of MV12 indicate not only the demise of the entity, but warrant further study on what mechanisms at landfall (and subsequent weakening) alter the arrangement and sustenance of inner core MVs.

5.13 Non-MV13

The next feature analyzed was first visible at 0800 UTC as a notch in the Z field between the merging MV03/10 entity and MV05 in the northern eyewall (Figure 4.9a). It persisted for about half an hour in the NW lobe. Only a few analysis times were available, in all of which 13 possessed no distinct vorticity center of its own. Thus, it was not deemed an MV.

5.14 Inland MV14

When MV07 emerged in the NW lobe near 0845 UTC, a smaller swirled Z shape became evident in the vicinity of its leading edge (Figure 4.9d). This entity developed its own, relatively strong vorticity center as it progressed through the northwestern eyewall, making it MV14. It did not persist for very long, but did provide the best analysis for an MV in the western eyewall. As MV14 neared the baseline, the vorticity center weakened and by 0949 UTC became elongated. Past this time MV14's Z signature was blurred as Ike continued inland.

Results for the earliest analyses of MV14 displayed consistent orientations to other MVs in the northern eyewall. Peak vorticity occurred near the center of the Z arc and upward motion favored the E to NE side of the MV. By 0900 UTC, MV14 was

located in the northwestern eyewall, and results again compared well to previous MVs in the same region as the primary updraft shifted toward the W of the vorticity center (similar to the 0829 UTC results for MV05, Figure 5.30).

Ten min later, MV14 was in the western eyewall. The 0910 UTC analysis of MV14 allowed the best analysis of an MV in that region. Figure 5.67 shows context for its position and remaining panels in the figure show results. The 6 x 10^{-3} s^{-1} vorticity peak was located near the back end of the Z curl and the updraft maximum was to its SW. This orientation fit well with that shown for MVs in other parts of the eyewall (discussed further in Section 5.16). The radial wind component, though, followed the arrangement shown for the late analysis times of MV12, with a reverse to the more typical pattern of inward (outward) flow at the MV's front (back). Convergence occurred near the inner part of the Z signature, but the general character of the divergence was less like that of earlier MVs than the vorticity and vertical motion fields.

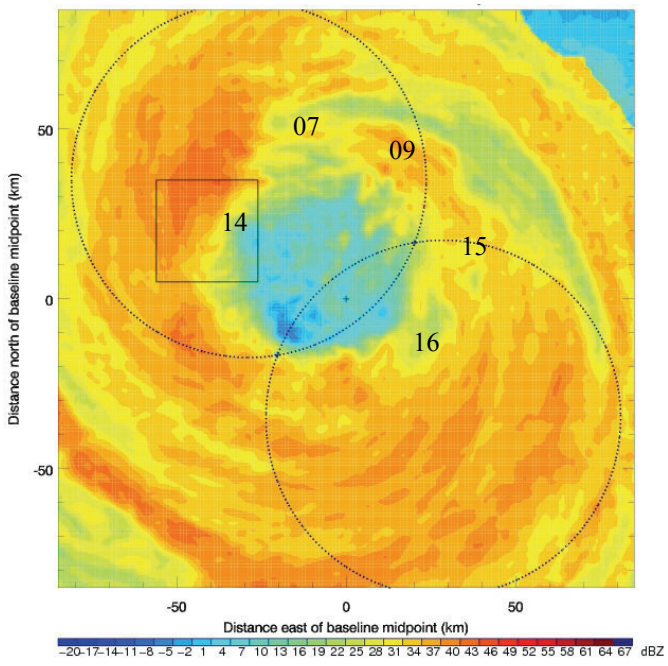

Figure 5.67: Context for 0910 UTC analysis of MV14.

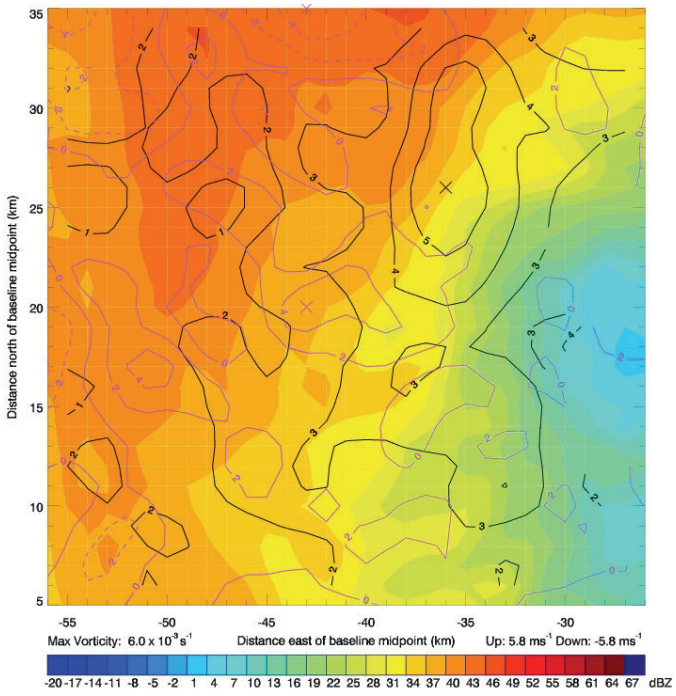

Figure 5.68: MV14 0910 UTC 1.5 km reflectivity (shaded, color bar), vorticity (black, x 10^{-3} s^{-1}) and vertical velocity (violet, m s^{-1}).

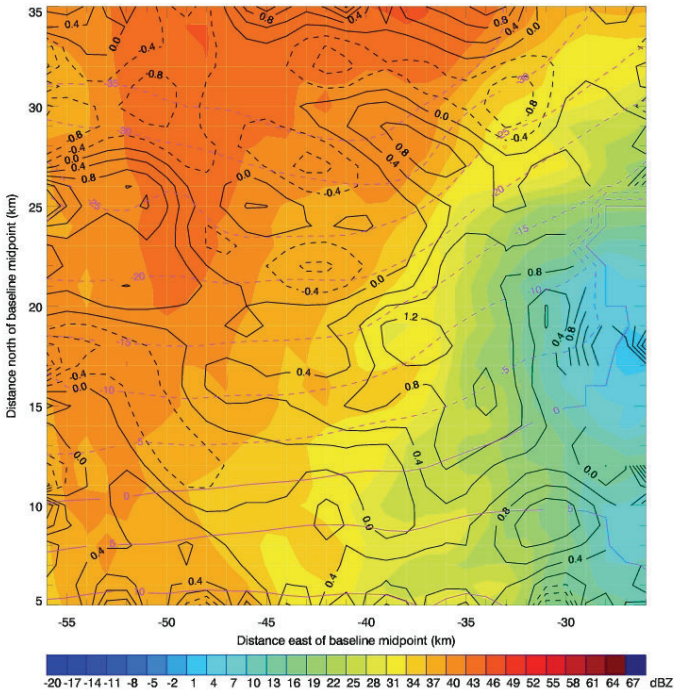

Figure 5.69: MV14 0910 UTC 1.5 km reflectivity (shaded, color bar), divergence (black, x 10^{-3} s^{-1}) and radial wind component (violet, m s^{-1}).

5.15 Inland MVs 15 and 16

At 0900 UTC, a notch in Z upwind of MV12 and an arced segment behind it (Figure 4.9e) began to form what eventually became the circular section (MV15) and northern part of the elliptical portion of the eyewall (MV16) at 1102 UTC (Figure 4.10g). The last analyses in this study are run on MVs 15 and 16 as they moved around the eye and eventually left the dual-Doppler domain while the eye became increasingly obscured after 1200 UTC. Retrieved fields for both MVs were not resolved well compared to the previous MVs, especially beyond 1103 UTC. Meager results for each indicated they did contain a localized vorticity maximum adjacent to their Z signatures. Preferential locations of the maximum updrafts shifted from SE of the vorticity center while the MVs were in the southern and southeastern eyewall and to the N then NW as they propagated around the eye, fitting with the configurations detailed previously. Radial wind component changes for both resembled the behavior described for MV12, with the last resolvable times showing entirely outward radial components.

5.16 Discussion

Overall, the configuration of areas of favored upward motion changed in the MVs at they traveled cyclonically around the eye. These transitions fit well with the conceptual model proposed by B06 (see Figure 2.4). The moderate shear (5-8 m s^{-1}) over Ike in the hours prior to landfall was from the N to NE (Section 2.2, Figure 2.5). At low levels, inflow into the storm interacted with the local vorticity peaks associated with each MV and led to the observed preferential updraft locations. Upward motion favored the radially outward side of the entity and tended to progress cyclonically around the vorticity center with time, as the MV progressed cyclonically around the eye. Table 5.2

lists representative values for the 1.5 km vorticity and upward motion in MVs in various parts of the eyewall arranged well relative to the radars. As in the B06 simulations, updrafts were stronger on the upshear side of the storm (here, the N and NE regions of the eyewall).

Figure 5.70 demonstrates the general arrangement of the kinematic fields observed in mature MVs (in the N eyewall). Locations of each kinematic feature are fairly consistent as the MVs travel around the eye, with the notable exception of the updraft maximum, which transitions around the vorticity center in a manner similar to B06's model (see Figure 2.4, Table 5.1 and Figures referred to therein). This transition is also evident in the schematic Figure 5.71. It shows the general organization of mature MV's kinematic fields (as in Figure 5.70) for the four cardinal regions of the eyewall. Note again that the shear at the time of analysis was generally from the N to NE. In the

Table 5.2: Representative values of 1.5 km vorticity (x 10^{-3} s^{-1}) and updraft (m s^{-1}) associated with the listed MVs in various regions of the eyewall. Note that the strongest updrafts occur when the MV is in the upshear (NE, N) side of the eyewall, consistent with the B06 conceptual model.

Time (UTC)	**MV**	**Eyewall Region**	**Vorticity (x 10^{-3} s^{-1})**	**Updraft (m s^{-1})**
0630	02	E	5.5	6.1
0424	07	NE	5.0	10.8
0535	03	N	6.2	6.8
0910	14	W	6.0	5.8
0728	05	S	6.6	5.8
0838	09	SE	4.7	3.5

vertical, tower like structures of vorticity occur in mature MVs. The vertical extent of this elevated vorticity aloft decreases as the MVs decay and the hurricane moves inland.

The secondary circulation of a hurricane is characterized by low level inflow. The observation of the shift of the radial flow in the MVs investigated is conceptually consistent with the presence of the MV vorticity peak within the larger scale TC circulation. A similar behavior in the radial wind component was noted by Marks et al. (2008) near the mesovortex encountered by a research aircraft in Hurricane Hugo (1989). The reversal of this shift seen in MVs 12 and 14-16 is odd. It may be attributable to the fact that the 1.5 km level used to assess the results may be above the inflow layer, or other errors in the analysis technique (use of a coarse storm center estimate), but most likely was caused by Ike's weakening as it moved inland. The 1.5 km height was used in this study to ensure complete coverage of the entities by both radars at the lowest possible heights. For features analyzed while at farther ranges (i.e., beyond about 60 km) from either radar, the lowest elevation scans actually sampled approaches 1 km, and this height can be exceeded for longer ranges, especially for most of the MAX volume scans where the lowest elevation was 0.8°.

Attenuation in rain at X-band can be substantial. Also, for many of the analysis times both radars are embedded in portions of Ike's eyewall or heavy rainbands. At such times it is very likely the radomes of both radars were coated in a layer of water that would have attenuated the signal before it left the radar and again on return (Doviak and Zrnic 1993). Signal degradation and eventual loss from MAX had an obvious impact on the quality of results for MVs that occurred far from that radar, as noted for many cases above. Qualitatively, though, the horizontal characteristics of the results are encouraging

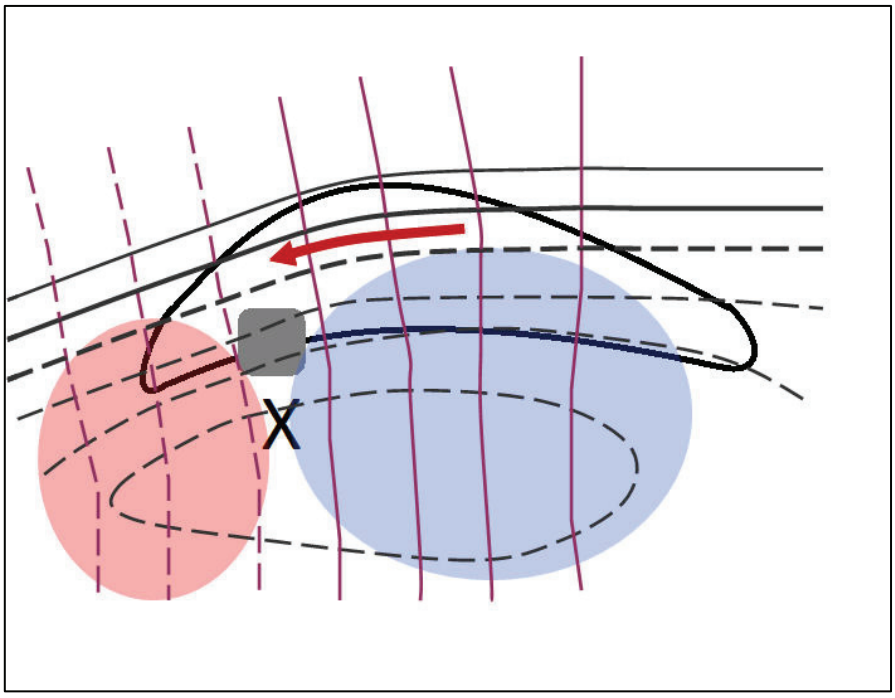

Figure 5.70: Schematic of the general arrangement of low level kinematic fields in Ike's MVs. This image was crafted for an MV in the N eyewall, but most fields were structured similarly as the MVs progressed around the eye. The arced shape outlined by the thick black line indicates the area of enhanced reflectivity (≥ 30 dBZ). The approximate location of maximum vorticity is labeled by an X. Solid (dashed) gray lines denote positive (negative) pressure perturbations, and solid (dashed) violet lines show outward (inward) radial wind components. Blue (red) shading shows areas of enhanced convergence (divergence), and the red arrow denotes the area prone to the highest local horizontal winds. Maximum upward velocity favors the region shown by the grey square. Note: the relative placement of preferential upward motion changed as the features moved about the eye (see Table 5.1), but characteristics of the other fields were comparable to those shown here.

as they relate well to previous work (KS01, B06). KS01's work was the first modeling study to show that mesovortices could contain isolated pressure minima, though such behavior was found in observations in earlier hurricanes (e.g., Willoughby and Black 1996, Marks et al. 2008). It is possible that the results for MVs 07 and 10 again confirm this, at least from the perspective of the deviation from the mean pressure and within the constraints of the retrieval method outlined in Chapter 3. The B06 simulations of Bonnie

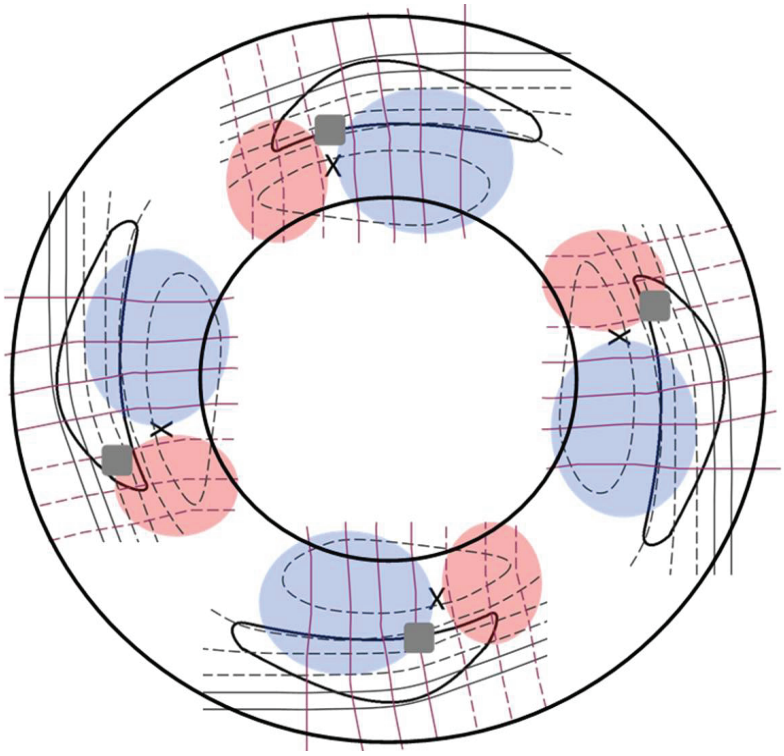

Figure 5.71: Schematic of MVs in cardinal regions of the eyewall. Lines and shading as in Figure 5.70.

produced MV pressure perturbations up to 3 hPa, on par to the values derived here for Ike. Also consistent with the results of KS01 and B06 is the preferred location of the vorticity peak downwind of the kink or arc in Z.

Results in the horizontal and vertical planes indicated the presence of an unstable configuration in the primary vortex. Barotropic instability is seen often in the analyses as perpendicular radial wind and pressure perturbation isopleths, a representation of horizontal shear in the vicinity of the "jet" along the sharp pressure gradient of the eyewall. This characteristic orthogonality becomes blurred at the late analysis times, especially in the case of MV12, suggesting a break down of the processes marinating the MVs as Ike continued inland. B06 showed that MV updrafts can act to strengthen local vorticity via stretching, and thereby constantly replenish the high vorticity annulus,

aiding the maintenance of existent MVs and generation of new ones. In the vertical, tower-like structures of elevated vorticity suggested this type annulus rebuilding, and also resemble the more unstable Regime 1 presented by KE01. As the MVs weakened (and especially as Ike moved further inland), large vorticity contours (3×10^{-3} s^{-1}) did not extend much above the 3 km level. If the vorticity in the central eye at these times were to have increased, then KE01's second, more stable Regime 2 may have been achieved at times when the MVs were much weaker. Determining the value or even trend of the value of the *eye* vorticity, however, is impossible with this method alone due to a general lack of scatters in the central eye.

The highly variable nature of the updrafts (see Table 3.1) is difficult to ascribe solely to the MVs without noting problems that complicate their derivation. Doviak et al. (1976), Davies-Jones (1979), Clark et al. (1980), Matejka and Bartels (1998) and others have shown that dual-Doppler estimates of vertical velocity are generally worse (relatively) than those for the horizontal wind speed and will be further degraded for non-ideal geometries (Section 3.2). This known problem can be compounded by the chaotic flow field in the domain and that this study employs only an averaged advection for the analysis. Keeping this in mind, though, peak values of up and down vertical motion computed for Ike's MVs were within the upper 5-10% for eyewall updrafts as reported in works by Jorgensen et al. (1985) and Black et al. (1996). While it is difficult to rely on the exact values obtained in these analyses because of the numerous sources of error, the occurrence of extreme wind values in the vicinity of TC eyewall MVs is not unprecedented: Aberson et al. (2006) showed the existence of an updraft on the order of 20 m s^{-1} near an MV in Hurricane Isabel (2003). Marks et al. (2008) found an updraft

maximum of 16 m s^{-1} attendant to the Hugo MV. Updrafts in B06's simulated Bonnie MVs peaked at 10-15 m s^{-1}. So, while there are errors present in the values reported in Table 3.1, vertical velocities found when MVs were in good locations relative to the radars agreed reasonably well with previous work.

CHAPTER 6

SUMMARY

Organization of the kinematic fields in the MVs of Ike was investigated via dual-Doppler analysis from the KHGX and MAX radars (Figure 1.1). The analysis employs downward integration of the mass continuity equation and uses a bulk estimate of particle fallspeed derived from the KHGX reflectivity. Initial analysis is performed on a 160 x 160 x 10 km grid with 1 km horizontal and 0.5 km vertical spacing, centered on the midpoint of the baseline. Forward speed of the hurricane, interpolated from the Best Track record, is used for the advection in the larger domain runs. A smaller analysis domain is placed over the feature of interest, usually 30 x 30 x 10 km, with the same spacing as the larger domain. The average horizontal velocity retrieved in the first run over the entire second domain is used for the advection in a new run on the smaller domain to retrieve the vertical vorticity (references to "vorticity" indicate the vertical vorticity unless otherwise stated), divergence, horizontal and vertical winds, and perturbation pressure fields. A total of 166 smaller domain runs were completed on 16 arced Z features that developed along the inner edge of Ike's eyewall. All but 2 of the 16 features were found to contain localized peaks in vorticity and were deemed MVs.

A summary of conclusions drawn from the results are provided first in this chapter, followed by a brief reminder on the errors inherent in the analysis. Ongoing and future work are discussed last.

6.1 Conclusions

Vorticity centers for the MVs were all located at either the leading edge or near the middle of the arced shape of elevated Z (≥ 30 dBZ). The configuration of the maximum vertical velocity relative to the vorticity centers (both at the 1.5 km level) of the observed MVs changed while the features progressed around the eye. Maximum updrafts preferentially occurred generally radially outward from the vorticity peak, as characterized in Table 5.1 and Figure 5.71. These favored locations are very consistent with earlier modeling work. KS01 showed the location of MV vorticity centers favored the downwind side of the "kink" in the Z field, and transitions in the updraft location found here fit with B06's conceptual model of MV updraft behavior (Section 2.1, Figure 2.4).

Magnitudes of the maximum (1.5 km level) vertical velocities varied greatly (Table 3.1), but ranged about 7-10 m s^{-1} for the most vigorous MVs in good geometric placement in the lobes. As noted in Section 5.16, these are within the upper 5-10% of eyewall updrafts according to the findings of Jorgensen et al. (1985) and Black et al. (1996). Despite the various errors involved in their retrieval, the values found in this study are not drastically different from updraft velocities reported in MVs of previous TCs. Jorgensen (1984) used airborne radar data to estimate convective scale updrafts of 7-9 m s^{-1} in MV-like features in the eyewall of Hurricane Allen (1980). The entities were visible in individual flight legs, but were not able to be tracked due to the ~20-30 min

time frame it took to complete each pass. Maximum vertical motions in the Hugo and Isabel MVs were stronger (both > 20 m s^{-1}), but this does not come as a surprise as the vorticity peaks and local pressure anomalies were also more vigorous in those hurricanes' MVs than in Ike's: the strongest observed Isabel MV had a vorticity maximum of 15 x 10^{-3} s^{-1}, maximum updraft of 25 m s^{-1}, and pressure anomaly of nearly 4 hPa (Montgomery et al. 2006, Aberson et al. 2006). In the Hugo MV discussed by Marks et al. (2008), these values were 1.25 x 10^{-1} s^{-1}, 21 m s^{-1} and 12 hPa, respectively. Comparison to these values requires one to keep in mind that the MVs reported in Hugo and Isabel were smaller in spatial scale than the MVs in Ike.

Convergence tended to occur in towards the MV center, with divergence typically found just downwind of the entity (depicted in Figures 5.70 and 5.71). At mature MV stages, contours of pressure perturbation and the radial wind component were nearly perpendicular. As the features weakened this arrangement became less striking, indicating a decrease in the barotropic instability. A distinct shift in the sign of the radial wind component occurred with each MV. A similar switch was reported in the case of Hugo by Marks et al. (2008), with 8 m s^{-1} outflow changing to 12.5 m s^{-1} inflow across the MV and the sign change roughly coincident with the vorticity center. For some analyses, the maximum horizontal wind speed in the small domain occurred in the vicinity of the MV, on its radially outward side. Such instances can be simply understood as the influence of local cyclonic motion on the larger scale wind field, so that on the side of vorticity that matches the primary flow winds are enhanced. This phenomena occurred in the MVs of Andrew, and led to the most destruction associated with that storm's landfall (Willoughby and Black 1996). Montgomery et al.'s (2002) fluid

in a box experiments showed that the increased horizontal winds on the radially outward side of MVs can reach up to 150% the value of the main TC winds. Obviously, such events can exponentially increase property damage if a strong MV passes at landfall (as happened in the case of Andrew) and warrant continued research to attempt mitigate the threat they can also pose to life. The MVs in Ike were not explicitly correlated to increased damage (J. Schroeder and K. Knupp 2011, personal communication). It's likely the intensity and relative sizes of these storms (Andrew made landfall as a compact category 5 storm, Ike as a very large category 2) played a significant role in this difference. However, not every small domain run resulted in a peak horizontal wind near the MV, which warrants further investigation and comparison of Ike's MVs to those in other landfalling TCs.

Vertically, the MVs' arced Z shape echo tops extended up to about 6-8 km, though a few were slightly taller. Most MVs in previous studies have comparable vertical extents, with the exception of the very small, shallow MV in Isabel that did not reach much above 2 km (Aberson et al. 2006). The features documented by Jorgensen (1984) in Allen went up to about 6 km, and the one observed in Hugo extended up to nearly 7 km (Marks et al. 2008). The entities typically contained a tower of elevated vorticity to at least mid-levels (≥4 km). Such a result is consistent with the unstable Regime 1 outlined by KE01 (Section 2.1, pg 8-9 and Figure 2.1). Over time, in a combination of the weakening of the storm as it moved inland and the weakening of the MVs, the vorticity towers diminished, implying either a tendency towards KE01's more stable Regime 2 (Section 2.1, Figure 2.1) or a combination of that process, the weakening

of the storm as it made landfall and encountered greater surface roughness that modified the hurricane boundary layer.

Occasionally, results indicated a closed or nearly closed minimum in the pressure perturbation field. While not seen for every MV, local pressure minima in these types of features have been shown previously in both modeling work and observations. MVs that developed in KS01's numerical experiments exhibited local pressure minima, often lower than that of the parent vortex. Observations of MVs in Hurricane Andrew indicated one feature with a pressure lower than that in the central eye, as reported by Willoughby and Black (1996). Recall, however, that formation of the MVs in the case of Andrew occurred as a result of the interaction of the eye with the coastline, whereas in Ike the MVs began developing while the inner core was still well offshore (Chapter 4). As noted above, local pressure anomalies were also found for MVs in the eyewalls of Hugo and Isabel.

Other than the transitions of the preferred updraft locations, patterns in the vorticity, divergence, radial winds and pressure perturbation fields were remarkably similar for the MVs, no matter which portion of the eyewall they occupied (Figure 5.70). Magnitudes of the vorticity, vertical velocity peaks, and pressure perturbation minima ranged as follows for mature MVs in the best positions relative to the radars: Vorticity maxima were over 4 x 10^{-3} s^{-1}, and up to 7-8 x 10^{-3} s^{-1} for the most vigorous features. Updrafts were generally 7-10 m s^{-1}. Local minima in pressure perturbations were not resolved for every MV, but for those where a closed or nearly closed contour occurred magnitudes of the perturbation were 2.5-3 hPa. Radial wind component changes across the best observed of Ike's MVs (before landfall) shifted from outward at the back to

inward at the front. As noted above, the switch in sign occurred nearly coincident with the vorticity peak. The results of this study add much to the growing body of work on TC inner core MVs, and are quite consistent with earlier modeling and observational studies, in spite of the many assumptions and errors inherent in the analysis methodology.

Unlike all pervious observational studies that have detailed MVs, to the author's knowledge the present work is the first to provide a long-term (nearly 10 h) view of the entities and their attendant kinematic signatures as they occupy almost every region of the eyewall (Table 5.1 and figures referenced therein). Earlier radar studies that examine MVs have utilized airborne radar data. It is suggested here that a well-oriented ground-based network of multiple Doppler radars might be a more consistent way to observe eyewall MVs as the stationary radars can sample the features in a more continuous manner than achieved with aircraft. This does of course require that the observed TC develop an MV regime and pass within range of the network. In this regard, our observations of Ike's MVs appear rather serendipitous.

The majority of Ike's MVs formed prior to landfall. Exceptions to this initially display similar characteristics to the earlier MVs. However, as the hurricane moved inland, the organization of the kinematic fields lost resemblance to results found for the earlier entities that formed while most or all of the eyewall was over water. It is highly probable that the dynamical processes governing the development and maintenance of the MVs are augmented as the storm moves from over the sea to land. Abrupt changes in surface roughness at the coastline modify the hurricane boundary layer, which is vital to the storm's persistence. These alterations are likely to have an impact on the rearrangement of the high vorticity of the eyewall. Exactly what these implications are

remains an unanswered question until a more complete understanding of both the unaltered processes (i.e., further advances to S99's theoretical work) and the impact of surface changes on the hurricane boundary layer is achieved.

6.2 Error discussion

In order to perform the retrievals from the data collected by KHGX and MAX, many assumptions were made. Inescapable, but not always correct, these assumptions lead to errors in the resulting values. Non-simultaneous sampling, advection and evolution of the observed area airflow, incomplete sampling of the lowest and highest levels' divergence, the underdetermined nature of a dual-Doppler system, accumulation of errors through and insufficient boundary conditions for the vertical continuity integration all affect the accuracy of the retrieved wind field (Section 3.2) and the pressure perturbations derived from it (Gal-Chen 1978). Apart from further complications arising from the assumptions of uniform advection and storm center location with height (the latter of which may contribute to aliasing of tangential winds onto and incorrect radial wind component), the most deleterious parts of the analysis are the underdetermined nature of the synthesis problem for radial velocities (Clark et al. 1980) and inadequate sampling of divergence. Mentioned in Section 5.16, the lowest elevation scan from both radars do not extend near the surface, and for MVs at far ranges (> 60 km) the lowest sampled height was at or above 1 km. The boundary layer inflow of a TC is vital to the storm's maintenance, and likely contains the most important part of the divergence field. This region is not well observed by the radars, which adversely affects the retrieval of vertical motion. In general, the vertical velocities present here need to be taken with

caution because as with any dual-Doppler analysis this component is the least well represented in the results (Doviak et al. 1976).

Considering the data itself, changes within radar volumes do occur over the time that it takes for each scan to be completed (about 5 min), and this of course violates the steady-state assumption. The evolution of the MVs on this time scale may not be negligible, especially in cases such as MVs 04 and 08 that formed and dissolved within 0.5 h. Non-simultaneous observations are one reason why it is important to use a reasonable advection in the analysis. Furthermore, attenuation in rain at X-band can be substantial. Signal degradation and eventual loss from MAX had an obvious impact on the quality of results for MVs that occurred far from that radar, as noted in Chapter 5. For the Z-fallspeed relation, the Z value from KHGX is used (Section 3.2), but future work to examine hydrometeor distribution first requires correcting the MAX Z and Z_{dr} data for attenuation and differential attenuation (Bringi and Chandrasekar 2001). With corrected Z values, it's possible the maximum reflectivity in a grid box will no longer be the KHGX value, and thus results from the present analyses may be slightly different.

Also noteworthy is that the vertical dimension of the analysis domain and the boundary conditions assumed in the methodology do not consider the possible occurrence of high altitude updrafts and downdrafts. Heymsfield et al. (2010) and Cecil et al. (2010) showed that at heights of > 10 km in TCs vigorous vertical motions can occur. The methodology used in this study was chosen to focus on what structure of the MVs could be resolved, but its method of integration limits the ability to account for such drafts.

6.3 Ongoing and future work

While insightful, results of this work are limited. Investigation here focused on individual MV features, but was merely a first step along a long path of study based on the data collected during Ike. Ongoing and future work aims to eliminate the primary large-scale assumptions relied on in this initial study (that the storm center is constant with height and that the advection over the smaller domains is linear). Beyond these modifications, more study with this dataset has great potential for advancing observational knowledge of TC inner core MVs.

The first step is assessing the actual circulation center of the hurricane at each vertical level in the domain. The center finding and track determination algorithm pioneered by Willoughby and Chemlow (1982) was mainly designed for application to airborne radar data, but can also be employed for ground-based radars. Another possible method for obtaining a more accurate storm center is based on the ground-based velocity track display (GBVTD) technique (Lee et al. 1999, Lee and Marks 2000). The GBVTD method has the advantage of better handling highly asymmetric TCs, and can be applied to a single radar. Future work will involve applying these location algorithms to both the KHGX and MAX data sets and finding a more exact location of the TC center at every vertical level. Once this is completed, a more accurate initial forward storm motion and final storm-relative radial and tangential wind components will be possible. An extended version of the GBVTD (EGBVTD, Liou et al. 2006) technique can be implemented with data from a dual-Doppler network. An instructive future project will involve applying the EGBVTD to Ike dataset and comparing its derived wind field to that obtained from the dual-Doppler analysis.

Another primary assumption used here that may be alleviated with ongoing work is the use of a linear advection vector for the smaller domain analyses. As explained in Section 3.2, the present methodology simply averages the derived wind from the larger domain analysis over the entire smaller domain, and this mean wind is used as the uniform advection in the small domain runs. For translating supercells and typical mid-latitude convection studies, a simple storm motion vector is generally acceptable. Within a hurricane, however, advection speed and direction become more complicated. Shapiro et al. (2010a,b) introduced a procedure that determines spatially varied advection components. A proposed version that includes a time variation is also presented. Their application of a derived variational advection field to correct Z and radial velocity fields for non-simultaneous measurement effects are encouraging, though the latter requires improvement. Efforts to extend the present study include the implementation of Shapiro et al.'s procedure for generating the spatial (and eventually, time) variant advection components and applying them as more accurate representation of the movement of the MVs than the simple averaged vector.

This work focused on the individual MVs that formed along Ike's inner eyewall. As mentioned in Section 2.2, the propagation of VRWs in TCs can be manifested in the form of instabilities similar to the MV regime. Hurricane Elena (1985) displayed VRW characteristics as it approached the N Gulf coast (Corbosiero et al. 2005, 2006). The Corbosiero et al. works detail the intensification of the TC just prior to landfall, and its subsequent development of an asymmetric structure. Wavenumber decomposition of the reflectivity field suggested the presence of vortex Rossby waves (VRWs) that may have acted as an exchange mechanism between the eye and eyewall and spurred the

development of MVs (as in S99). A goal for further analysis of Ike is to complete a similar wavenumber decomposition (via fast Fourier transform) to gain a better understanding of the eyewall evolution. Such an analysis will provide further context for the development of the MVs examined here, and may lend support to the theory of VRWs and their connections to MV regimes.

As mentioned previously, to best use the dual-polarimetric data collected by MAX for further study it must first be corrected for rain attenuation. Ongoing work on this problem has incorporated the attenuation and differential attenuation correction procedure used by Liu et al. (2006), similar to the C-band methodology presented by Bringi et al. (2001). The methods involve a constraint on the differential propagation phase value (Φ_{dp}) to correct the Z data, and the Bringi et al. differential attenuation correction relies on a constrained value for the intrinsic Z_{dr} at ranges beyond attenuating precipitation. Once reasonable corrected MAX Z and Z_{dr} fields have been obtained, work to examine hydrometeor distribution (similar to Snyder et al. 2010), rain rate and liquid water content estimates will ensue.

To bring study on the dataset full circle, simulation of X-band radar observables from S-band Z data may be done on the KHGX data and compared to data collected with MAX. Chandrasekar et al. (2006) presented a method for extracting X-band values from S-band data for use in rainfall estimation. Their method might be applied to the 88-D data from Ike to derive S-band Z_{dr} values that can be used for rain rate and liquid water context estimates. The proxy S-band quantities can then be compared with those found from the X-band data to evaluate differences in the performance of the 2 radar wavelengths for the event.

REFERENCES

Aberson, S.D., M.T. Montgomery, M. Bell, and M. Black, 2006: Hurricane Isabel (2003): New insights into the physics of intense storms. Part II: Extreme localized wind. *Bull. Amer. Meteor. Soc.*, **87,** 1349–1354.

Armijo, L., 1969: A theory for the determination of wind and precipitation velocities with Doppler radars. *J. Atmos. Sci.*, **26,** 570–573.

Bell, M.M., and M.T. Montgomery, 2008: Observed structure, evolution, and potential intensity of category 5 Hurricane Isabel (2003) from 12 to 14 September. *Mon. Wea. Rev.*, **136**, 2023–2046.

Berg, R., National Hurricane Center, cited 2009: Hurricane Ike Tropical Cyclone Report. [Available online at http://www.nhc.noaa.gov/2008atlan.shtml]

Beven, National Hurricane Center, cited 2009: Hurricane Ike Discussion Number 45 [Available online at http://www.nhc.noaa.gov/archive/2008/al09/al092008.discus.045.shtml]

Black, M.L., R.W. Burpee, and F.D. Marks, 1996: Vertical motion characteristics of tropical cyclones determined with airborne Doppler radial velocities. *J. Atmos Sci.*, **53**, 1887-1909.

Braun, S.A., 2002: A cloud-resolving simulation of Hurricane Bob (1991): Storm structure and eyewall buoyancy. *Mon. Wea. Rev.*, **130,** 1573–1592.

Braun, S.A., M.T. Montgomery, and Z. Pu, 2006: High-resolution simulation of Hurricane Bonnie (1998). Part I: The organization of eyewall vertical motion. *J. Atmos. Sci.*, **63,** 19–42.

Braun, S.A., and L. Wu, 2007: A numerical study of Hurricane Erin (2001). Part II: Shear and the organization of eyewall vertical motion. *Mon. Wea. Rev.*, **135**, 1179–1194.

Bringi, V.N., and V. Chandrasekar. 2001. *Polarimetric Doppler Weather Radar: Principles and Applications.* Cambridge University Press, 636 pp.

Bringi, V.N., T.D. Keenan, and V. Chandrasekar, 2001: Correcting C-band radar reflectivity and differential reflectivity data for rain attenuation: A self-consistent method with constraints. *IEEE Trans. Geosci. Remote Sens.*, **39,** 1906–1915.

Brown, D.P., J.L. Beven, J.L. Franklin, and E.S. Blake, 2010: Atlantic hurricane season of 2008. *Mon. Wea. Rev.*, **138**, 1975–2001.

Cecil, D.J., K.R. Quinlan, and D.M. Marchm 2010: Intense convection observed by NASA ER-2 in Hurricane Emily (2005). *Mon. Wea. Rev.*, **138**, 765-780.

Chandrasekar, V., S. Lim, and E. Gorgucci, 2006: Simulation of X-band rainfall observations from S-sand radar data. *J. Atmos. Oceanic Technol.*, **23**, 1195–1205.

Chong, M., and J. Testud, 1983: Three-dimensional wind field analysis from dual-doppler radar data. Part III: The boundary condition: An optimum determination based on a variational concept. *J. Climate Appl. Meteor.*, **22**, 1227–1241.

Chong, M., J. Testud, and F. Roux, 1983: Three-dimensional wind field analysis from dual-Doppler radar data. Part II: Minimizing the error due to temporal variation. *J. Climate Appl. Meteor.*, **22**, 1216–1226.

Clark, T.L., F.I. Harris, and C.G. Mohr, 1980: Errors in wind fields derived from multiple-Doppler radars: Random errors and temporal errors associated with advection and evolution. *J. Appl. Meteor.*, **19**, 1273–1284.

Corbosiero, K.L., J. Molinari, and M.L. Black, 2005: The structure and evolution of Hurricane Elena (1985). Part I: Symmetric intensification. *Mon. Wea. Rev.*, **133**, 2905–2921

Corbosiero, K.L., J. Molinari, A.R. Aiyyer, and M.L. Black, 2006: The structure and evolution of Hurricane Elena (1985). Part II: Convective asymmetries and evidence for vortex Rossby waves. *Mon. Wea. Rev.*, **134,** 3073–3091.

Cram, T.A., J. Persing, M.T. Montgomery, and S.A. Braun, 2007: A Lagrangian trajectory view on transport and mixing processes between the eye, eyewall, and environment using a high-resolution simulation of Hurricane Bonnie (1998). *J. Atmos. Sci.*, **64,** 1835–1856.

Davies-Jones, R.P., 1978: Dual-Doppler radar coverage area as a function of measurement accuracy and spatial resolution. *J. Appl. Meteor.*, **18**, 1229-1233.

Doviak, R.J., P.S. Ray, R.G. Strauch, and L.J. Miller, 1976: Error estimation in wind fields derived from dual-Doppler radar measurement. *J. Appl. Meteor.*, **15**, 868–878.

Doviak, R.J., and D.S. Zrnic, 1993: *Doppler Radar and Weather Observations.* Academic Press, 562 pp.

Eastin, M.D., P.G. Black, and W.M. Gray, 2005: Buoyancy of convective vertical motions in the inner core of intense hurricanes. Part II: Case studies. *Mon. Wea. Rev.*, **133,** 209–227.

Emanuel, K.A., 1988: The maximum intensity of hurricanes. *J. Atmos. Sci.*, **45,** 1143–1155.

Emanuel, K.A., 1995: Sensitivity of tropical cyclones to surface exchange coefficients and a revised steady-state model incorporating eye dynamics. *J. Atmos. Sci.*, **52,** 3969–3976.

Emanuel, K.A., 1997: Some aspects of hurricane inner-core dynamics and energetics. *J. Atmos. Sci.*, **54,** 1014–1026.

Frank, W.M., and E.A. Ritchie, 1999: Effects of environmental flow upon tropical cyclone structure. *Mon. Wea. Rev.*, **127**, 2044–2061.

Gal-Chen, T., 1978: A method for the initialization of the anelastic equation: Implications for matching models with observations. *Mon. Wea. Rev.*, **106,** 587–606.

Hane, C.E., R.B. Wilhelmson, and T. Gal-Chen, 1981: Retrieval of thermodynamic variables within deep convective clouds: Experiments in three dimensions. *Mon. Wea. Rev.*, **109,** 564–576.

Hendricks, E.A., W.H. Schubert, R.K. Taft, H. Wang, and J.P. Kossin, 2009: Life cycles of hurricane-like vorticity rings. *J. Atmos. Sci.*, **66**, 705–722.

Heymsfield, G.M., L. Tian, A.J. Heymsfield, L. Li, and S. Guimond, 2010: Characteristics of deep tropical and subtropical convection from high-altitude airborne Doppler radar. *J. Atmos. Sci.*, **67**, 285-308.

Holton, J.R., 2004: *An Introduction to Dynamic Meteorology*. 4th ed. Elsevier Academic Press, 529 pp.

Jorgensen, D.P., 1984: Mesoscale and convective-scale characteristics of mature hurricanes. Part II. Inner core structure of Hurricane Allen (1980). *J. Atmos. Sci.*, **41,** 1287–1311.

Jorgensen, D.P., E.J. Zipser, and M.A. LeMone, 1985: Vertical motions in intense hurricanes. *J. Atmos. Sci.*, **42**, 839–856.

Kossin, J.P., and M.D. Eastin, 2001: Two distinct regimes in the kinematic and thermodynamic structure of the hurricane eye and eyewall. *J. Atmos. Sci.*, **58,** 1079–1090.

Kossin, J.P., B.D. McNoldy, and W.H. Schubert, 2002: Vortical swirls in hurricane eye clouds. *Mon. Wea. Rev.*, **130**, 3144–3149.

Kossin, J.P., and W.H. Schubert, 2001: Mesovortices, polygonal flow patterns, and rapid pressure falls in hurricane-like vortices. *J. Atmos. Sci.*, **58**, 2196–2209.

Kossin, J.P., and W.H. Schubert, 2004: Mesovortices in Hurricane Isabel. *Bull. Amer. Meteor. Soc.*, **85**, 151–153.

Lee, W., C. Walther, and R. Oye, 1994: Doppler Radar Data Exchange format DORADE. *NCAR Tech. Note, NCAR/TN-4031IA.*

Lee, W-C., B.J-D. Jou, P-L. Chang, and S-M. Deng, 1999: Tropical cyclone kinematic structure retrieved from single-Doppler radar observations. Part I: Interpretation of Doppler velocity patterns and the GBVTD technique. *Mon. Wea. Rev.*, **127**, 2419-2439.

Lee, W-C., and F.D. Marks, 2000: Tropical cyclone kinematic structure retrieved from single-Doppler radar observations. Part II: The GBVTD-simplex center finding algorithm. *Mon. Wea. Rev.*, **128**, 1925-1936.

Lewis, B., and H. Hawkins, 1982: Polygonal eye walls and rainbands in hurricanes. *Bull. Amer. Meteor. Soc*., 63, 1294–1301.

Liou, Y-C., T-C.C. Wand, W-C. Lee, and Y-J. Chang, 2006: The retrieval of asymmetric tropical cyclone structures using Doppler radar simulations and observations with the extended GBVTD technique. *Mon. Wea. Rev.*, **134**, 1140-1160.

Liu, Y, V.N. Bringi, and M. Maki, 2006: Improved rain attenuation correction algorithms for radar reflectivity and differential reflectivity with adaptation to drop shape model variation. *Proc. 26th Int. Geoscience and Remote Sensing Symposium (IGRASS 2006),* Denver, CO. *IEEE*. 1910-1913.

Marks, F.D., P.G. Black, M.T. Montgomery, and R.W. Burpee, 2008: Structure of the eye and eyewall of Hurricane Hugo (1989). *Mon. Wea. Rev.*, **136**, 1237–1259.

Marks, F.D., and R.A. Houze, 1984: Airborne Doppler radar observations in Hurricane Debby. *Bull. Amer. Meteor. Soc.*, **65**, 569–582.

Matejka, T., and D.L. Bartels, 1998: The accuracy of vertical air velocities from Doppler radar data. *Mon. Wea. Rev.*, **126**, 92–117.

Miller, L.J., and R.G. Stauch, 1974: A dual Doppler radar method for the determination of wind velocities within precipitating weather systems. *Rem. Sens. of Envior.,* **3**, 219-235.

Mohr, C.G., L.J. Miller, R.L. Vaughn, and H.W. Frank, 1986: The merger of mesoscale datasets into a common Cartesian format for efficient and systematic analyses. *J. Atmos. and Ocean. Tech.,* **3**, 143-161.

Montgomery, M.T., M.M. Bell, S.D. Aberson, and M. Black, 2006: Hurricane Isabel (2003): New insights into the physics of intense storms. Part I: Mean vortex structure and maximum intensity estimates. *Bull. Amer. Meteor. Soc.*, **87,** 1335–1347.

Montgomery, M.T., V.A. Vladimirov, and P.V. Denissenko, 2002: An experimental study on hurricane mesovortices. *J. Fluid Mech.*, **471,** 1–32.

Mueller, C.K., and P. Hildebrand, 1985: Evaluation of meteorological airborne Doppler radar. Part II. Triple-Doppler analyses of air motions. *J. Atmos. Oceanic Technol.*, **3,** 381–392.

Murphy, T.A., and K.R. Knupp, 2009: Variability in the kinematic structure of super Tuesday storms. *Preprints, 34th Conf. on Radar Meteorology*, Williamsburg, VA, Amer. Meteor. Soc.

National Oceanic and Atmospheric Administration, cited 2009: Distance Learning Operations Course Topic 3 Lesson 1. [Available online at http://www.wdtb.noaa.gov/courses/dloc/topic3/lesson1/index.html]

O'Brien, J.J., 1970: Alternative solutions to the classical vertical velocity problem. *J. Appl. Meteor.*, **9,** 197–203.

Oye, R., C. Mueller, and S. Smith, 1995: Software for radar translation, visualization, editing, and interpolation. *Preprints, 27th Conf. on Radar Meteorology*, Vail, CO, Amer. Meteor. Soc.

Pershing, J., and M.T. Montgomery, 2003: Hurricane superintensity. *J. Atmos. Sci.*, **60,** 2349–2371.

Ray, P.S., M. Gilet, and K.W. Johnson, 1980: The multiple Doppler radar workshop, November 1979. Part IV: Motion field synthesis and radar placement. *Bull. Amer. Meteor. Soc.*, **61,** 1184–1189.

Ray, P., K.K. Wagner, K.W. Johnson, J.J. Stephens, W.C. Bumgarner, and E.A. Muller, 1978: Triple-Doppler observations of a convective storm. *J. Appl. Meteor.*, **17,** 1201–1212.

Reasor, P.D., M.D. Eastin, and J.F. Gamache, 2009: Rapidly intensifying Hurricane Guillermo (1997). Part I: Low-wavenumber structure and evolution. *Mon. Wea. Rev.*, **137**, 603–631.

Reasor, P.D., M.T. Montgomery, F.D. Marks, and J.F. Gamache, 2000: Low-wavenumber structure and evolution of the hurricane inner core observed by airborne dual-Doppler radar. *Mon. Wea. Rev.*, **128,** 1653–1680.

Rew, R.K., and G.P. Davis, 1990: NetCDF: An interface for scientific data access. *Comp. Graphics and App., IEEE,* 76-82.

Rinehart, R.E., 2004: *Radar for Meteorologists*. 4th ed. Rinehart, 482 pp.

Roux, F., 1985: Retrieval of thermodynamic fields from multiple-Doppler radar data using the equations of motion and the thermodynamic equation. *Mon. Wea. Rev.*, **113,** 2142–2157.

Roux, F., J. Testud, M. Payen, and B. Pinty, 1984: West African squall-line structure retrieved from dual-Doppler radar observations. *J. Atmos. Sci.*, **41,** 3104–3121.

Rozoff, C.M., J.P. Kossin, W.H. Schubert, and P.J. Mulero, 2009: Internal control of hurricane intensity variability: The dual nature of potential vorticity mixing. *J. Atmos. Sci.*, **66**, 133–147.

Saffir, H.S., 1973: Hurricane wind and storm surge. *Mil. Eng.*, **423,** 4–5.

Schubert, W.H., M.T. Montgomery, R.K. Taft, T.A. Guinn, S.R. Fulton, J.P. Kossin, and J.P. Edwards, 1999: Polygonal eyewalls, asymmetric eye contraction, and potential vorticity mixing in hurricanes. *J. Atmos. Sci.*, **56**, 1197–1223.

Shapiro, A., K.M. Willingham, and C.K. Potvin, 2010a: Spatially variable advection correction of radar data. Part I: Theoretical considerations. *J. Atmos. Sci.*, **67,** 3445–3456.

Shapiro, A., K.M. Willingham, and C.K. Potvin, 2010b: Spatially variable advection correction of radar data. Part II: Test results. *J. Atmos. Sci.*, **67,** 3457–3470.

Simpson, R.H., 1974: The hurricane disaster potential scale. *Weatherwise*, **27.**169, 186.

Sitkowski, M., and G.M. Barnes, 2009: Low-level thermodynamic, kinematic, and reflectivity fields of Hurricane Guillermo (1997) during rapid intensification. *Mon. Wea. Rev.*, **137**, 645–663.

Snyder, J.C., H.B. Bluestein, G. Zhang, and S.J. Frasier, 2010: Attenuation correction and hydrometeor classification of high-resolution, X-band, dual-polarized mobile radar measurements in severe convective storms. *J. Atmos. Oceanic Technol.*, **27**, 1979–2001.

Testud, J., and M. Chong, 1983: Three-dimensional wind field analysis from dual-Doppler radar data. Part I: Filtering, interpolating and differentiating the raw data. *J. Climate Appl. Meteor.*, **22**, 1204–1215.

University of Wisconsin, Cooperative Institute for Meteorological Satellite Studies (CIMSS) cited 2011: North Atlantic deep layer shear - zoom GOES-East satellite derived product for 18 UTC 12 September - 06 UTC 13 September 2008 [Available online at http://tropic.ssec.wisc.edu/archive]

Wang, Y., and C.C. Wu, 2004: Current understanding of tropical cyclone structure and intensity changes – A review. *Meteor. Atmos. Phys.,* **87**, 257-278.

Willoughby, H.E., 1998: Tropical cyclone eye thermodynamics. *Mon. Wea. Rev.,***126,** 3053–3067.

Willoughby, H., and P. Black, 1996: Hurricane Andrew in Florida: Dynamics of a disaster. *Bull. Amer. Meteor. Soc.*, **77**, 543–549.

Willoughby, H.E., and M.B. Chelmow, 1982: Objective determination of hurricane tracks from aircraft observations. *Mon. Wea. Rev.*, **110**, 1298–1305.